

# Antennas for 5G and Future Communication Systems

Lead Guest Editor: Muhammad Inam Abbasi

Guest Editors: Muhammad Ramlee Kamarudin, Qammer H. Abbasi,  
Hashim Dahri, and Mohd Haizal Jamaluddin





---

# **Antennas for 5G and Future Communication Systems**

International Journal of Antennas and Propagation

---

## **Antennas for 5G and Future Communication Systems**

Lead Guest Editor: Muhammad Inam Abbasi

Guest Editors: Muhammad Ramlee Kamarudin,  
Qammer H. Abbasi, Hashim Dahri, and Mohd  
Haizal Jamaluddin



---

Copyright © 2022 Hindawi Limited. All rights reserved.

This is a special issue published in “International Journal of Antennas and Propagation.” All articles are open access articles distributed under the Creative Commons Attribution License, which permits unrestricted use, distribution, and reproduction in any medium, provided the original work is properly cited.

# Chief Editor

Slawomir Koziel , Iceland

## Associate Editors

Sotirios K. Goudos , Greece  
N. Nasimuddin , Singapore  
Ikmo Park , Republic of Korea

## Academic Editors

Kush Agarwal , Singapore  
Ana Alejos , Spain  
Mohammad Ali, USA  
Rodolfo Araneo, Italy  
Hervé Aubert , France  
Paolo Baccarelli , Italy  
Xiulong Bao, Ireland  
Giulio Maria Bianco , Italy  
Pietro Bolli , Italy  
Paolo Burghignoli , Italy  
Shah Nawaz Burokur , France  
Giuseppe Castaldi , Italy  
Giovanni Andrea Casula , Italy  
Luca Catarinucci, Italy  
Felipe Cátedra , Spain  
Marta Cavagnaro , Italy  
Ayan Chatterjee , India  
Maggie Y. Chen , USA  
Shih Yuan Chen , Taiwan  
Renato Cicchetti , Italy  
Riccardo Colella , Italy  
Laura Corchia , Italy  
Claudio Curcio, Italy  
Francesco D'Agostino , Italy  
Michele D'Urso, Italy  
María Elena De Cos Gómez , Spain  
Arpan Desai, Taiwan  
Alessandro Di Carlofelice , Italy  
Giuseppe Di Massa , Italy  
Flaminio Ferrara , Italy  
Ravi Kumar Gangwar, India  
Claudio Gennarelli , Italy  
Farid Ghanem, Algeria  
Rocco Guerriero , Italy  
Kerim Guney, Turkey  
Ashish Gupta , India  
Tamer S. Ibrahim , USA

Muhammad Ramlee Kamarudin , Malaysia  
Dmitry V. Kholodnyak , Russia  
Rajkishor Kumar , India  
Ping Li , China  
Ding-Bing Lin , Taiwan  
Angelo Liseno, Italy  
Gui Liu , China  
Pierfrancesco Lombardo , Italy  
Lorenzo Luini , Italy  
Giovanni Magno, Italy  
Praveen Kumar Malik, India  
Bappaditya Mandal, Sweden  
Atsushi Mase, Japan  
Diego Masotti , Italy  
Christoph F. Mecklenbräuker , Austria  
Ananda S. Mohan, Australia  
Jose-Maria Molina-Garcia-Pardo , Spain  
Giuseppina Monti , Italy  
Giorgio Montisci , Italy  
Andrea Francesco Morabito , Italy  
Mohammad H. Neshati , Iran  
Truong Khang Nguyen, Vietnam  
Symeon Nikolaou , Cyprus  
Amrindra Pal , India  
Sandeep Kumar Palaniswamy, India  
Mauro Parise , Italy  
Josep Parrón, Spain  
Shobhitkumar Patel , India  
Anna Pietrenko-Dabrowska, Poland  
Khaled ROUABAH, Algeria  
MADAN KUMAR SHARMA, Oman  
VISHAL SORATHIYA, India  
Ahmad Safaai-Jazi, USA  
Safieddin Safavi-Naeini, Canada  
Stefano Selleri , Italy  
Zijian Shao, USA  
Raffaele Solimene , Italy  
Gina Sorbello , Italy  
Seong-Youp Suh, USA  
Larbi Talbi, Canada  
Luciano Tarricone, Italy  
Sreenath Reddy Thummalur, India  
Giuseppe Torrisi , Italy  
Trushit Upadhyaya , India



---

Chien-Jen Wang , Taiwan  
Mustapha C E Yagoub , Canada  
Yuan Yao , China  
Tao Zhou , China  
Muhammad Zubair , Pakistan

## Contents

### **A Wideband Hybrid Fractal Ring Antenna for WLAN Applications**

Atif Jamil , Muhammad Rauf , Abdul Sami , Arsalan Ansari , and Muhammad Dawood Idrees   
Research Article (8 pages), Article ID 6136916, Volume 2022 (2022)

### **Corrigendum to “Square-Framed T Shape mmwave Antenna Array at 28 GHz for Future 5G Devices”**

Saad Hassan Kiani, Xin Cheng Ren, Adil Bashir, Muhammad Rizwan Anjum, Ammar Rafiq, Mian Muhammad Kamal, Burhan Ud Din, and Fazal Muhammad  
Corrigendum (1 page), Article ID 9839346, Volume 2022 (2022)

### **Novel Compact Design and Investigation of a Super Wideband Millimeter Wave Antenna for Body-Centric Communications**

H. M. Arifur Rahman , Mohammad Monirujjaman Khan , Mohammed Baz , Mehedi Masud ,  
and Mohammed A. AlZain   
Research Article (15 pages), Article ID 8725263, Volume 2021 (2021)

### **A Wideband Reflector-Backed Antenna for Applications in GPR**

A. Raza , W. Lin , M. K. Ishfaq , M. Inam , F. Masud , and M. H. Dahri   
Research Article (10 pages), Article ID 3531019, Volume 2021 (2021)

### **A Novel Shape Compact Antenna for Ultrawideband Applications**

Saad Hassan Kiani , Xin Cheng Ren , Muhammad Rizwan Anjum , Khalid Mahmood , Haider Ali , Naveed Jan , Muhammad Adil Bashir , and Muhammad Abbas Khan   
Research Article (7 pages), Article ID 7004799, Volume 2021 (2021)

### **Square-Framed T Shape mmwave Antenna Array at 28 GHz for Future 5G Devices**

Saad Hassan Kiani , Xin Cheng Ren , Adil Bashir , Ammar Rafiq , Muhammad Rizwan Anjum , Mian Muhammad Kamal, Burhan Ud Din , and Fazal Muhammad   
Research Article (9 pages), Article ID 2286011, Volume 2021 (2021)

### **Various Textiles-Based Comparative Analysis of a Millimeter Wave Miniaturized Novel Antenna Design for Body-Centric Communications**

Mohammad Monirujjaman Khan , Kaisarul Islam , Md. Nakib Alam Shovon , Mehedi Masud ,  
Mohammed Baz , and Mohammed A. AlZain   
Research Article (14 pages), Article ID 2360440, Volume 2021 (2021)

## Research Article

# A Wideband Hybrid Fractal Ring Antenna for WLAN Applications

Atif Jamil <sup>1</sup>, Muhammad Rauf <sup>1</sup>, Abdul Sami <sup>1</sup>, Arsalan Ansari <sup>1</sup>,  
and Muhammad Dawood Idrees <sup>2</sup>

<sup>1</sup>Department of Electronic Engineering, Dawood University of Engineering & Technology Karachi, M. A Jinnah Road, Karachi-74800, Pakistan

<sup>2</sup>Department of Industrial Engineering and Management, Dawood University of Engineering & Technology Karachi, M. A Jinnah Road, Karachi-74800, Pakistan

Correspondence should be addressed to Atif Jamil; [atif.jamil@duet.edu.pk](mailto:atif.jamil@duet.edu.pk)

Received 17 September 2021; Revised 3 January 2022; Accepted 8 January 2022; Published 21 February 2022

Academic Editor: Muhammad Inam Abbasi

Copyright © 2022 Atif Jamil et al. This is an open access article distributed under the Creative Commons Attribution License, which permits unrestricted use, distribution, and reproduction in any medium, provided the original work is properly cited.

We propose the design of a novel fractal antenna that is both unique and performance-driven. Two important antenna design features, miniaturization and wideband operation, are combined in this work. A ring-shaped antenna is designed using the well-known fractal geometry. This hybrid geometry is a fusion of meander and Koch curve shapes. The geometrical construction of the proposed antenna is compared to the standard Koch curve geometry. It is shown that combining the meander and Koch curve shapes increases the effective electrical length. The wider bandwidth is achieved by bringing the higher modes together. The overall dimensions of proposed meander Koch curve fractal ring antenna are  $45 \times 25 \times 1.6 \text{ mm}^3$ . The resonance frequency of the antenna is between 4.94 and 6.12 GHz (% BW = 21.83), which covers the entire 5 GHz WLAN band. The prototype has been fabricated and experimentally verified.

## 1. Introduction

The advancement of wireless communication technology has raised the bar for modern living. The sophisticated devices have brought a great degree of freedom to the conventional stationary working styles. The demand for data-hungry applications and multimedia streaming videos has given rise to the improved quality of service (QoS) in wireless communication systems. Antenna, an essential part of wireless communication system, must respond to the call of QoS improvement by enhancing its performance by aiming wide bandwidth, high gain, reduced return loss, omnidirectional radiation pattern, low cross-polarization, and reduced cost for fabrication. Fractal geometry has a long history; since its inception, fractals have been practically deployed in various technical fields. Mandelbrot introduced the term fractal from the Latin word “Fractus” in 1975 [1, 2]. Fractal shapes are nowhere differentiable as they are resultant of a recursive process. The increased bandwidth has been linked to fractal geometry’s self-similar, convoluted

and jagged structures. Additionally, fractal geometry is used in antennas because of its unique properties, including small size and multiband/wideband behavior [3]. Numerous researchers have advocated incorporating fractal geometry into their antenna research. Several antenna geometries have been examined, including Koch, Cantor, Sierpinski, fractal tree, and Minkowski. In [4], an octagonal Fractal microstrip patch antenna with a superwideband bandwidth range of 10 GHz–50 GHz has been presented. For numerous applications such as PCS, WLAN, WiFi, WiMax, and other communication systems, a Koch-like fractal curve has been proposed [5]. A Pythagorean tree was placed in a T-patch to form an ultrawideband (UWB) antenna [6]. Grounded coplanar waveguides have been used to enhance the bandwidth of conventional Sierpinski carpet antenna [7]. Additionally, various fractal shapes have been used to improve the properties of the dielectric resonator antennas [8–13].

Numerous fractal geometries have been combined to enhance the properties of fractal antennas such as

multiband/wideband operation and size reduction. Using Koch curves as inductive loading and Sierpinski carpet as a slot loading, the resonant frequency and the size of a patch antenna can be reduced, as shown by experiments in [14]. Fractal shapes have been modified to alter the characteristics of the antenna which are driven by the shape of antenna. A perturbed Sierpinski fractal antenna with slotted ground plane has been proposed for GSM/DCS/PCS/IMT-2000/ISM/satellite DMB bands [15]. For a WLAN USB dongle, the hybrid meander-Koch monopole antenna was presented in [16]. The antenna is multiband-capable, operating throughout the whole IEEE 802.11 a/b/g spectrum. In [17], a UWB antenna based on Giuseppe Peano and Sierpinski carpet fractal geometries was proposed. Two different fractal antennas have been fused together to design a multiband antenna for Wi-Max and C-band applications [18]. A multiband hybrid fractal antenna based on Koch–Minkowski geometry has been developed for use in a variety of wireless applications [19]. A report on the construction of a hybrid fractal antenna comprising Giuseppe Peano, Cantor set, and Sierpinski carpet for industrial, scientific, and medical (ISM) band has been presented in [20]. A hybrid fractal antenna based on Moore, Minkowski, and Koch curve for multiband applications such as Wi-Fi, Bluetooth, and Wi-MAX has been reported in [21]. A hybrid fractal antenna with a defected ground structure (DGS) was optimized for S, C, and X applications using artificial neural networks (ANNs) [22]. An ultrawideband hybrid fractal antenna based on Koch and Sierpinski Fractals has been reported in [23]. Using the well-known Minkowski and Hilbert curves, a hybrid fractal antenna has been designed [24].

In this paper a hybrid Fractal antenna geometry has been proposed for 5 GHz WLAN band. The antenna has been constructed by merging the meander and Koch curve geometries. The antenna has been experimentally studied to optimize its performance impedance bandwidth. The proposed antenna has been designed to operate in the IEEE 802.11a (WLAN) i.e., 5.15–5.825 band. The antenna prototype has been physically analysed and the actual measurement results have been found to be in good agreement with the simulation results. The simulation and measurement results indicate that the proposed antenna can achieve an impedance bandwidth of more than 1 GHz at  $-10$  dB scale. The configuration of the proposed antenna has been described in Section 2. Section 3 presents a study on the parametric optimization of the proposed meander-Koch Fractal ring antenna. Experimental results have been presented in Section 4. The conclusion follows in Section 5.

## 2. Antenna Design

Figure 1 illustrates the suggested antenna design. The hybrid meander-Koch Fractal ring antenna measures  $45 \times 25 \text{ mm}^2$  in total and is printed on top of FR-4 dielectric substrate. The dielectric substrate has a height of  $h = 1.6 \text{ mm}$  and a relative dielectric constant of  $\epsilon_r = 4.34$ . The antenna is fed with a

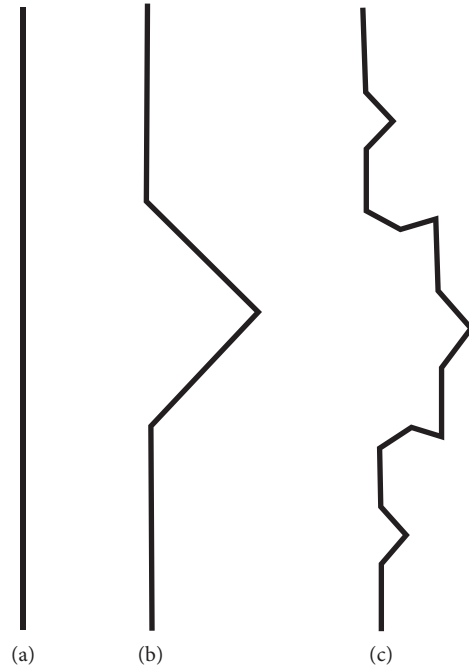


FIGURE 1: Generation of a standard Koch curve geometry. (a) First iteration, (b) second iteration, (c) third iteration.

microstrip transmission line terminated with a  $50 \Omega$  feeder. The proposed antenna has a ground plane on the opposite side of the radiating hybrid meander-Koch Fractal ring element.

The construction of the hybrid meander-Koch Fractal ring antenna is defined by using the iteration function system (IFS) algorithm [25–30]. To justify the complex design and construction of a new Fractal shape, the proposed hybrid meander-Koch Fractal antenna’s generator is compared to that of a standard Koch curve Fractal antenna. The shapes are compared according to their ability to increase the effective electrical length.

*2.1. Construction of Standard Koch Curve Using IFS.* Helge von Koch, a Swedish mathematician, invented the standard Koch curve geometry in 1904 [28]. The standard Koch is constructed using the initiator-generator method. As illustrated in Figures 1(a)–1(c), this method applies several transformations to a straight line in order to convert it to a Koch shape. A straight line (initiator) is divided into three equal sections, with the middle section further subdivided into two equal sections. The resultant shape is called the generator, and this procedure can be repeated to achieve the higher iterations.

The IFS algorithm is used to construct the standard Koch curve shown in Figures 1(a)–1(c). The IFS is formed by the set of affine transformations to generate the standard Koch. In its construction, it is assumed that a straight line of unit length is placed along the  $x$ -axis with its left end placed at the origin. The transformations used to construct the Koch curve antenna’s generator are as follows:

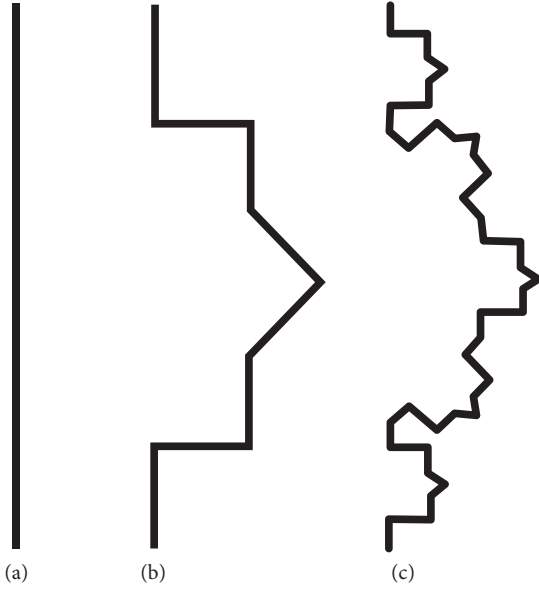


FIGURE 2: Transformations of the hybrid meander-Koch curve Fractal antenna. (a) 0<sup>th</sup> transformation. (b) 1<sup>st</sup> transformation. (c) 2<sup>nd</sup> transformation.

$$\begin{aligned}
 W_1 \begin{pmatrix} x' \\ y' \end{pmatrix} &= \begin{bmatrix} \frac{1}{3} & 0 \\ 0 & \frac{1}{3} \end{bmatrix} \begin{pmatrix} x \\ y \end{pmatrix}, \\
 W_2 \begin{pmatrix} x' \\ y' \end{pmatrix} &= \begin{bmatrix} \frac{1}{3} \cos 60^\circ & -\frac{1}{3} \cos 60^\circ \\ \frac{1}{3} \sin 60^\circ & \frac{1}{3} \cos 60^\circ \end{bmatrix} \begin{pmatrix} x \\ y \end{pmatrix} + \begin{pmatrix} \frac{1}{3} \\ 0 \end{pmatrix}, \\
 W_3 \begin{pmatrix} x' \\ y' \end{pmatrix} &= \begin{bmatrix} \frac{1}{3} \cos 60^\circ & -\frac{1}{3} \sin 60^\circ \\ -\frac{1}{3} \sin 60^\circ & \frac{1}{3} \cos 60^\circ \end{bmatrix} \begin{pmatrix} x \\ y \end{pmatrix} + \begin{pmatrix} \frac{1}{2} \\ \frac{1}{2} \sin 60^\circ \end{pmatrix}, \\
 W_4 \begin{pmatrix} x' \\ y' \end{pmatrix} &= \begin{bmatrix} \frac{1}{3} & 0 \\ 0 & \frac{1}{3} \end{bmatrix} \begin{pmatrix} x \\ y \end{pmatrix} + \begin{pmatrix} \frac{2}{3} \\ 0 \end{pmatrix}.
 \end{aligned} \tag{1}$$

The generator is obtained by combining the segments as

$$A_1 = W(A) = W_1(A) \cup W_2(A) \cup W_3(A) \cup W_4(A). \tag{2}$$

The procedure described previously can be used to generate iterations of higher order. To generate self-similar geometry, the distance between the start and end points of all iterations must be the same. The dimensions of self-similarity are calculated as

$$D = \frac{\log 4}{\log 3} = 1.2618. \tag{3}$$

This implies that four identical copies are scaled by a factor of three during each iteration.

**2.2. Construction of Hybrid Meander-Koch Curve Using IFS.** Hybrid fractal geometries are created by fusing two fractal geometries together or by fusing a fractal shape with a nonfractal shape. Additionally, certain hybrid fractal shapes can be created by combining multiple shapes. As illustrated in Figures 2(a)–2(c), the hybrid meander-Koch curve generator is created by combining the meander and Koch curve shapes. The meander and Koch curve generators (first iteration) each contain four and five segments, respectively. However, as illustrated in Figure 2(b), when the two shapes are combined, the resulting generator contain eight segments. This method clearly contributes to antenna's size reduction by increasing the effective electric length. The IFS algorithm for constructing the segments of the meander-Koch curve fractal antenna is as follows:

$$\begin{aligned}
 W_1 \begin{bmatrix} x' \\ y' \end{bmatrix} &= \begin{bmatrix} \frac{1}{5} & 0 \\ 0 & \frac{1}{5} \end{bmatrix} \begin{bmatrix} x \\ y \end{bmatrix}, \\
 W_2 \begin{bmatrix} x' \\ y' \end{bmatrix} &= \begin{bmatrix} 0 & -\frac{1}{5} \\ \frac{1}{5} & 0 \end{bmatrix} \begin{bmatrix} x \\ y \end{bmatrix} + \begin{bmatrix} \frac{1}{5} \\ 0 \end{bmatrix}, \\
 W_3 \begin{bmatrix} x' \\ y' \end{bmatrix} &= \begin{bmatrix} \frac{1}{5} & 0 \\ 0 & \frac{1}{5} \end{bmatrix} \begin{bmatrix} x \\ y \end{bmatrix} + \begin{bmatrix} \frac{1}{5} \\ \frac{1}{5} \end{bmatrix}, \\
 W_4 \begin{bmatrix} x' \\ y' \end{bmatrix} &= \begin{bmatrix} \frac{1}{5} \cos 45^\circ & -\frac{1}{5} \sin 45^\circ \\ \frac{1}{5} \sin 45^\circ & \frac{1}{5} \cos 45^\circ \end{bmatrix} \begin{bmatrix} x \\ y \end{bmatrix} + \begin{bmatrix} \frac{2}{5} \\ \frac{1}{5} \end{bmatrix}, \\
 W_5 \begin{bmatrix} x' \\ y' \end{bmatrix} &= \begin{bmatrix} \frac{1}{5} \cos 45^\circ & \frac{1}{5} \sin 45^\circ \\ -\frac{1}{5} \sin 45^\circ & \frac{1}{5} \cos 45^\circ \end{bmatrix} \begin{bmatrix} x \\ y \end{bmatrix} + \begin{bmatrix} \frac{2.5}{5} \\ \frac{1}{5} \sin 45^\circ \end{bmatrix}, \\
 W_6 \begin{bmatrix} x' \\ y' \end{bmatrix} &= \begin{bmatrix} \frac{1}{5} & 0 \\ 0 & \frac{1}{5} \end{bmatrix} \begin{bmatrix} x \\ y \end{bmatrix} + \begin{bmatrix} \frac{3}{5} \\ \frac{1}{5} \end{bmatrix}, \\
 W_8 \begin{bmatrix} x' \\ y' \end{bmatrix} &= \begin{bmatrix} \frac{1}{5} & 0 \\ 0 & \frac{1}{5} \end{bmatrix} \begin{bmatrix} x \\ y \end{bmatrix} + \begin{bmatrix} \frac{4}{5} \\ 0 \end{bmatrix},
 \end{aligned} \tag{4}$$

$$\begin{aligned}
 W(A) &= W_1(A) \cup W_2(A) \cup W_3(A) \cup W_4(A) \\
 &\cup W_5(A) \cup W_6(A) \cup W_7(A) \cup W_8(A),
 \end{aligned}$$

where the generator  $W(A)$  is obtained by combining  $W_1$  to  $W_8$  which are the set of linear affine transformations and  $A$  is the initial geometry. The fractal dimension  $D$  for the 1<sup>st</sup> transformation of the meander-Koch curve Fractal antenna is calculated as

$$D = \frac{\log(N)}{\log(r)} = \frac{\log 8}{\log 5} = 1.29, \quad (5)$$

where  $N$  is the total number of segments at each iteration and  $r$  is number by which the initiator is divided at each iteration.

**2.3. Development of Hybrid Meander-Koch Fractal Ring Antenna.** The proposed antenna in this section has a ring type structure, and it has been formed by following the basis of the fractal geometry. The generator is a meander-Koch curve shape, and the initiator is a trapezoid-like shape with three linear strips that are presented for transformation, as shown in Figure 3(a). The transformation has been carried out in two-steps: in the first step, a meander pattern is applied on each leg of the trapezoid resembling shape. In the next step, the Koch fractal pattern is applied at the top of the meander element, and this is achieved by forming an upper portion of the equilateral triangle in the middle of the meander shape. As a result of this two-step transformation, all the three linear segments have been replaced by the meander-Koch elements, and the obtained shape is illustrated in Figure 3(b). In Figure 3(c), a segment of the microstrip line has been used to interconnect the two arms through the open ends to form a closed loop radiating structure. Practical limitations exist in terms of applying the higher order iterations to design the fractal antennas. These include the overlap between the strips of the adjacent segments in the geometry which consequently deforms its shape. To avoid this situation, the line width should be very narrow; however, this could give rise to the conductor losses which reduces the radiation efficiency. Therefore, the iterative transformation on the meander-Koch Fractal ring antenna has been limited up to the second iteration. Moreover, the dimensions of the proposed meander-Koch fractal ring antenna have been presented in Figure 4 and Table 1.

### 3. Parametric Optimization

After the design of the proposed antenna using IFS, it has been analysed in commercial full-wave simulator CST Microwave Studio (MWS) for studying the effects of the variation of the design parameters. Design goals have been set to achieve an impedance bandwidth that can cover the entire 5 GHz band. In order to realize such an antenna with desired performance, a series of parametric studies have been performed on important design parameters. As elaborated in Section 2.3, the geometric construction of the resultant antenna shape started from an initiator that resembles a trapezoid shape which was presented for transformations using the meander-Koch curve shape. Figure 5 shows the optimization study which has been carried on different lengths of the ring-type antenna. The length  $L_{M-kr}$  of the radiating element has been optimized to make the antenna resonant on the entire 5 GHz band.

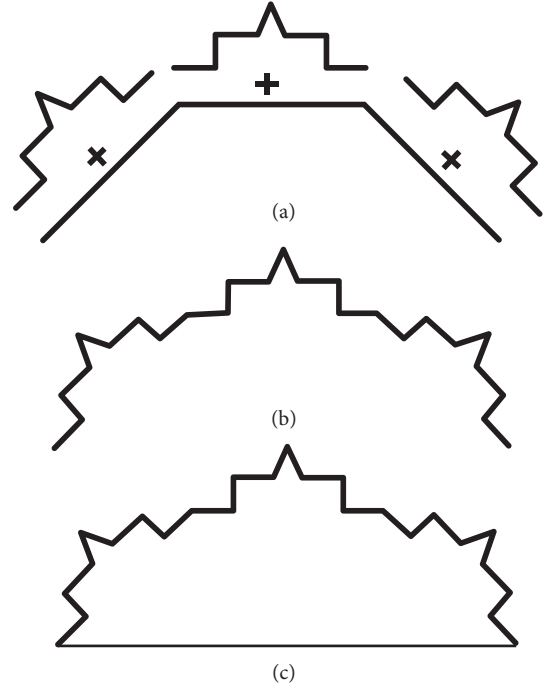


FIGURE 3: Transformations of the meander-Koch fractal ring antenna. (a) Geometries of the initiator and generator; (b) combined shape; (c) closed loop.

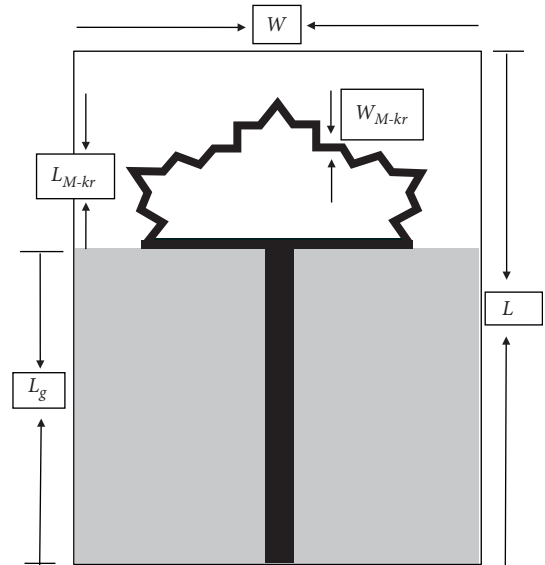


FIGURE 4: Dimensions of the proposed antenna.

A similar study has been conducted to study the effects of the variation of the fractal ring in Figure 6. The thickness  $W_{M-kr}$  of the ring has been varied from 1.1 mm to 1.3 mm with a step size of 0.1 mm. It has been noticed that, as the strip thickness increases, the effective perimeter of the ring geometry also increases which results in frequency reduction.

Figure 7 shows the parametric study on the width of the transmission feed line  $W_f$ . It has been optimized to maintain the reflection coefficient at  $-10$  dB level for the bandwidth

TABLE 1: Dimensions of the proposed meander-Koch fractal ring antenna.

Parameter	Value (mm)
$L$	45
$W = W_g$	25
$L_{M-kr}$	13.1
$W_{M-kr}$	1.1
$L_f = L_g$	26
$W_f$	1.8

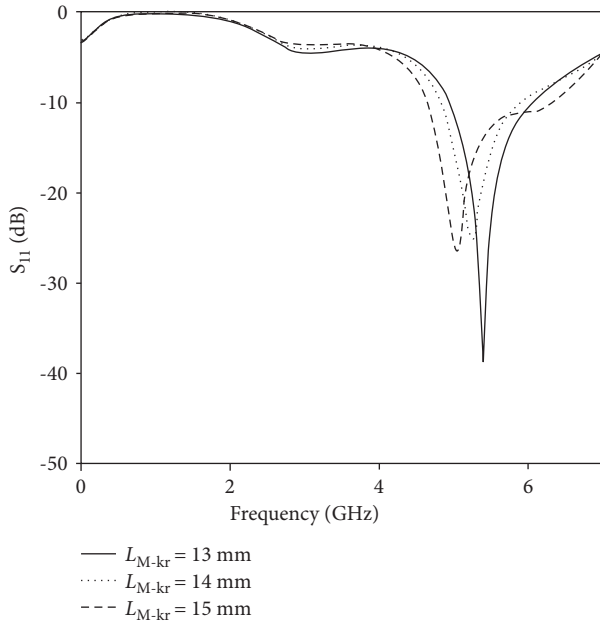


FIGURE 5: The effect of length of the meander-Koch fractal ring antenna on reflection coefficient.

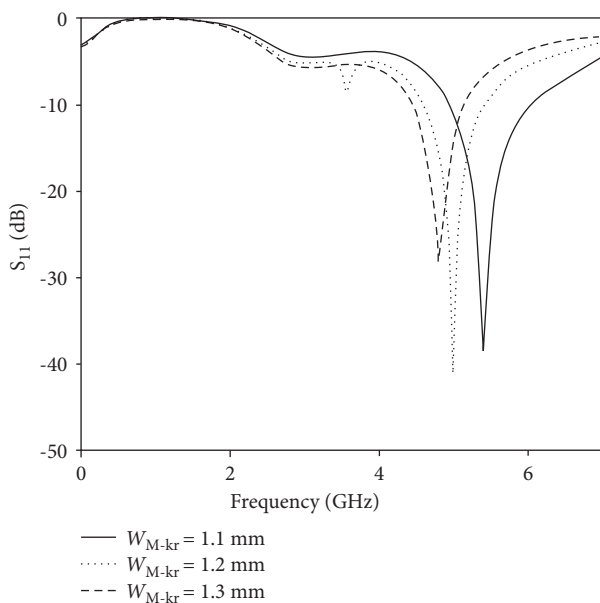


FIGURE 6: The effect of width of the meander-Koch fractal ring antenna on reflection coefficient.

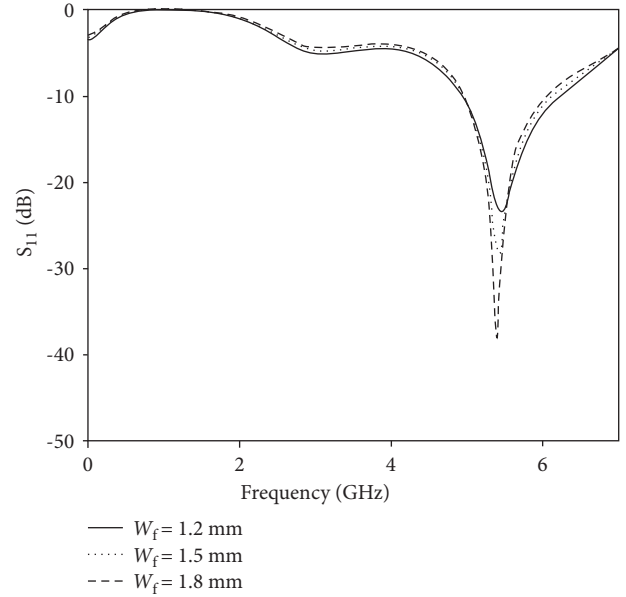


FIGURE 7: The effect of width of the feed line on reflection coefficient.

covering from 4.94 GHz to 6.12 GHz. The width of the transmission line is also a crucial parameter that needs optimization because it is a known reason for impedance mismatch between the antenna and feed line.

The ground plane plays a significant role in the radiation of small antennas. Certain parameters are adversely affected by the small ground plane size. These degradations include a shift in resonant frequencies, impedance mismatch, narrow impedance bandwidth, low gain, low efficiency, and distorted radiation patterns. As illustrated in Figure 8, the final parametric study has been performed by varying the size of the ground plane to avoid the inaccurate measurement results due to cable effects. However, in the optimization process on the size of the ground plane  $G$ , it was noticed that the width of the ground plane  $W_g$  has a considerable effect on the resonant frequency and the input impedance, whereas the length has negligible effect on the said parameters. Therefore, for this study the length ( $L_g = 26$  mm) of the ground plane has been kept constant to perform this study.

#### 4. Experimental Results

In Figure 9, the fabricated prototype of the proposed meander-Koch Fractal ring antenna has been presented. It can be noticed from the comparison curves (simulation and measurement), presented in Figure 10, that antenna has satisfactory return loss result. The antenna is designed to operate on the 5 GHz WLAN band. The measured  $S_{11}$  plot, as shown in Figure 10, of the proposed antenna shows an impedance bandwidth of 1.18 GHz at  $-10$  dB scale.

The simulated and measured far-field radiation patterns of the proposed meander-Koch ring fractal antenna are presented in Figure 11. From the results, the radiation patterns of the meander-Koch fractal ring antenna are

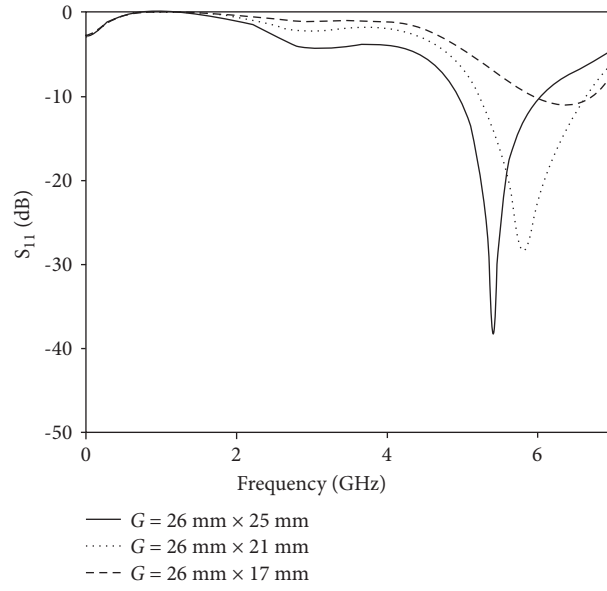


FIGURE 8: The effect of ground plane size on reflection coefficient.

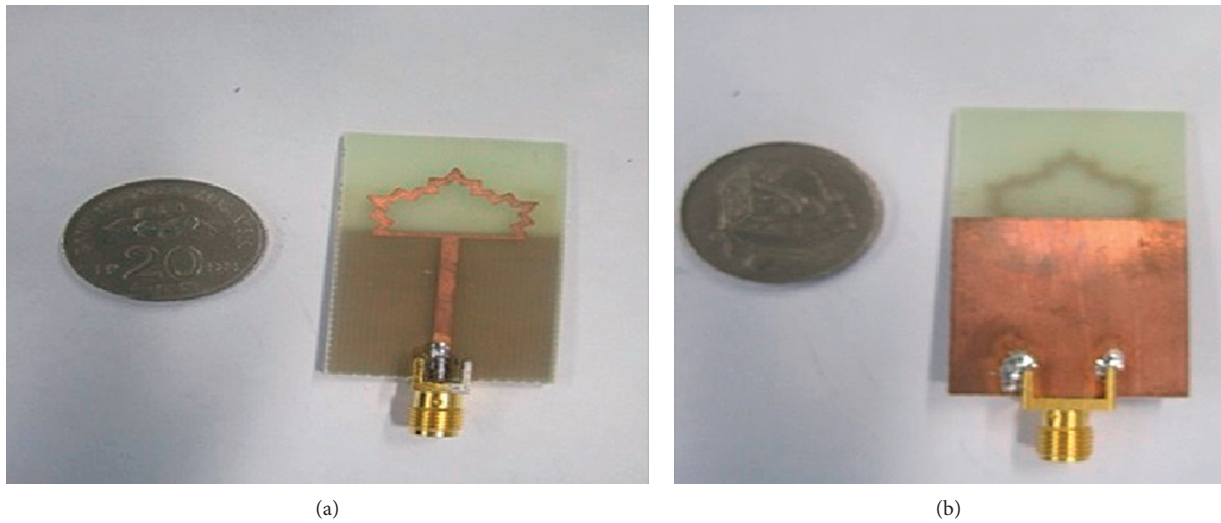


FIGURE 9: Fabricated prototype of proposed meander-Koch fractal ring antenna: (a) top view; (b) back view.

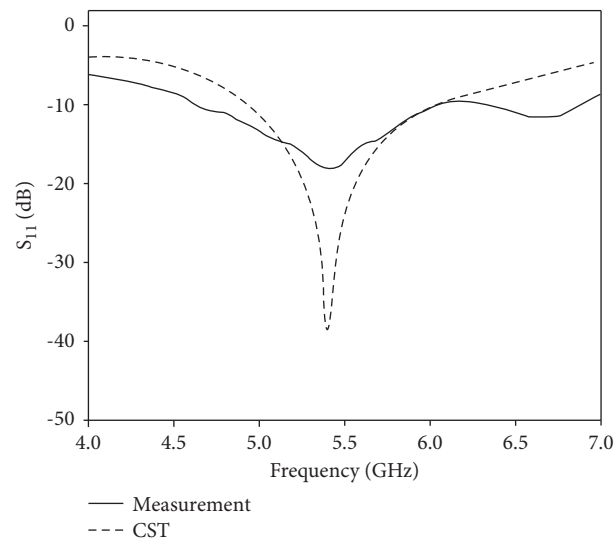


FIGURE 10: Comparison of simulated and measurement results.

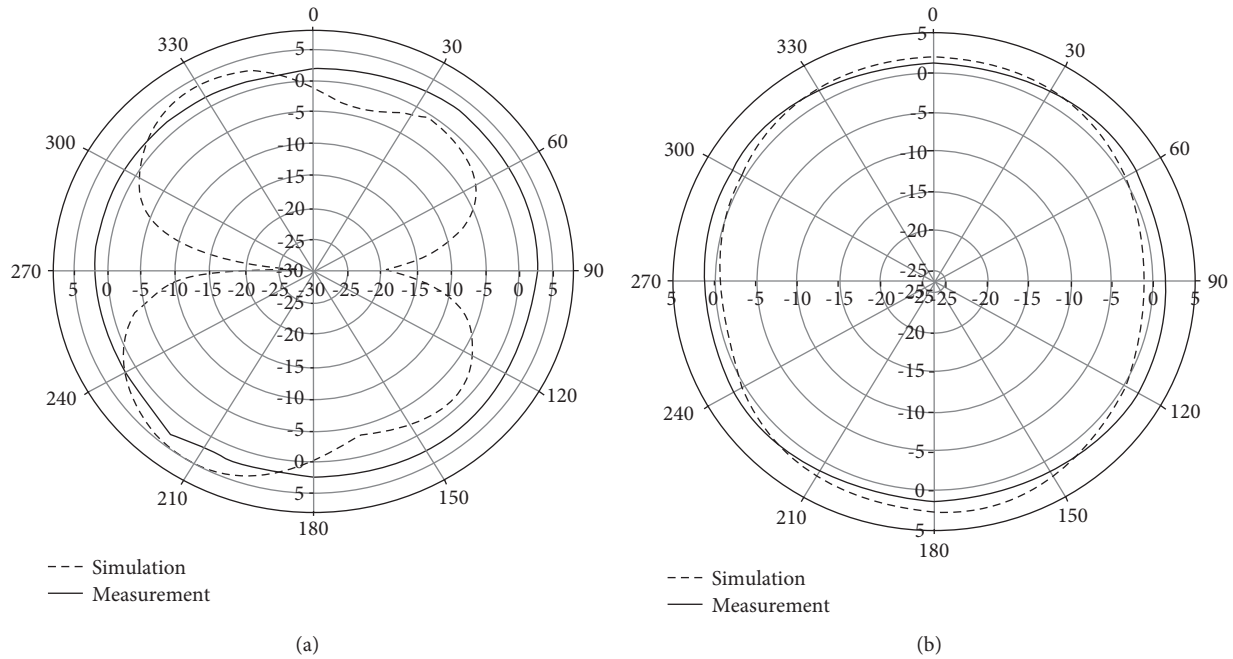


FIGURE 11: Radiation pattern results of the meander-Koch fractal ring antenna. (a) X-Z plane. (b) Y-Z plane.

omnidirectional, and the antenna has a considerable gain from  $0$  to  $2\pi$  radians in both the X-Z and Y-Z planes. Moreover, the measured far-field plot of the proposed antenna in Figure 11(a) illustrates that the proposed meander-Koch fractal ring antenna has symmetric radiation patterns in both the X-Z and Y-Z planes. Figure 11(a) depicts the simulated X-Z plane radiation patterns for the meander-Koch ring fractal antenna, where it has a maximum gain of 3.5 dBi and doughnut-shaped radiation pattern could be easily noticed. In case of measured results, the maximum gain is 3 dBi. Furthermore, Figure 11(b) shows the radiation patterns of the meander-Koch fractal ring antenna in the Y-Z plane. The simulation result shows that the maximum gain is 1.8 dBi, whereas the measurement result shows a maximum gain of 1.43 dBi.

## 5. Conclusion

In this paper, a hybrid meander-Koch fractal ring antenna has been proposed for 5 GHz WLAN band. The IFS algorithm to construct the generator of the proposed antenna has been compared to the standard Koch curve antenna. Due to an increase in the number of segments of the resulting convoluted shape, the electrical length has been increased, thus miniaturizing the antenna size. Several antenna dimensions have been optimized through the parametric study in CST MWS. The antenna prototype has been realized, and the comparison between the simulated and measurement results has been presented, which confirms the practicality of the proposed antenna.

## Data Availability

No data were used to support this study.

## Conflicts of Interest

All authors declare that they have no conflicts of interest.

## Authors' Contributions

All authors contributed equally in this work.

## References

- [1] J. P. Gianvittorio and Y. S. Rahmat, "Fractal antennas: a novel antenna miniaturization technique, and applications," *IEEE Antennas and Propagation Magazine*, vol. 44, no. 1, pp. 20–36, 2002.
- [2] J. Anguera, A. Andújar, J. Jayasinghe et al., "Fractal antennas: an historical perspective," *Fractal and Fractional*, vol. 4, no. 1, p. 3, 2020.
- [3] A. Ramadan, K. Y. Kaban, A. El-Hajj, S. Khoury, and M. Al-Husseini, "A reconfigurable U-Koch microstrip antenna for wireless applications," *Progress In Electromagnetics Research*, vol. 93, pp. 355–367, 2009.
- [4] A. Azari, "A new super wideband fractal microstrip antenna," *IEEE Transactions on Antennas and Propagation*, vol. 59, no. 5, pp. 1724–1727, 2011.
- [5] D. Li and F. Mao, "A Koch-like sided fractal bow-tie dipole antenna," *IEEE Transactions on Antennas and Propagation*, vol. 60, no. 5, pp. 2242–2251, 2012.
- [6] J. Pourahmadazar, C. Ghobadi, and J. Nourinia, "Novel modified pythagorean tree fractal monopole antennas for UWB applications," *IEEE Antennas and Wireless Propagation Letters*, vol. 10, pp. 484–487, 2011.
- [7] M. J. Naghshvarian Jahromi, A. Falahati, and R. M. Edwards, "Bandwidth and impedance-matching enhancement of fractal monopole antennas using compact grounded coplanar waveguide," *IEEE Transactions on Antennas and Propagation*, vol. 59, no. 7, pp. 2480–2487, 2011.

- [8] S. Dhar, R. Ghatak, B. Gupta, and D. R. Poddar, "A wideband minkowski fractal dielectric resonator antenna," *IEEE Transactions on Antennas and Propagation*, vol. 61, no. 6, pp. 2895–2903, 2013.
- [9] D. V. Kiran, D. Sankaranarayanan, and B. Mukherjee, "Compact embedded dual-element rectangular dielectric resonator antenna combining sierpinski and minkowski fractals," *IEEE Transactions on Components, Packaging, and Manufacturing Technology*, vol. 7, no. 5, pp. 786–791, 2017.
- [10] D. Sankaranarayanan, D. Venkatakirana, and B. Mukherjee, "A novel compact fractal ring based cylindrical dielectric resonator antenna for ultra wideband application," *Progress In Electromagnetics Research C*, vol. 67, pp. 71–83, 2016.
- [11] D. Sankaranarayanan, D. Venkatakirana, and B. Mukherjee, "Koch snowflake dielectric resonator antenna with periodic circular slots for high gain and wideband applications," in *Proceedings of the 2016 URSI Asia-Pacific Radio Science Conference (URSI AP-RASC)*, pp. 1418–1421, Seoul, South Korea, August 2016.
- [12] D. Sankaranarayanan, D. V. Kiran, and B. Mukherjee, "Koch snowflake Dielectric Resonator Antenna loaded with a circular metallic patch for wideband applications," in *Proceedings of the 2016 URSI Asia-Pacific Radio Science Conference (URSI AP-RASC)*, pp. 1798–1801, Seoul, South Korea, August 2016.
- [13] D. V. Kiran, D. Sankaranarayanan, and B. Mukherjee, "Compact minkowski half-hexagon notched dielectric resonator antenna for wideband applications," in *Proceedings of the 2016 URSI Asia-Pacific Radio Science Conference (URSI AP-RASC)*, pp. 1787–1790, Seoul, South Korea, August 2016.
- [14] W. L. Chen, G. M. Wang, and C. X. Zhang, "Small-size microstrip patch antennas combining koch and sierpinski fractal-shapes," *IEEE Antennas and Wireless Propagation Letters*, vol. 7, pp. 738–741, 2008.
- [15] K. C. Hwang, "A modified sierpinski fractal antenna for multiband application," *IEEE Antennas and Wireless Propagation Letters*, vol. 6, no. 1, pp. 357–360, 2007.
- [16] A. Jamil, M. Z. Yusoff, N. Yahya, and M. A. Zakariya, "A compact multiband hybrid meander-Koch Fractal antenna for WLAN USB dongle," in *Proceedings of the 2011 IEEE Conference on Open Systems*, pp. 290–293, Langkawi, Malaysia, September 2011.
- [17] R. A. Kumar, Y. K. Choukiker, and S. K. Behera, "Design of hybrid fractal antenna for UWB application," in *Proceedings of the 2012 Int. Conf. Comput. Electron. Electr. Technol. ICCEET 2012*, pp. 691–693, Nagercoil, India, March 2012.
- [18] N. Sharma, V. Sharma, and S. S. Bhatia, "A novel hybrid fractal antenna for wireless applications," *Progress In Electromagnetics Research M*, vol. 73, pp. 25–35, 2018.
- [19] Y. Kumar and S. Singh, "A compact multiband hybrid fractal antenna for multistandard mobile wireless applications," *Wireless Personal Communications*, vol. 84, no. 1, pp. 57–67, 2015.
- [20] M. Kaur and J. S. Sivia, "Ann and fa based design OF hybrid fractal antenna for ISM band Applications," *Progress In Electromagnetics Research C*, vol. 98, pp. 127–140, 2020.
- [21] I. S. Bangi and J. S. Sivia, "Moore, minkowski and koch curves based hybrid fractal antenna for multiband Applications," *Wireless Personal Communications*, vol. 108, no. 4, pp. 2435–2448, 2019.
- [22] S. S. Sran and J. S. Sivia, "ANN and IFS based wearable hybrid fractal antenna with DGS for S, C and X band application," *AEU - International Journal of Electronics and Communications*, vol. 127, Article ID 153425, 2020.
- [23] R. A. Lituma-Guarta, J. B. Benavides-Aucapifia, D. F. Poveda-Pulla, L. F. Guerrero-Vasquez, and P. A. Chasi-Pesántez, "A novel hybrid fractal antenna design for ultra-wideband application," in *Proceedings of the 2018 IEEE 10th Latin-American Conference on Communications (LATIN-COM)*, pp. 1–5, Guadalajara, Mexico, November 2018.
- [24] I. S. Bangi and J. S. Sivia, "Minkowski and Hilbert curves based hybrid fractal antenna for wireless applications," *AEU - International Journal of Electronics and Communications*, vol. 85, pp. 159–168, 2018.
- [25] S. Rani and A. P. Singh, "A novel design of hybrid fractal antenna using BFO," *Journal of Intelligent and Fuzzy Systems*, vol. 27, no. 3, pp. 1233–1241, 2014.
- [26] S. R. Best, "On the performance of the Koch fractal and other bent wire monopoles as electrically small antennas," in *Proceedings of the IEEE Antennas and Propagation Society International Symposium (IEEE Cat. No.02CH37313)*, pp. 534–537, San Antonio, TX, USA, June 2002.
- [27] L. Schulwitz, "The small koch fractal monopole: theory, design and applications," *Eng. Comput. Sci. Univ. Michigan*, vol. 4, pp. 1–12, 2005, <http://scholar.google.com/scholar?hl=en&btnG=Search&q=intitle:The+Small+Koch+Fractal+Monopole:+Theory+design+and+applications#1>.
- [28] K. J. Vinoy, J. K. Abraham, and V. K. Varadan, "On the relationship between fractal dimension and the performance of multi-resonant dipole antennas using koch curves," *IEEE Transactions on Antennas and Propagation*, vol. 51, no. 9, pp. 2296–2303, 2003.
- [29] C. Puente, J. Romeu, R. Pous, J. Ramis, and A. Hijazo, "Small but long Koch fractal monopole," *Electronics Letters*, vol. 34, no. 1, pp. 9–10, 1998.
- [30] S. Rani and A. P. Singh, "On the design and optimisation of new fractal antenna using PSO," *International Journal of Electronics*, vol. 100, no. 10, pp. 1383–1397, 2013.

## Corrigendum

# Corrigendum to “Square-Framed *T* Shape mmwave Antenna Array at 28 GHz for Future 5G Devices”

**Saad Hassan Kiani,<sup>1</sup> Xin Cheng Ren,<sup>2</sup> Adil Bashir,<sup>3</sup> Muhammad Rizwan Anjum,<sup>4</sup> Ammar Rafiq,<sup>5</sup> Mian Muhammad Kamal,<sup>6</sup> Burhan Ud Din,<sup>1</sup> and Fazal Muhammad<sup>7</sup>**

<sup>1</sup>Electrical Engineering Department, City University of Science and Information Technology, Peshawar 25000, Pakistan

<sup>2</sup>School of Physics and Electronic Information, Yanan University, Yanan 761000, China

<sup>3</sup>Electrical Engineering Department, Bahauddin Zakariya University, Multan, Pakistan

<sup>4</sup>Department of Electronic Engineering, The Islamia University of Bahawalpur, Bahawalpur 63100, Pakistan

<sup>5</sup>Department of Computer Science, NFC Institute of Engineering & Fertilizer Research, Faisalabad, Pakistan

<sup>6</sup>School of Information Engineering, Zhengzhou University, Zhengzhou 450001, China

<sup>7</sup>Department of Electrical Engineering, University of Engineering Technology, Mardan 23200, Pakistan

Correspondence should be addressed to Xin Cheng Ren; [chren@yau.edu.cn](mailto:chren@yau.edu.cn)

Received 16 December 2021; Accepted 16 December 2021; Published 5 January 2022

Copyright © 2022 Saad Hassan Kiani et al. This is an open access article distributed under the Creative Commons Attribution License, which permits unrestricted use, distribution, and reproduction in any medium, provided the original work is properly cited.

In the article titled “Square-Framed *T* Shape mmwave Antenna Array at 28 GHz for Future 5G Devices” [1], the order of the author names has been incorrectly published and the correct order is found above.

## References

- [1] S. H. Kiani, X. C. Ren, B. Adil et al., “Square-framed *T* shape mmwave antenna array at 28 GHz for future 5G devices,” *International Journal of Antennas and Propagation*, vol. 2021, Article ID 2286011, 9 pages, 2021.

## Research Article

# Novel Compact Design and Investigation of a Super Wideband Millimeter Wave Antenna for Body-Centric Communications

**H. M. Arifur Rahman** <sup>1</sup>, **Mohammad Monirujjaman Khan** <sup>1</sup>, **Mohammed Baz** <sup>2</sup>,  
**Mehedi Masud** <sup>3</sup>, and **Mohammed A. AlZain** <sup>4</sup>

<sup>1</sup>Department of Electrical and Computer Engineering, North South University, Dhaka-1229, Bangladesh

<sup>2</sup>Department of Computer Engineering, College of Computers and Information Technology, Taif University, P. O. Box 11099, Taif 21944, Saudi Arabia

<sup>3</sup>Department of Computer Science, College of Computers and Information Technology, Taif University, P.O. Box 11099, Taif 21944, Saudi Arabia

<sup>4</sup>Department of Information Technology, College of Computers and Information Technology, Taif University, P. O. Box 11099, Taif 21944, Saudi Arabia

Correspondence should be addressed to Mohammad Monirujjaman Khan; [monirujjaman.khan@northsouth.edu](mailto:monirujjaman.khan@northsouth.edu)

Received 22 August 2021; Accepted 2 November 2021; Published 18 November 2021

Academic Editor: Muhammad Inam Abbasi

Copyright © 2021 H. M. Arifur Rahman et al. This is an open access article distributed under the Creative Commons Attribution License, which permits unrestricted use, distribution, and reproduction in any medium, provided the original work is properly cited.

This paper presents a novel design for a multiple band millimeter wave antenna with a wide active region in the extremely high frequency (EHF) range. The antenna's performance was tested at three evenly separated frequencies: 60 GHz within the V-band region, 80 GHz within the E-band region, and 100 GHz. Simulation exhibits satisfactory results in terms of gain and efficiency, although the efficiency falling tendency for higher frequency persists. As millimeter wave antennas have miniature-like dimensions and low penetration depth into human body layers, the performance of these antennas is less disturbed by the presence of a human body, making them ideal for body-centric wireless communication (BCWC) applications. Thus, a human body model was created virtually with the necessary property data. Simulations are repeated at the same frequencies as before, with the antenna kept close to the constructed human body model. The results were promising as the gains found increased radiation patterns and return loss curves remained almost identical, except some efficiencies that were considered. Some H-plane radiation patterns are changed by the presence of a human body. Although all three frequencies present satisfactory results, 60 GHz is found to be more balanced, but 100 GHz shows better gain and directivity. Multiple band operability makes this antenna suitable for various applications. Finally, a distance-based analysis was conducted to realize the in-depth characteristics of the antenna by placing the antenna at five different gaps from the human body. The result verifies the antenna's category as suitable for body-centric communications.

## 1. Introduction

The millimeter wave, also known as mmWave or millimeter band, is a popular research sector for telecommunication researchers because of its numerous advantages over other lower frequency bands. The spectrum covers the 30 GHz to 300 GHz frequency range, having wavelengths of 10 mm to 1 mm, from where the name came. The International Telecommunication Union (ITU) refers to this frequency

range as extremely high frequency (EHF) because of its extremely higher frequency spectrum.

Millimeter band electromagnetic waves suffer from atmospheric attenuation, which causes them to gradually degrade as they propagate through the environment or air. This attenuation is mostly the result of absorption by environmental components, such as gases and humidity. Absorption increases as the frequency increases, and maximum frequencies can only remain active within several

meters of distance. Radio waves exhibit better performance in less humid environments. Apart from this limitation, millimeter waves can be highly effective in short-range distances. This limitation also enables designers to reuse frequency to increase efficiency. To utilize this potential, cell sizes are reduced, occupied by fewer cellular network clients. Access point numbers can be higher in short-range operations.

Millimeter wave signals can be used in an extensive area of operation. Antennas designed for mmWaves have very small form factors, which allows them to be equipped with a variety of mobile and wireless network devices and services. mmWave antennas are also known to consume less power and are more power-efficient during operation. These signals are capable of achieving extremely high data transfer rates compared to the smaller frequency bands, which makes them suitable for point-to-point (P2P) high-speed wireless local area network operations. They are currently being used in military operations, security scanners, fire detection radars, airports, and many other short-distance wireless Internet of things, IoT devices, and scientific research [1].

Within the huge spectrum of mmWave, the V-band of 60 GHz, more precisely 57 GHz to 54 GHz, is kept unlicensed by the Federal Communications Commission (FCC). Due to the lack of various device implementations, this band remains low in traffic worldwide. Because of the permitted accessibility and its other advantages, researchers worldwide are heavily interested in this frequency band. But it has a few drawbacks compared to other frequency bands in the millimeter wave range. This frequency band coincides with the harmonics of the oxygen molecules in the air and thus gets absorbed so easily into the Earth's terrestrial environment. So the bandwidth delivery distance becomes shorter at this particular frequency [1, 2]. The range of 70 to 80 GHz of the E-band is also made publicly accessible by the FCC with an easy licensing procedure. In June 2020, the American aerospace manufacturer and space transportation service, SpaceX, applied for the utilization of this band for their orbital deployment and operating authority for the SpaceX Gen2 NGSO satellite system [3]. However, in environments without obstacles like brick walls or metal barriers, and for short-range operations, millimeter waves can achieve an extremely high data transfer rate between portable electronic devices, which can be used for fast file transfer, high definition video streaming, short-range wireless fidelity (WiFi), and much more. Such environments can be found in halls or in medical wards in a hospital.

For body-centric communication, several sensor nodes are placed on, inside, or in close proximity to the human body to collect vital information and send it to a common node where the data is fetched. Mostly, these collected data need to be either stored on a base station computer or sent to a distantly located doctor or physician or to a monitoring healthcare center. Tiny microchip antennas are used as the medium as the sensor nodes are dispersed throughout the body and wires will make it more sophisticated or sometimes impossible to maintain a connection. As a result, it is more commonly known as the body-centric wireless network (BCWN), which is also associated with the wireless body

area network (WBAN). These are specially used for medical purposes to distantly monitor someone's vital signs like heartbeat rate, blood pressure, electrocardiogram (ECG), or peripheral oxygen saturation (SpO<sub>2</sub>) reading collection. In healthcare centers, these can also be used for athletes in sports or astronauts in space [4].

As antennas play a key role in body-centric wireless communication, researchers must keep in mind while designing an antenna how it will perform when it is in close proximity to a human body. Antennas near the human body behave differently than they do in free space. The capacitive properties of the human body are most likely to disturb the performance as well as the efficiency of the antenna [5–7]. The presence of a human body close to an antenna has a notable influence on the radiation efficiency, resonant frequency, radiation patterns, and the input impedance of the model [5–7]. To simulate the performance of an antenna close to a human body, a human body model should be created consisting of three different layers: a thinner skin layer with a loss tangent of 1.37, a comparatively less thin fat layer with a loss tangent of 0.27 adjacent to it, and a muscle layer with a loss tangent of 0.0012, respectively [8].

Christophe Calvez et al. previously characterized and analyzed millimeter wave antenna solutions for 60 GHz operation using both SoC (System on Chip) and SiP (System in Package) techniques. Comparing a planar dipole antenna on chip (SoC) with a silicone substrate and Si-IPD in a package antenna, researchers found SiP antennas can achieve better gains and are mostly suitable for industrial use [9]. A very simple rectangular-shaped patch antenna was designed by Adamu [10]. It is powered by a coaxial probe feed, operates at 38 GHz, and is claimed to have 90% power efficiency. Choi et al. have designed a miniature mmWave 5G antenna and fabricated it with anodized aluminum oxide (AAO). Researchers claimed they had used 99.99% pure aluminum thin sheet, which reduces the antenna volume and weight, making it suitable for mobile devices. The antenna operates at 29 GHz and has a gain of 5.02 dB to 5.62 dB [11].

Many researchers have tried to design a flawless millimeter wave antenna with high gain and efficiency in the past decade, but very few of them have performed satisfactorily when it comes to the human body. The antenna must perform at least within an excellent operable region for body-centric wireless communication. A mmWave antenna consisting of two identical patch arrays set up face-to-face 19.5 cm apart fed by a coaxial feed launcher operates within the 37 to 39 GHz frequency range with an optimized gain by Cheng-Nan Hu et al. [12] but has an unknown performance near the human body, as the model does not appear to be suitable for BCWN. Heba Shawkey and Dalia Elsheakh suggest a dual-meander line (DML) antenna for body-centric networks and biomedical applications that works in several bands: 22 GHz, 34 GHz, 44 GHz, and 58 GHz. The design used a UMC 180 nm complementary metal oxide semiconductor (CMOS) fabrication process with a low-resistivity silicon substrate and an interdielectric layer embedded with six metal layers. A dielectric passivation layer was applied to the M6 top metallic surface

TABLE 1: Electrical size at different frequencies.

Material	Physical size (mm)	Electrical size at 60 GHz ( $\lambda$ )	Electrical size at 80 GHz ( $\lambda$ )	Electrical size at 100 GHz ( $\lambda$ )
Length of the substrate	8	0.625	0.468	0.375
Width of the substrate	5.2	0.96	0.72	0.576
Height of the substrate	1.57	3.18	2.388	1.91
Length of the radiating element	3.178	1.57	1.179	0.94
Width of the radiating element	2.432	2.055	1.54	1.233
Height of the radiating element	0.035	142.85	107.14	85.71

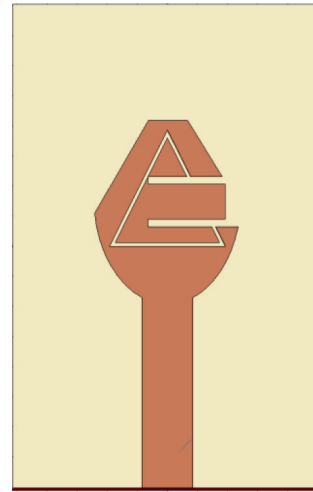
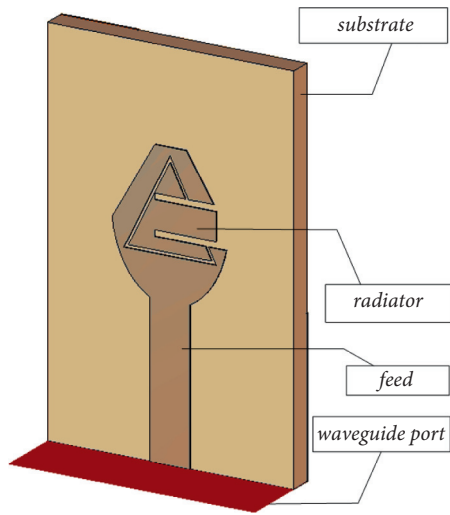
[13]. To compare the human body effect, simulations placed the antenna inside and over the human body and observed the downshift of the resonant frequency and operating bandwidth increment. A textile antenna for wearable body-centric networks has been presented by Chahat et al., which operates in the mmWave frequency range. It was claimed to be the first time that it was implemented with a hybrid textile substrate and that it operates at a frequency range of 57 GHz to 64 GHz [14]. The authors of [15] presented a novel and compact shaped textile substrate for body-centric communications based on a 60 GHz mmWave antenna. A comparison of antenna performance parameters was conducted utilizing various textile substrates. The proposed antenna of the paper [15] was also tested by placing it on a three-layer human body model. In [16], a Yagi-Udah cotton-based mmWave antenna for on-body communication was presented. The antenna works at 60 GHz and it is bigger in size. According to the authors in [17], a printed antenna for mmWave body-centric communication is presented which operates at 60 GHz. The antenna has a length and width of  $14 \times 10.5$  mm.

The major contribution of this paper is to propose a novel and compact design for a multiband and super wideband mmWave antenna, and its free space and human body performance are simulated and compared. Performance was tested at three different frequencies (60 GHz, 80 GHz, and 100 GHz) within the popular mmWave range. A virtual human body model was created consisting of layers to evaluate its performance over a human body at the same frequencies as the body-centric network. According to the reported literatures in this manuscript, it is noted that most of the mmWave antennas are bigger in size, and they work at lower frequency bands. The maximum operating frequency band was 60 GHz in the presented literatures. However, the proposed antenna is the smallest mmWave antenna to the best of knowledge of the authors of this paper. The overall length and width of this antenna is 8 and 5.2 mm, respectively. The antenna is novel because it works multiple band at the higher frequency bands, and it has super wideband characteristics. In previous studies, researches have not investigated 60 GHz, 80 GHz, and 100 GHz multiband compact and wideband antenna for BCWC. This proposed antenna presents very good performance. Hence, this antenna beats the state of the arts and is considered to be the novel antenna in BCWC application.

The remainder of the paper is divided into the following sections: The antenna's design is described in Section 2. Section 3 includes free space simulation in different bands and performance parameters. In Section 4, human body performance compared to free space was presented. Section 5 contains the evaluation of BCWC compatibility by distance-based study, and, finally, in Section 6, the conclusion was drawn based on the result comparisons.

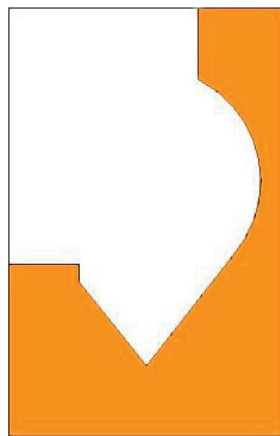
## 2. Antenna Design

Computer Simulation Technology (CST) Microwave Studio Suite was used to build and test the antenna design. The radiating element, substrate, and ground plane were the three neighboring planner components in the model. The overall length and width of the antenna are 8 mm and 5.12 mm, respectively. The total thickness of all three layers is 1.57 mm, while the radiating patch is 0.035 mm, the substrate is 1.5 mm, and the ground is 0.035 mm thick, respectively. The wavelength of the antenna for the operating frequencies of 60 GHz, 80 GHz, and 100 GHz is 5 mm, 3.75 mm, and 3 mm, respectively. Table 1 summarizes the electrical size of the antenna at different frequencies. Figures 1(a)–1(e) show the antenna design, parameters, and front and back views with detailed dimensions. The substrate is made of flame retardant fiberglass reinforced epoxy (FR-4) with a dielectric constant of 3. An inverted lotus petal-shaped cutout ground plane actually consists of four parts: a circular part, a triangular cutout at the bottom of it, a top-left rectangular shape cutout, and an added small rectangular brick on that cutout pace. Annealed copper was selected for the ground. The radiator patch is placed on the upper side of the substrate with a feed line and a waveguide port at the base for source excitation. The feed line is 3.136 mm long and 0.832 mm wide. The elliptical half-cylinder has a radius of 1.216 mm and a vertical axis radius of 1.76 mm. A 0.064 mm wide equilateral triangular slot 1.92 mm of each arm is cut in the middle for a better response. The middle rectangle is 1.28 mm long and 0.576 mm tall, with 0.128 mm slots on top and bottom. On the opposite side of the substrate, the circular slot is centered in the middle horizontally but vertically 4.768 mm higher from the bottom. The radius of the circular shape is 2.128 mm. The rectangular cutout has a dimension of 5.12 mm  $\times$  3.52 mm. The length of the bottom triangular extruded sides has been given in Figure 1(e).

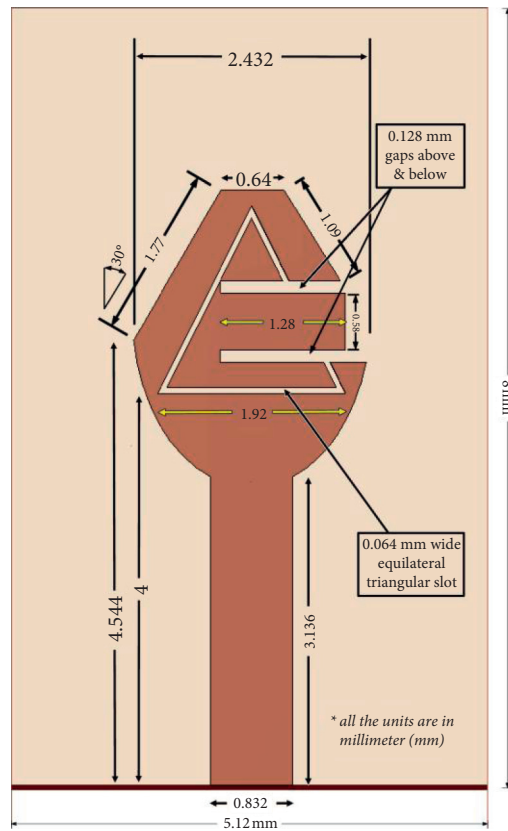


(a)

(b)



(c)



(d)

FIGURE 1: Continued.



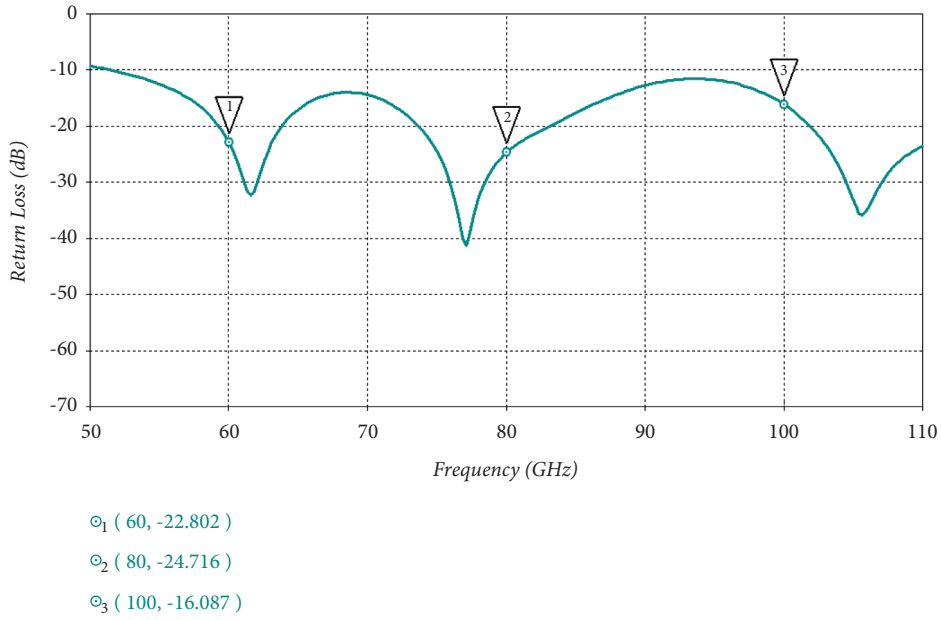


FIGURE 2: Free space return loss.

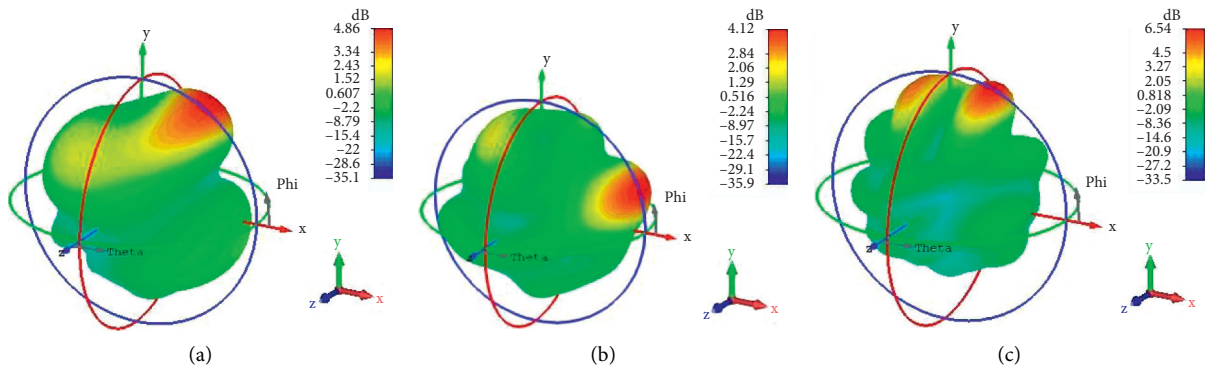


FIGURE 3: 3D radiation patterns at (a) 60 GHz, (b) 80 GHz, and (c) 100 GHz (from left to right).

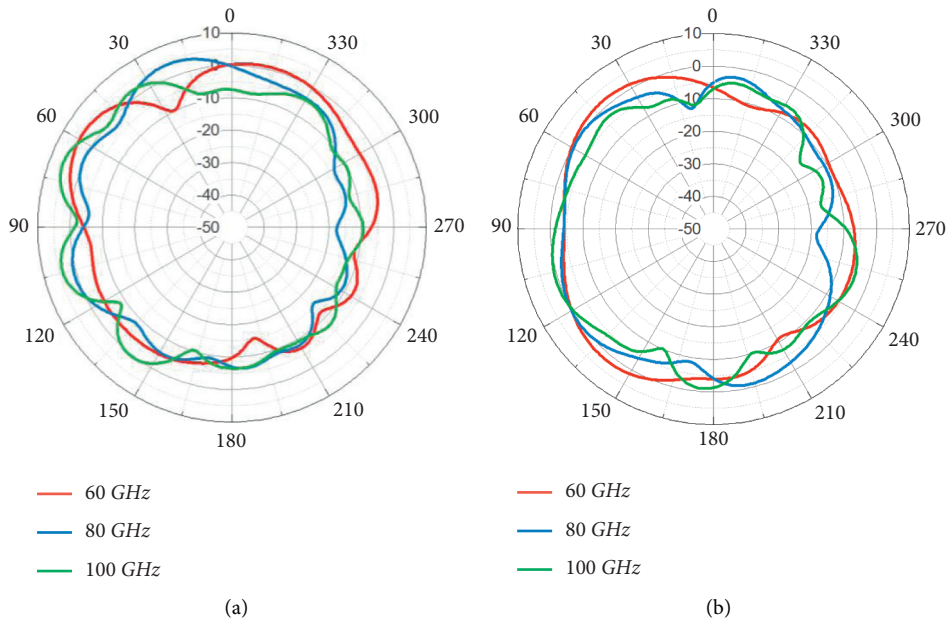


FIGURE 4: Polar plot radiation patterns of different planes: (a) XY-plane and (b) YZ-plane.

100 GHz, the main lobe directions are  $58^\circ$ ,  $21^\circ$ , and  $69^\circ$ , respectively. Lobe magnitudes were found at 4.33 dB for 60 GHz with an angular width of 33.3 degrees, 4.11 dB for 80 GHz with an angular width of 32.2 degrees, and 5.779 dB for 100 GHz with an angular width of 21.1 degrees. Figure 4(b) shows the two-dimensional patterns for all three frequencies in the YZ-plane. For 60 GHz, 80 GHz, and 100 GHz, the main lobe directions are at  $140^\circ$ ,  $124^\circ$ , and  $109^\circ$ , respectively. Lobe magnitudes were found at 1.97 dB for 60 GHz with an angular width of 47.9 degrees, 0.365 dB for 80 GHz with an angular width of 43.0 degrees, and 0.745 dB for 100 GHz with an angular width of 42.1 degrees. The antenna shows stability at all three frequencies, though it provides better gain and directivity at 100 GHz. The XY- and YZ-plane radiation patterns for 60 GHz and 80 GHz are comparable, but at 100 GHz they look slightly distorted.

**3.3. VSWR.** Figure 5 shows the free space voltage standing wave ratio curve over the frequency span of 50 to 110 GHz. Since the antenna has a wide bandwidth at  $-10$  dB return loss, it shows good impedance matching. Hence, the VSWR of the antenna over the wide frequency range shows good values. The voltage standing wave ratio (VSWR) values for three observing frequencies are 1.1564, 1.1234, and 1.3724 for 60 GHz, 80 GHz, and 100 GHz, respectively. In comparison with these three selected frequencies (60 GHz, 80 GHz, and 100 GHz), the VSWR value is noticed to be slightly higher at 100 GHz.

**3.4. Gain and Efficiency.** Table 2 shows the values of gain, efficiency, and VSWR of three different frequencies of the antenna. From Table 2, it is observed that the antenna displays an overall better gain at 100 GHz with 5.779 dB. At 60 GHz, the gain is slightly lower than that of 100 GHz, but satisfactory. The gain in the E-band is a bit lower than the other two, but still above 4 dB. In terms of efficiency, it shows that as the frequency increases, efficiency falls gradually. The higher radiation efficiency is noticed at 60 GHz as compared with 100 GHz.

## 4. On-Body Simulation

A three-layer human body model was developed to test the antenna's on-body performance. For the convenience of the simulation, three outermost layers of the human body have been taken into account, which will be closer to the antenna. Skin, fat, and muscle are the three layers. A skin model with a skin thickness of 1.3 mm was created with its dielectric and other properties. Similarly, the fat layer is made with a thickness of 2 mm, and the muscle layer, which is the inner and the heavier one, is made with a thickness of 10 mm. The height and width of the whole human body model are  $10 \text{ mm} \times 14 \text{ mm}$ . All the layers are then placed sequentially without any gaps, like a real human body. Figures 6(a) and 6(b) show the created human body model with the antenna with its dimensions. The designed antenna was then placed over the human body model, keeping a distance of 4 mm. After that, simulations were done, and then the newly

simulated results were compared with the previous ones. The accounted properties (relative permittivity, loss tangent) [18] and dimensions of the three-layer human body model are shown in Table 3.

**4.1. On-Body Return Loss.** As illustrated in Figure 7, the on-body return loss curve is compared to the free space return loss. The return loss curve becomes more sharp-edged at the resonant locations and slightly left-shifted. On the observed frequencies of 60 GHz, 80 GHz, and 100 GHz, return loss values decreased from  $-22.8$  dB to  $-32.42$  dB,  $-24.72$  dB to  $-25.64$  dB, and  $-16.09$  dB to  $-17.43$  dB, respectively. However, this antenna shows good return loss responses both in free space and also on the body. Both free space and on-body return loss levels are less than  $-10$  dB at 60 GHz, 80 GHz, and 100 GHz. If we consider bandwidth at  $-10$  dB, this antenna shows super wideband impedance bandwidth, which is very good for very high-speed data transmission. Because of the presence of the human body, there are negligible effects on the on-body return loss for this proposed super wideband mmWave antenna in this research work.

**4.2. 3D Radiation Free Space and On-Body Radiation Pattern Comparison.** The comparison of free space and on-body 3D radiation patterns for 60 GHz, 80 GHz, and 100 GHz is shown in Figures 8(a)–8(f). From Figure 8, it is noted that there are very slight changes in on-body 3D radiation patterns in comparison with the on-body case. However, due to the presence of the human body model at the back of the antenna, the peak gain for on-body cases increases for all three frequencies. At 60 GHz and 80 GHz, passive lobes are detected with the existing ones with a very slight change in directivity, except for 100 GHz, which remains very stable. Gain increased in all three frequencies while it is close to the human body model. For 60 GHz, it has now increased to 5.39 dB from 4.86 dB. Similarly, for 80 GHz, it has shifted to 4.69 dB from 4.12 dB, and for 100 GHz, it recorded 7.01 dB from 6.54 dB.

**4.3. Comparison of Free Space and On-Body Polar Plot Radiation Patterns.** Figures 9(a)–9(f) illustrate a comparison of polar plot free space and on-body radiation patterns for the XY- and YZ-planes at 60 GHz, 80 GHz, and 100 GHz. It is noted that in both planes, the radiation patterns do not change much but the power level does. Figure 9 present the radiation pattern changes after placing the antenna 4 mm apart from the human body on two different planes at 60 GHz, 80 GHz, and 100 GHz. Three figures from the top row of the XY-plane show the changes are very slight in the patterns for all three frequencies. The main lobe and side lobe directions are almost identical except for some gain value changes. After placing the antenna close to the human body model, on the XY-plane, at 60, 80, and 100 GHz, the main lobe magnitudes are now 5.13 dB, 4.71 dB, and 7.01 dB, respectively. The primary lobe directions are  $58^\circ$ ,  $21^\circ$ , and  $70^\circ$  in the same order. Similarly,

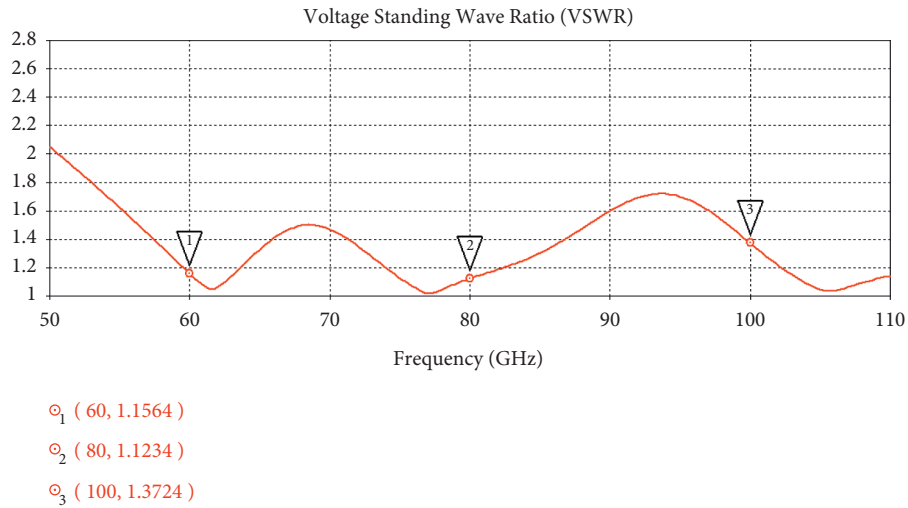


FIGURE 5: Free space voltage standing wave ratio curve.

TABLE 2: Gain and radiation efficiency.

Frequencies	60 GHz	80 GHz	100 GHz
Radiation efficiency (%)	70.65	63.96	57.31
Total efficiency (%)	70.28	63.74	55.89
VSWR	1.1564	1.1234	1.3724
Gain (dB)	4.669	4.125	5.779

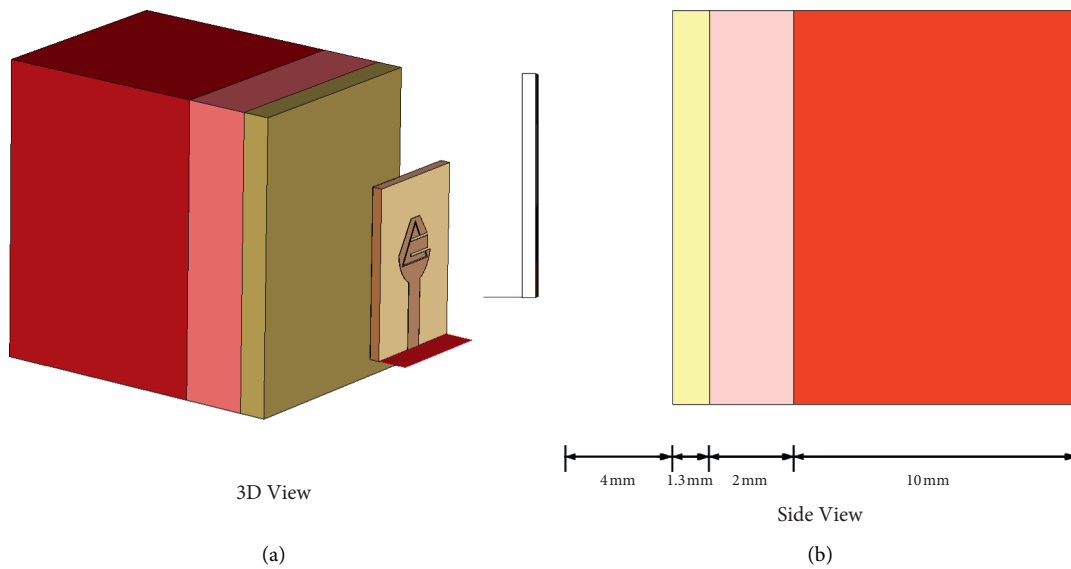


FIGURE 6: Antenna with human body model: (a) 3D view and (b) side view.

TABLE 3: Modeled human body layer parameters and properties.

Layers	Skin	Fat	Muscle
Length (mm)	14	14	14
Width (mm)	10	10	10
Thickness (mm)	1.3	2	10
Ave. penetration depth (mm)	0.48	3.37	0.41
Relative permittivity	7.9753	3.1324	2.8152
Loss tangent	1.37	0.27	0.0012
Conductivity (S/m)	36.397	2.8152	52.825

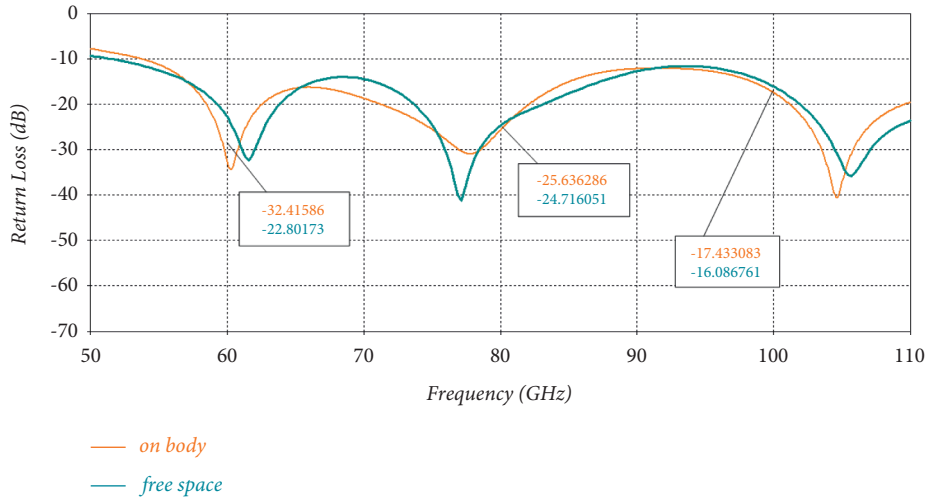


FIGURE 7: Comparison curves for free space and on-body return loss.

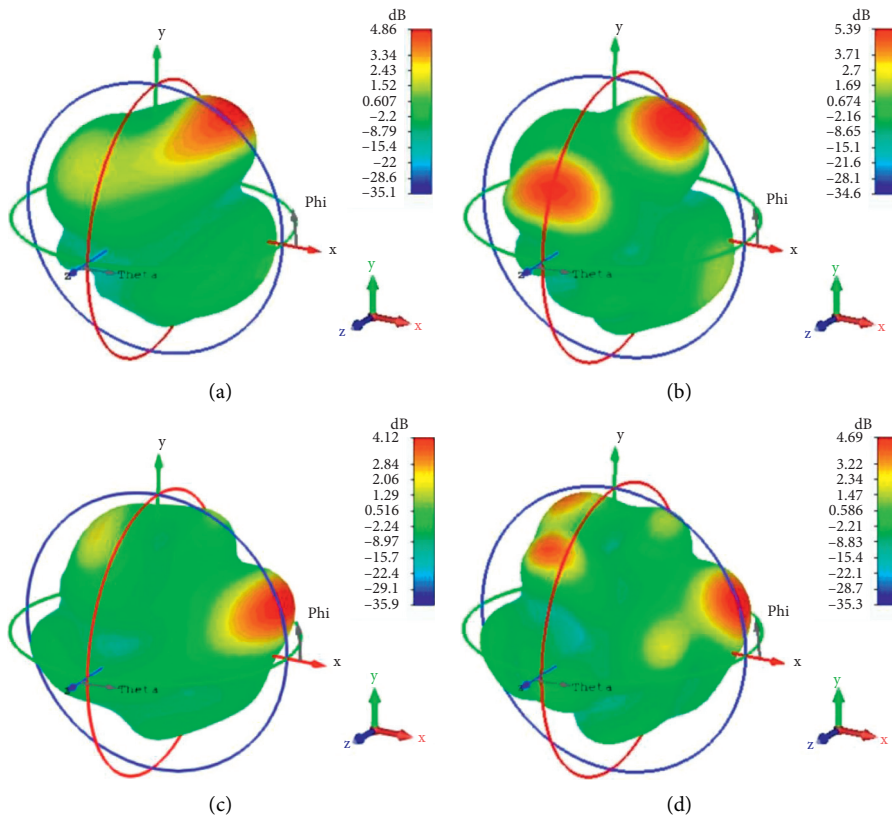


FIGURE 8: Continued.

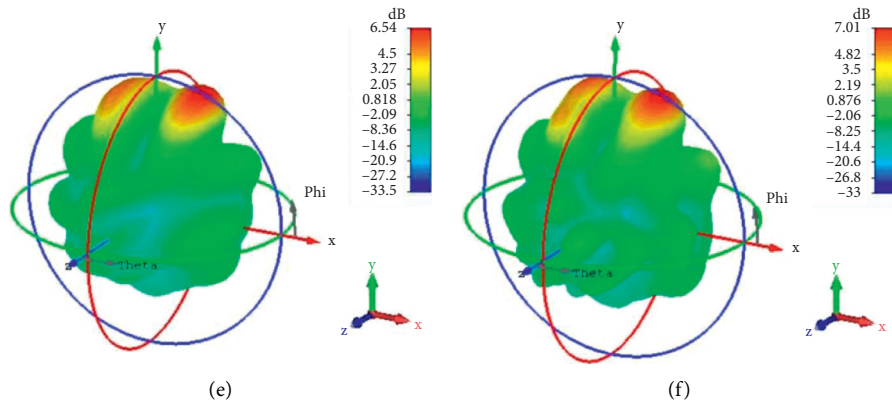


FIGURE 8: : 3D radiation pattern comparison: (a) free space 60 GHz, (b) on-body 60 GHz, (c) free space at 80 GHz, (d) on-body at 80 GHz, (e) free space at 100 GHz, and (f) on-body at 100 GHz.

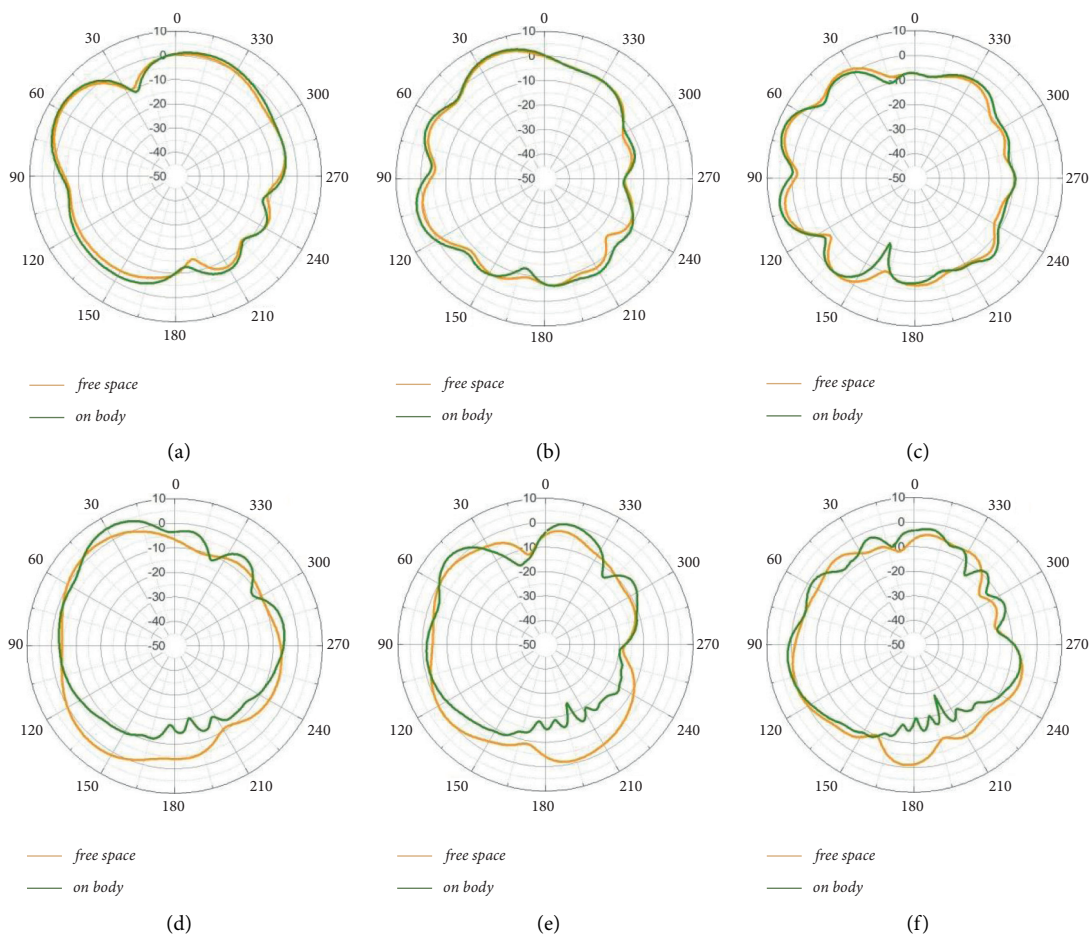


FIGURE 9: Free space versus on-body radiation pattern comparison: (a) XY-plane at 60 GHz, (b) XY-plane at 80 GHz, (c) XY-plane at 100 GHz, (d) YZ-plane at 60 GHz, (e) YZ-plane at 80 GHz, and (f) YZ-plane at 100 GHz.

for 60, 80, and 100 GHz on the YZ-plane, the main lobe magnitudes are now 5.12 dB, 3.16 dB, and 1.75 dB with their primary lobe directions of 29°, 48°, and 99°, respectively. To have a clear view of the changes and compare them with the free space data, Table 4 has been presented.

From Table 4, it is determined that the antenna performs much better when it is closer to the human body from a radiation perspective. The results on the XY-plane are very stable in both free space and on-body conditions. Only some variations in gain and directivity can be

TABLE 4: Comparison of polar plot radiation patterns at different angles: lobe-wise (FS, free space and OB, on-body).

Frequency and planes	60 GHz				80 GHz				100 GHz			
	XY		YZ		XY		YZ		XY		YZ	
	FS	OB	FS	OB	FS	OB	FS	OB	FS	OB	FS	OB
Primary lobe magnitude (dB)	4.33	5.13	1.97	5.12	4.11	4.71	0.37	3.16	5.77	7.01	0.75	1.75
Primary lobe direction	58°	58°	140°	29°	21°	21°	124°	48°	69°	70°	109°	99°
Lobe width (degree)	33.3	34.8	47.9	30.2	32.2	33.2	43	21.9	21.1	19.7	42.1	36.4
Side lobe level (dB)	-3.5	-3.2	-5.9	-6.8	-3.3	-1.5	-1.5	-3.0	-1.7	-1.0	-1.7	-3.2

noticed on the H-plane (YZ). It needs to be mentioned that the table data for “primary lobe magnitude” is rounded up to two decimal places, while others are rounded up to one.

**4.4. On-Body versus Free Space VSWR Comparison.** After placing the antenna 4 mm above the created human body model, the VSWR curve was calculated again and compared with the previously generated “free space” curve. Figure 10 shows the comparison of free space and on-body VSWR curves. The on-body VSWR curve pattern is nearly similar to the free space one, but the on-body curve is noticed to be slightly left-shifted. For the three observing frequencies, results have become much better for 60 GHz, which is down to 1.049 from 1.156 now. At 80 GHz, both free space and the body curve get intertwined, and values are very close. At 100 GHz, it is 1.31, which is better than the 1.37 for free space.

**4.5. Gain, VSWR, and Efficiency Comparison.** In Table 5, on-body simulated gain, VSWR, and efficiency results were compared with the previously recorded free space simulation data. Due to the lossy nature of the human body, efficiencies are reduced for on-body scenarios. Lossy tissues of the human body absorb radiation power, which results in a reduction of efficiency from the free space when an antenna is placed on the body. Almost 8% of radiation efficiency is reduced at all three frequencies, which indicates that the gradual increment of frequencies alongside the gradual decrease in efficiency does not have a proportional effect on the antennas surrounding the human body. Voltage standing wave ratio at 60 GHz looks more revised in on-body simulation. In terms of gain, on-body performance data outpaced free space performance in all three frequencies. For all three frequencies (60 GHz, 80 GHz, and 100 GHz), the gain increases when the antenna is placed on the body. However, at a higher frequency, at 100 GHz, the on-body gain is noticed to be the highest (7.007 dB).

All the designs and the results in this study are based on computer simulation using professional simulation software, CST Microwave Studio. Unfortunately, these simulated results could not be verified with a real-life fabricated one for lack of scope. However, many published articles have justified their CST Microwave Studio simulated results with real-life measurements and found similar outcomes [19–22].

## 5. Distance-Based Study

To have a clear concept of the effects of the presence of the human body in close proximity to the antenna clearly, a distance-based study was conducted. The antenna was positioned at five different distances from the human body model in this investigation, and the return loss, radiation patterns, and other variables were simulated to see how they were influenced. The results are achieved by placing the antenna 0 mm (close contact), 2 mm, 4 mm, 6 mm, and finally 8 mm apart from the human body and comparing with free space data. This section is based on the distance-based analysis of those results to understand the characteristics of the proposed super wideband mmWave antenna more precisely.

**5.1. Return Loss.** The antenna’s simulated return loss curves at five various distances from the human body model with a free space return loss curve are shown in Figure 11. The green curve with triangular marks represents the return loss of 0 mm and is clearly distinguishable from others. It is observed that when the antenna is placed directly on the body, the return loss graph changes dramatically as compared to the free space one. As the antenna is taken 2 mm or more away from the human body, the return loss curve becomes nearly stable. For 6 mm and 8 mm distances, the impact of the human body on the antenna’s return loss curve is very low. The major shape shifting of return loss is done from a distance of 0 mm to 2 mm. It is clear that the variation in the antenna distance from the human body model has an effect on the return loss for this super wide band compact antenna. When the antenna is very close to the body, the effect is stronger, and when it is farther away, the effect is weaker. However, the return loss values for 60 GHz, 80 GHz, and 100 GHz are all less than  $-10$  dB in all circumstances.

**5.2. Radiation Patterns of Different Planes.** In Figures 12(a)–12(f), the polar plot radiation patterns of this antenna are shown in the XY- and XZ-planes for three different frequencies (60 GHz, 80 GHz, and 100 GHz) while the antenna was placed at five different distances (0 mm, 2 mm, 4 mm, 6 mm, and 8 mm). In these graphs of Figures 12(a)–12(f), the free space polar plot radiation patterns are also included for comparison purposes. The radiation pattern is substantially altered, while the antenna is situated 0 mm away from the body, as seen in Figures 12(a)–12(c) in the XY-plane. The main lobe magnitudes at 60 GHz,

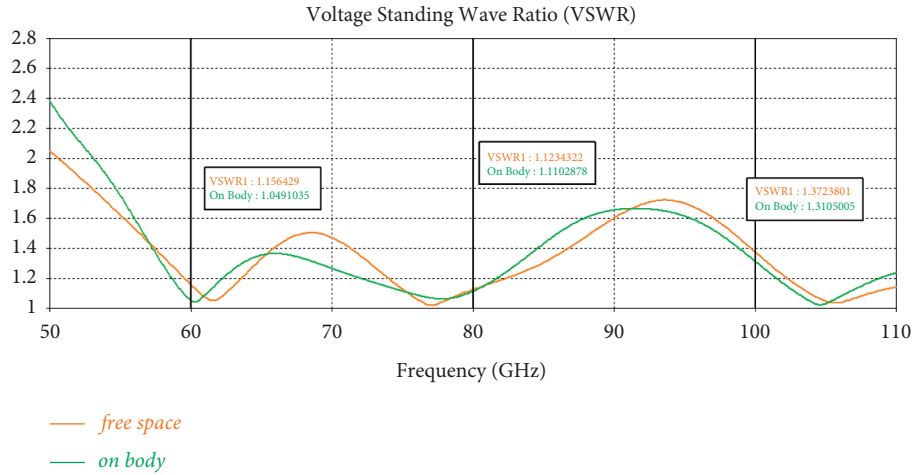


FIGURE 10: Free space versus on-body VSWR curves.

TABLE 5: Gain, VSWR, and efficiency comparison (FS = free space and OB = on-body).

Frequencies	60 GHz		80 GHz		100 GHz	
	FS	OB	FS	OB	FS	OB
Radiation efficiency (%)	70.65	62.12	63.96	53.55	57.31	49.61
Total efficiency (%)	70.28	62.08	63.74	53.25	55.89	48.71
VSWR	1.1564	1.0491	1.1234	1.1103	1.3724	1.3105
Gain (dB)	4.669	5.394	4.125	4.688	5.779	7.007

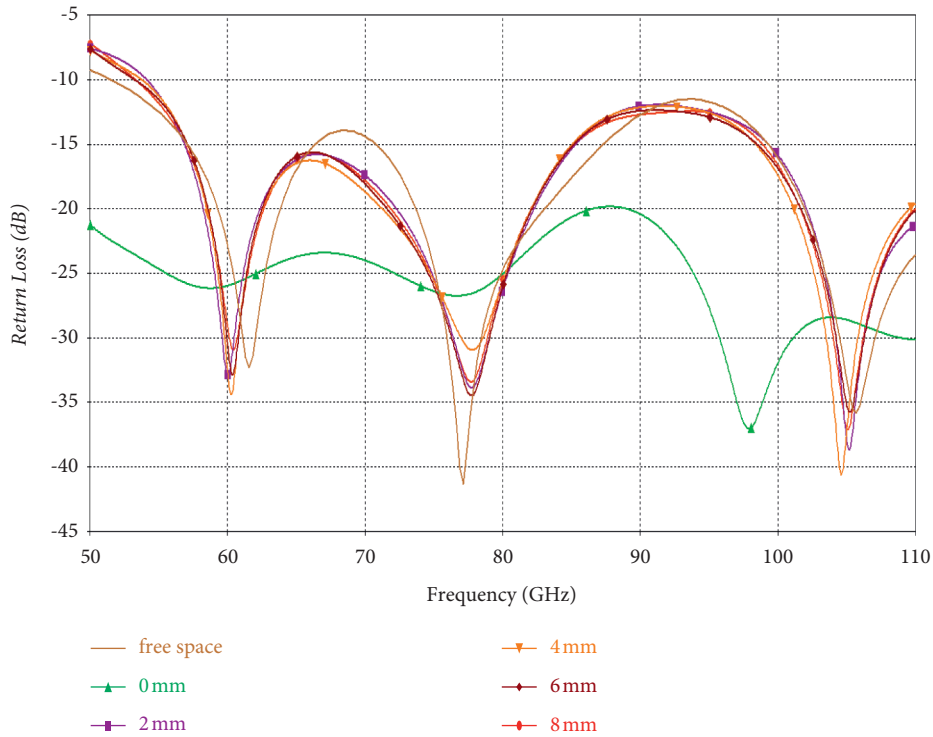


FIGURE 11: Return loss from the human body model and free space at various distances.

80 GHz, and 100 GHz are  $-11.2$  dB,  $-12$  dB, and  $-12.5$  dB, respectively. In this case, the radiation for both planes does not change much due to the close proximity of the human

body, but the power level is reduced. It is not ideal to place the antenna on the body directly. In real-life scenarios, the antenna with the wearable sensor and system will be on the

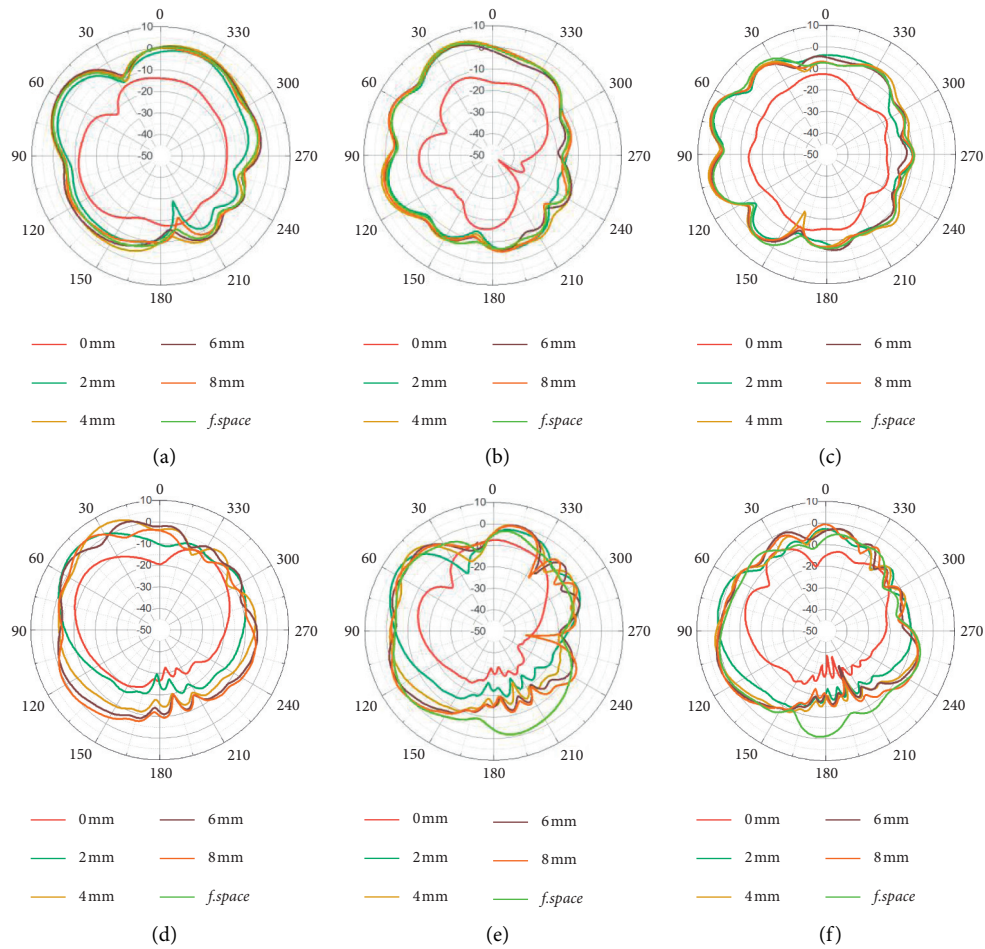


FIGURE 12: Polar plot antenna radiation patterns in the XY-plane at (a) 60 GHz, (b) 80 GHz, and (c) 100 GHz from different distances. Polar plot radiation patterns on YZ-plane at (d) 60 GHz, (e) 80 GHz, and (f) 100 GHz from different distances.

dress of the human body. For 2 mm and above distances, the radiation patterns do not change too much. Similarly, in the YZ-plane, radiation patterns are quite distinguishable at a distance of 0 mm rather than at any other distance of 2 mm or more. It shows a similar trend. However, the figure distorts a little abruptly at particular angles in the YZ-plane at higher frequencies as the distance varies. From this distance variation on-body parametric study, it is noted that even at 2 mm distance, the antenna on the body performs well in terms of XY and YZ radiation patterns, and at this distance, acceptable radiation is noticed. The power level of the radiation patterns is reported to be the lowest at 0 mm in all circumstances (antenna direct on the body).

**5.3. VSWR from Different Distances.** Figure 13 depicts the antenna VSWR at various gaps from the human body model. The free space VSWR of this antenna has also been included for comparison purposes. The green line with a triangular mark indicates the voltage standing wave ratio at a 0 mm distance from the human body model. As in the previous results, the VSWR curve also shows that the 0 mm distance curve stands separately from the others, which are 1.1, 1.12, and 1.05 at 60 GHz, 80 GHz, and 100 GHz, respectively. The

rest of the curves overlap at several frequencies on the path and fluctuate between 1.02 and 1.66 after 60 GHz.

**5.4. Investigation of Efficiency and Gain.** Table 6 shows the radiation efficiency, total efficiency, and gain comparison of the antenna at three preselected frequencies (60 GHz, 80 GHz, and 100 GHz). In Table 6, results of free space, 0 mm, 2 mm, 4 mm, 6 mm, and 8 mm, are presented. In the previous calculation of this antenna and this table, it is clearly visible that antenna performance is highly influenced when it is directly in contact with the human body. At 0 mm distance, efficiency falls from 4.96 to 4.4 at 60 GHz to 100 GHz. Nevertheless, even just a couple of millimeters away, the performance stays very stable. Therefore, the ideal distance to place this proposed antenna on the body is considered to be 2 mm away from the body. At 2 mm distance from the human body, this antenna performs very well, and the performance parameters are very much at an acceptable level. However, other distances can also be considered. Here, we have commented on the lowest minimum gap from the body to get an acceptable level of performance. At 2 mm distance, this antenna shows 56% radiation efficiency at 60 GHz, and at the same distance, this

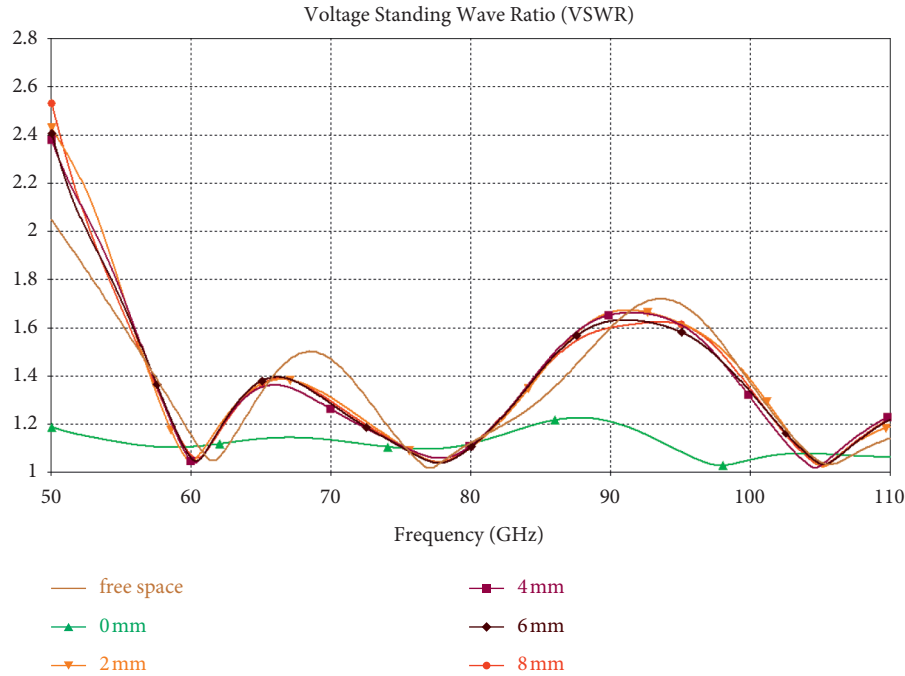


FIGURE 13: VSWR at various distances from the human body and in free space.

TABLE 6: Gain and efficiency comparison.

Distances		Free space	0 mm	2 mm	4 mm	6 mm	8 mm
Frequency (GHz)							
Radiation efficiency (%)	60	70.65	4.966	56	62.12	65.91	68.6
	80	63.96	4.94	47.49	53.55	58.52	60.44
	100	57.31	4.404	41.28	49.61	52.75	53.8
Total efficiency (%)	60	70.28	4.953	55.97	62.08	65.85	68.51
	80	63.74	4.924	47.37	53.25	58.38	60.28
	100	55.89	4.401	40.21	48.71	51.67	52.63
Gain (dB)	60	4.669	-6.368	6.071	5.394	5.463	5.407
	80	4.125	-4.665	5.413	4.688	4.253	4.018
	100	5.779	-6.524	6.853	7.007	6.852	6.511

antenna shows nearly 6.85 dB gain at 100 GHz. Even when it is quite close to the body, this antenna produces interesting results. As the distance between the body and the antenna extends, the performance improves.

## 6. Conclusion

In this paper, a novel and very tiny design of a multiple band super wide band millimeter wave antenna is presented. Simulations were done with the newly designed antenna in both free space and the human body with the help of modeling human body structures. The results were analyzed and compared. Simulations were done at three different frequencies of the mmWave spectrum (EHF range) and found promising results. The notable part was that the design is less vulnerable to the presence of the lossy human body, which makes it suitable and a potential candidate for body-centric communications. With a volume of  $8 \text{ mm} \times 5.12 \text{ mm} \times 1.57 \text{ mm}$ , the antenna is very small. Due to its very tiny size and printed structure, it can be equipped

with other lightweight, portable devices or can be placed on a human body. Moreover, multiple band operability made the antenna unique and widened its possibilities and area of application. The proposed antenna has a super wideband impedance bandwidth, which will be an excellent candidate for high data rate applications. According to the knowledge of the authors of this paper, this antenna achieved the most wideband bandwidth as it works over a large frequency spectrum with a return loss of less than  $-10 \text{ dB}$ . This antenna is the smallest mmWave antenna so far found in the open literature. This proposed antenna design and study in this paper is a novel work in mmWave antennas.

Further distance-based study clarifies the antenna's in-depth nature, which helped determine where and how it could serve in body-centric communications. We know the body area network (BAN) or BCN consists of three types of communication: in-body, off-body, and on-body communications [7]. When the sensor is implanted in the body and made to communicate with the external module, it is known as in-body communication. When the communication

device is placed on the human body (contact or contactless close proximity, e.g., 2 mm; can be of a thread or fabric thickness) and set to communicate with similar on-body sensors, it is known as on-body communication. If one of them is set outside the body to transfer and receive data, it is known as “off-body communication.” From the final distance-based analysis, it can be said that the performance of this proposed antenna is mostly suitable for on-body communications in body-centric networks (BCNs). In the future, this antenna could be designed on a textile substrate. In addition, the bending performance of the antenna can be investigated.

## Data Availability

The data used to support the findings of this study are freely available at <http://niremf.ifac.cnr.it/tissprop/>.

## Conflicts of Interest

The authors declare that they have no conflicts of interest regarding the present study.

## Acknowledgments

The authors are thankful for the support from Taif University Researchers Supporting Project (TURSP-2020/98), Taif University, Taif, Saudi Arabia.

## References

- [1] N. Guo, R. C. Qiu, S. S. Mo, and K. Takahashi, “60-GHz millimeter-wave radio: principle, technology, and new results,” *EURASIP Journal on Wireless Communications and Networking*, vol. 2007, no. 1, p. 190, 2007.
- [2] D. Dawson, *Unlicensed Millimeter Wave Spectrum*, CircleID, [Online]. Available: [https://www.circleid.com/posts/20190918\\_unlicensed\\_millimeter\\_wave\\_spectrum/](https://www.circleid.com/posts/20190918_unlicensed_millimeter_wave_spectrum/), 2019.
- [3] *inFCC Report*, <https://fcc.report/IBFS/SAT-LOA-20200526-00055/2378669>, 2021.
- [4] A. A. Thabit, M. S. Mahmoud, A. Alkhayat, and Q. H. Abbasi, “Energy harvesting internet of things health-based paradigm: towards outage probability reduction through inter-wireless body area network cooperation,” *International Journal of Distributed Sensor Networks*, vol. 15, no. 10, pp. 1–12, 2019.
- [5] P. S. Hall and Y. Hao, “Antennas and propagation for body centric communications,” in *Proceedings of the First European Conference On Antennas and Propagation*, pp. 1–7, Nice, France, 2006.
- [6] T.-W. Koo, Y.-J. Hong, G.-k. Park, K. Shin, and J.-G. Yook, “Extremely low-profile antenna for attachable bio-sensors,” *IEEE Transactions on Antennas and Propagation*, vol. 63, no. 4, pp. 1537–1545, 2015.
- [7] P. S. Hall and Y. Hao, *Antennas and Propagation for Body-Centric Wireless Communications*, Artech House, Norwood, MA, USA, 2006.
- [8] A. Christ, A. Kligenbock, T. Samaras, C. Goiceanu, and N. Kuster, “The dependence of electromagnetic far-field absorption on body tissue composition in the frequency range from 300 MHz to 6 GHz,” *IEEE Transactions on Microwave Theory and Techniques*, vol. 54, no. 5, pp. 2188–2195, 2006.
- [9] C. Calvez, R. Pilard, C. Person et al., “Millimeter-wave antenna designs for 60 GHz applications: SoC and SiP approaches,” *International Journal of Microwave and Wireless Technologies*, vol. 3, no. 2, pp. 179–188, 2011.
- [10] J. Adamu, “Millimeter wave patch antenna design antenna for future 5G applications,” *International Journal of Engineering and Technical Research*, vol. 6, pp. 289–291, 2017.
- [11] J. Choi, J. Choi, and W. Hwang, “Miniature millimeter-wave 5G antenna fabricated using anodized aluminum oxide for mobile devices,” *ACS Omega*, vol. 5, no. 40, 2020.
- [12] C.-N. Hu, D.-C. Chang, C.-H. Yu, T.-W. Hsaio, and D.-P. Lin, “Millimeter-wave microstrip antenna array design and an adaptive algorithm for future 5G wireless communication systems,” *International Journal of Antennas and Propagation*, vol. 2016, Article ID 7202143, 10 pages, 2016.
- [13] H. Shawkey and D. Elsheakh, “Multiband dual-meander line antenna for body-centric networks’ biomedical applications by using UMC 180 nm,” *Electronics*, vol. 9, p. 1350, 2020.
- [14] N. Chahat, M. Zhadobov, S. A. Muhammad, L. Le Coq, and R. Sauleau, “60-GHz textile antenna array for body-centric communications,” *IEEE Transactions on Antennas and Propagation*, vol. 61, no. 4, pp. 1816–1824, 2013.
- [15] M. Monirujjaman Khan, K. Islam, M. N. A. Shovon, M. Masud, M. Baz, and M. A. AlZain, “Various textiles-based comparative analysis of a millimeter wave miniaturized novel antenna design for body-centric communications,” *International Journal of Antennas and Propagation*, vol. 2021, Article ID 2360440, 14 pages, 2021.
- [16] N. Chahat, M. Zhadobov, L. Le Coq, and R. Sauleau, “Wearable endfire textile antenna for on-body communications at 60 GHz,” *IEEE Antennas and Wireless Propagation Letters*, vol. 11, pp. 799–802, 2012.
- [17] M. Ur-Rehman, N. A. Malik, X. Yang, Q. H. Abbasi, Z. Zhang, and N. Zhao, “A low profile Antenna for millimeter-wave body-centric applications,” *IEEE Transactions on Antennas and Propagation*, vol. 65, no. 12, pp. 6329–6337, 2017.
- [18] Italian National Research Council, *Dielectric Properties of Body Tissues in the Frequency Range 10 Hz to 100 GHz*, Italian National Research Council, [Online]. Available: <http://niremf.ifac.cnr.it/tissprop/>, Italy.
- [19] M. M. Khan, Q. H. Abbasi, A. Alomainy, C. Parini, and Y. Hao, “Dual band and dual mode antenna for power efficient body-centric wireless communications,” in *Proceedings of the IEEE International Symposium On Antennas and Propagation (APSURSI)*, pp. 396–399, Spokane, WA, USA, July 2011.
- [20] S. H. Choi, J. Kim, J. K. Park, S. K. Kim, and J. Y. Park, “A new ultra-wideband antenna for UWB applications,” *Microwave and Optical Technology Letters*, vol. 40, no. 5, pp. 399–401, 2004.
- [21] B. Biscontini, S. Hamid, F. Demmel, and P. Russer, “A novel antenna for ultra wide band (UWB) intelligent antenna systems,” in *Proceedings of the IEEE MTT-S International Microwave Symposium Digestion*, pp. 2023–2026, San Francisco, CA, USA, June 2006.
- [22] A. Y. I. Ashyap, Z. Zainal Abidin, S. H. Dahlan et al., “Inverted E-shaped wearable textile antenna for medical applications,” *IEEE Access*, vol. 6, pp. 35214–35222, 2018.

## Research Article

# A Wideband Reflector-Backed Antenna for Applications in GPR

A. Raza <sup>1</sup>, W. Lin <sup>2</sup>, M. K. Ishfaq <sup>1</sup>, M. Inam <sup>3</sup>, F. Masud <sup>4</sup>, and M. H. Dahri <sup>5</sup>

<sup>1</sup>Department of Electrical Engineering, Government College University Faisalabad, Faisalabad, Pakistan

<sup>2</sup>School of Mathematics and Physics, University of South China, Hengyang 421001, China

<sup>3</sup>Faculty of Electrical and Electronic Engineering Technology, Universiti Teknikal Malaysia Melaka (UTeM), Melaka 76100, Malaysia

<sup>4</sup>Department of Statistics and Computer Science, University of Veterinary & Animal Sciences, Lahore, Pakistan

<sup>5</sup>Dawood University of Engineering and Technology, Karachi, Pakistan

Correspondence should be addressed to M. Inam; [muhammad\\_inamabbasi@yahoo.com](mailto:muhammad_inamabbasi@yahoo.com)

Received 10 September 2021; Revised 20 October 2021; Accepted 26 October 2021; Published 8 November 2021

Academic Editor: Mohammad Alibakhshikenari

Copyright © 2021 A. Raza et al. This is an open access article distributed under the Creative Commons Attribution License, which permits unrestricted use, distribution, and reproduction in any medium, provided the original work is properly cited.

A resistively loaded wideband slotted patch antenna with optimized performance on lower frequencies is proposed for ground-penetrating radar (GPR) applications. The proposed design is backed by an optimized reflector composed of a periodic array of square loop elements, which enhances the antenna's gain and directivity. The antenna shows good radiation characteristics and ease of integration with the GPR systems. The proposed structure features a compact size and wide bandwidth covering from 0.6 to 4.6 GHz. The peak gain of 7 dBi is achieved. The fabricated prototype of the antenna along with an integrated optimized reflective surface has overall dimensions of  $18 \times 22 \times 5 \text{ cm}^3$ . The measured results validate the antenna's performance in both free space and sandy medium, which enlighten its use for GPR applications.

## 1. Introduction

Ground-penetrating radar (GPR) is an important technology developed for short-range radar applications. Electromagnetic waves are used for the detection of metallic and nonmetallic buried objects. Nowadays, GPR use not only is limited to subsurface and through wall utility detection but also has a wide range of applications in the commercial sector including nondestructive testing, explorations in mining, disaster relief work, and discovery of hidden tunnels. GPR has gained popularity due to its effectiveness in the civil and geological structural investigation. Unlike conventional radar, GPR signals travel in the lossy and inhomogeneous mediums varying in properties. With investigation of buried static targets at different depths, antennas employed in GPR should have ultrawideband characteristics. High frequencies are used for the detection of small targets in shallow depths; whereas low frequencies are used for the detection of large and deeper targets. Therefore, antennas used in GPR have an operating

frequency ranging from a few MHz to GHz covering a decade bandwidth [1].

Two common types of GPR systems are impulse GPR and continuous wave GPR. Most commercially available GPR systems incorporate impulse techniques. In these systems, a time-domain pulse is transmitted by the antenna and a reflected wave is received; short-duration pulse of nanosecond duration is used to achieve a broad bandwidth. Therefore, the antenna performs as an essential part of impulse GPR system performance, whereas continuous-wave GPR systems operate in the frequency domain and transmit continuously. A significant challenge in a continuous wave, both swept frequency and stepped frequency technique, is the synchronization of time in the entire sweep [2, 3].

For optimization of GPR antenna, several aspects including physical dimension, weight, impedance bandwidth, and footprint are considered. In recent years, many GPR antennas are designed for a diverse range of applications including civilian and military, as well as security services. A

transverse electromagnetic (TEM) horn antenna for air-coupled impulse GPR applications is presented in [4]; it operates in the broad frequency range between 0.6 and 6 GHz. A dipole antenna, in [5], is presented for structural investigation, operating in the frequency range from 0.45 to 1.1 GHz. Although 3D antennas such as horn [4], dipole [5], cone [6], and spiral [7] provide satisfactory GPR performances, their 3D structure led to an increase in size and weight of the antenna.

To address this issue, various planar antennas were proposed. The tapered slot antennas can be a good competitor because of their end-fire radiation, moderate gain, small dimensions, low-cost components, and easy fabrication. A few slotted designs were also presented like a CPW-fed tapered slot antenna [8], operating in 0.64 to 6 GHz, and a compact slot antenna [9], operating in 1.4 to 3.5 GHz. These slot-loaded designs are fed by the coplanar waveguide and are compact but have the disadvantage of low gain and low resolution, as back radiation of the antenna is of no use in the GPR system. Therefore, absorbing materials are used to avoid interference with the communication spectrum [10]. This back radiation can be used to illuminate the ground. Thus, some solutions are suggested for constructively enhancing the gain of planar antennas [11–16]. In the antenna casing of GPR, the use of a reflector, cavity, electromagnetic band-gap (EBG) structure, loop directors, and choke rings [17–21] is proposed for high gain GPR applications.

In this study, a compact and wideband reflector backed slotted patch antenna, suitable for applications in GPR, is presented. The proposed design provides a wide bandwidth from 0.6 GHz to 4.6 GHz. Furthermore, a reflective surface is designed to enhance the radiation performance of the antenna, especially at lower frequencies. The proposed antenna is compact and is constructed using low cost and lightweight materials, as well as its simple structure provides ease in fabrication. The presented antenna is tested under soil conditions to ensure its application for GPR. Also, the proposed design can be used simultaneously for 2G, 3G, 4G, and 5G applications as it covers 900/1800/1900/2100/2600/3500 MHz frequency bands.

## 2. Antenna Description

The geometrical structure of the planar slotted patch antenna (SPA) is shown in Figure 1. The antenna is fabricated using low cost and lightweight materials. The radiating structure is printed over a 1.6 mm thick FR-4 substrate with relative permittivity of 4.4. To have better control over characteristics impedance, the SPA antenna is fed by a tapered feed. The patch antenna has numerous advantages, such as being lightweight, low cost, and high gain, as compared to the CPW counterpart [22].

Therefore, the antenna-radiating structure is optimized to minimize aperture reflections and achieve wideband operation while keeping the antenna size small. Generally speaking, the mentioned antenna is geometrically designed using four elliptical patches. The big elliptical patches, having radii ER1 and ER2, are parallel to each other and

orthogonal to two small patches of radii ER3 and ER4. This configuration created a uniformly tapered bowtie-shaped radiating slot with a separation of 2 mm in the middle and 20 mm on the sides. The uniformly tapered bowtie-shaped radiating slot changes the direction and effective length of surface current on the radiator [23, 24]. A resistor is placed at the center of the slot for lower band operation. This design is termed as a resistive loaded slotted patch antenna (RLSPA). The planar antenna covers a dimension of  $18 \times 22 \text{ cm}^2$ . The antenna is further fine tuned using an inbuilt optimizer of antenna simulation software. The detailed dimensions of the antenna are described as below (in millimeters):  $L = 220$ ,  $W = 180$ ,  $ER1 = 80$ ,  $ER2 = 25$ ,  $ER3 = 35$ ,  $ER4 = 12$ ,  $LF = 111$ ,  $WF = 3.6$ ,  $L1 = 3.8$ ,  $L2 = 19.5$ ,  $g = 0.6$ ,  $Lg = 110$ ,  $L3 = 20.6$ ,  $L4 = 20.2$ ,  $SH = 60$ , and  $D = 50$ . The geometrical structure of the proposed reflector-backed antenna along with the fabrication is shown in Figure 2. The reflector comprises a  $4 \times 4$  slot array, where the size of each slot is  $2 \times 3 \text{ cm}^2$ .

## 3. Working Principle

A typical antenna in an impulse radar system should operate in a lower range of frequencies with compact dimensions. Therefore, the equivalent circuit of the reflector-backed antenna is investigated, as shown in Figure 3. The structure can be divided into three parts: (1) a square inductive metallic ring, (2) capacitive slot, and (3) ground plane of RLSPA act as a metallic layer [25].

The ground plane is modelled as inductance  $L_h$  and the layer between reflector and ground plane has capacitance coupling, which is represented as  $C_h$  [24, 25]. By using transmission line theory, the equivalent circuit input impedance can be expressed as a combination of inductive and capacitive components of the reflective surface as

$$Z_L = \frac{1}{j\omega C_h}, \quad (1)$$

$$Z_H = \frac{1}{(1/j\omega L_1) + (1/j\omega L_h)}.$$

The antenna's performance can be determined by many parameters including antenna size, radiation characteristics, bandwidth, and stable gain. Aperture reflections are a considerable cause of the reduction in radiation efficiency of UWB antennas for GPR [17].

GPR antennas have to satisfy a broad frequency band for better imaging resolution of the GPR system. Consequently, the removal of discontinuous points in radiation structure is considered an important optimization factor while designing. Also, slot loading, resistive loading, tapered feed, and curved ground have been utilized, and their effect to achieve specific antenna performance for GPR is recorded, respectively, and the results are described.

*3.1. Effect of the Loaded Resistor.* The resistive loading is used in many GPR antenna designs [7, 8], which is an effective method for bandwidth enhancement on lower frequencies

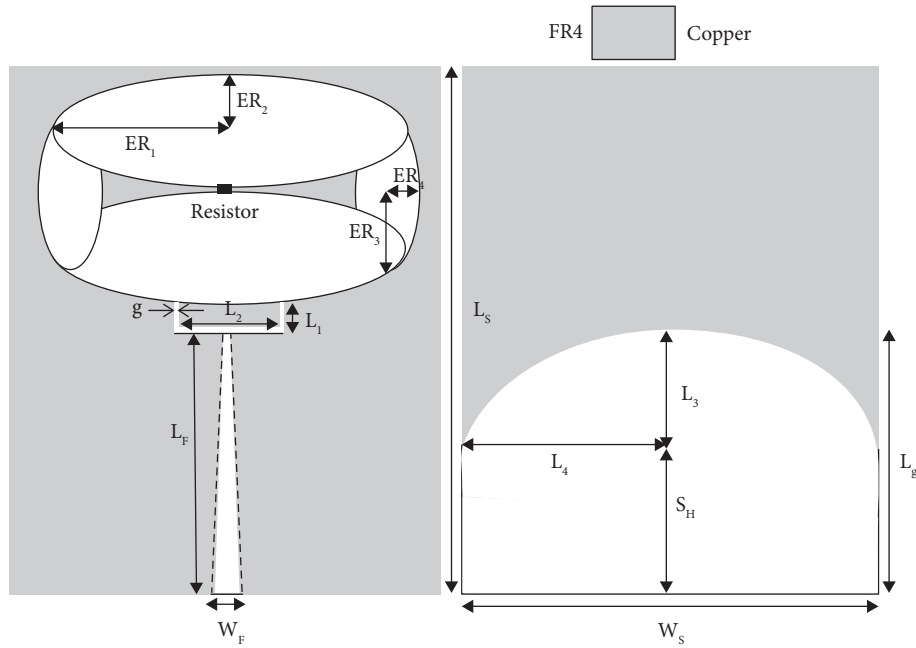


FIGURE 1: Geometrical construction of the planar SPA: (a) top radiator and (b) bottom view (ground plane).

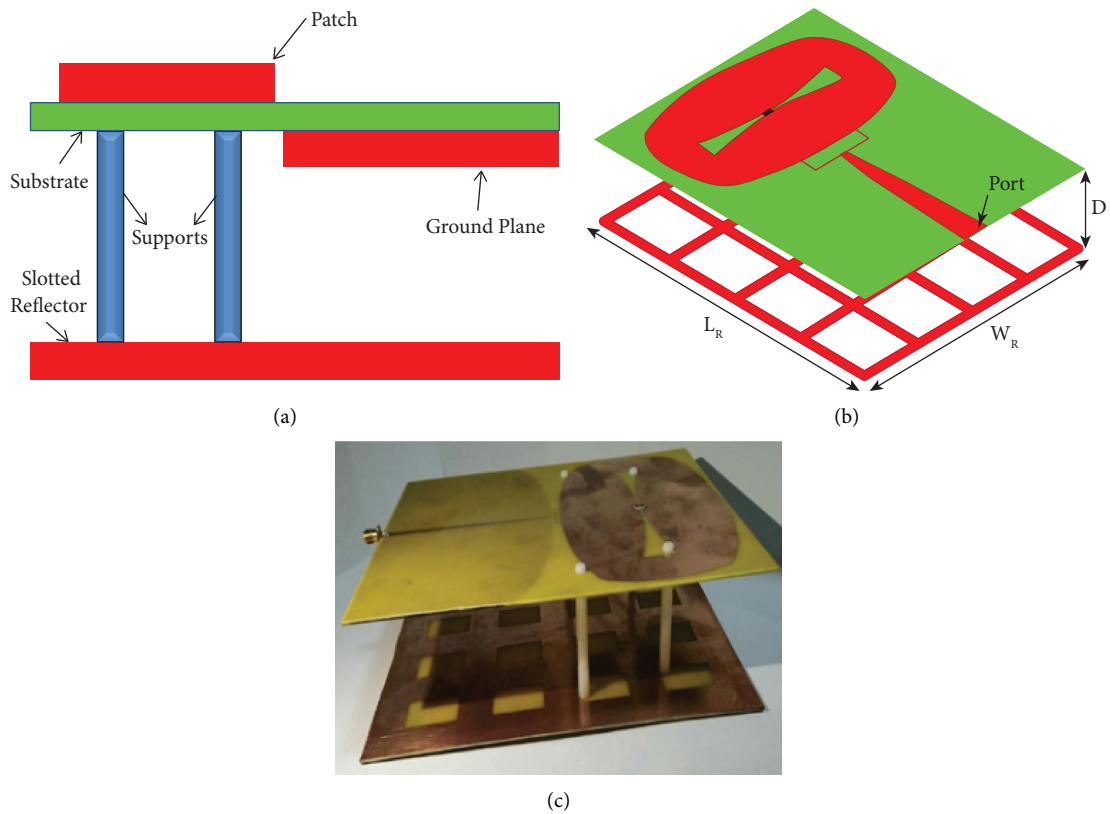


FIGURE 2: Geometry of the reflector-backed antenna: (a) side view (b) 3D view; (b) reflector-backed fabricated antenna.

while keeping the size of the antenna small. The optimal resistance value of  $50 \Omega$  is used for better impedance matching. Figure 4 shows the voltage standing wave ratio (VSWR) of SPA and resistively loaded slotted patch antenna

(RLSPA). After the optimization process, the surface current distribution at frequency 1 GHz of the SPA and RLSPA is shown in Figure 5. However, the use of resistors may introduce extra losses in the antenna. The antenna structure is

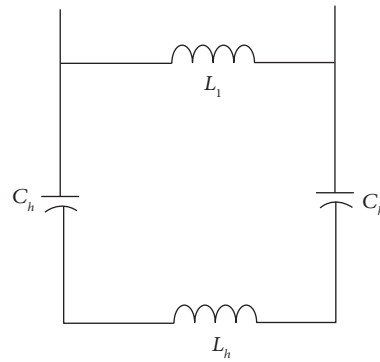


FIGURE 3: Equivalent circuit of the proposed reflector-backed antenna.

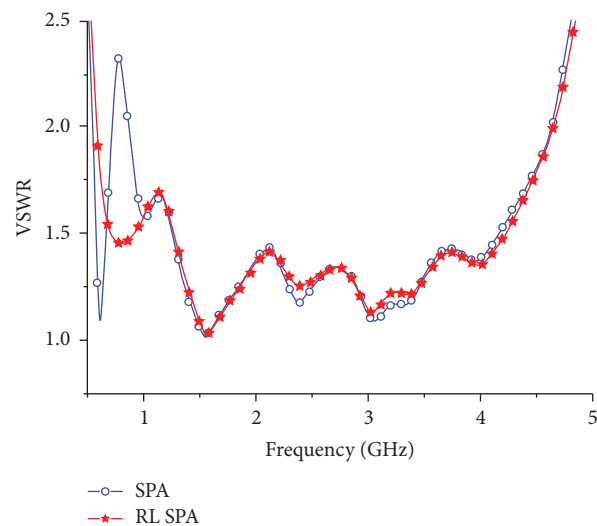


FIGURE 4: The VSWR of SPA and RLSPA.

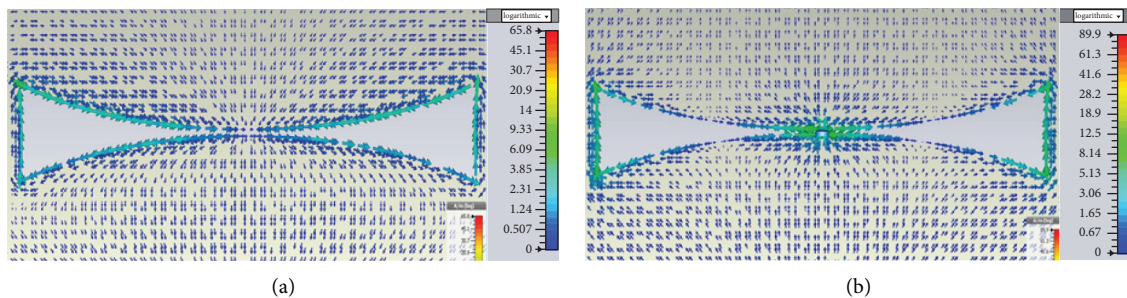


FIGURE 5: Construction of the antenna: (a) top radiator and (b) bottom view (ground plane).

optimized by the removal of discontinuous points in the radiating structure to reduce the aperture reflections.

The loaded resistance absorbs a part of the residual current. The distributed current mainly concentrates on the tapered feed and resistively loaded slot. Therefore, a slot is introduced into the radiating structure, which produces two current loops. The resistive loading introduced in the middle of the slot enhances current by the creation of additional two

small current loops, as shown in Figure 5(b). The resistive loading increases the flow of current in the radiation structure.

*3.2. Effect of the Tapered Ground.* Many performance parameters are considered in an antenna design to attain a specific objective, such as the size of the radiating structure

and center frequency. Some adjustments to these parameters were made, and effects on performance are recorded, respectively. Figure 5 shows the effect of ground plane optimization for the bandwidth enhancement of the proposed antenna. The top corners of the ground plane are rounded to reduce aperture reflections and better impedance matching.

The curved ground plane along with the tapered feeding structure is found useful in an enhancement of the lower frequency band. Therefore, in the proposed antenna optimization, the ground plane is used to enhance bandwidth. Figure 6 shows the antenna impedance plot, while Figure 7 shows the time-domain characteristics of the antenna. When an amplitude-modulated Gaussian pulse is applied, the received output signal has a 0.5 ns time duration with some minor reflections.

#### 4. Results and Discussion

The measured reflection coefficient  $S_{11}$  of the fabricated reflector-backed resistively loaded slotted patch antenna (RB-RLSPA) is displayed in Figure 8. The photographs of the antenna measurement setup are shown in Figure 9.

The proposed antenna operates ( $S_{11}$  less than  $-10$  dB) in the frequency band from 0.6 to 4.5 GHz. Generally speaking, a compact antenna structure can also reduce the antenna's radar cross section to a certain extent, and the reflected radiation energy can illuminate the ground surface. The constructive coupling between the antenna and the reflector leads to a significant increase in the gain of the antenna [26]. The enhancement of gain over the entire frequency band is achieved with a peak gain of 7 dBi; the optimal distance between RLSPA and slotted reflector is 5 cm, as displayed in Figure 10.

Despite the reflector, the ultrawideband operation of the proposed antenna is maintained. Figure 11 shows the simulated and measured radiation pattern of the proposed reflector-backed antenna design at 1 GHz, 2 GHz, 3 GHz, and 4 GHz. As it can be observed, the radiation plots are directional at lower frequencies such as 1 and 2 GHz. The performance of the proposed antenna is compared with preexisting antennas, and analysis is presented in Table 1.

**4.1. Experiment.** The performance of the proposed antenna has been evaluated above sandy soil, as shown in Figure 12 [17]. The proposed antenna is placed on the sand surface, whereas a loop antenna as an electromagnetic field sensor was placed under the sandy surface for measurement of reflection coefficient  $S_{21}$  [27, 28]. The result obtained from the electromagnetic field sensor is calculated using Agilent E5071C vector network analyzer and displayed in Figure 13 [29]. Furthermore, it can be noticed that the antenna shows good parasitic coupling performance at a whole frequency band, except for some late time ringing on higher frequencies. However, the variation is too small to be significant for electromagnetic wave behavior, as the coupling levels at all frequency bands stay below  $-35$  dB [30, 31].

Figure 14 shows the block diagram of the sandbox test setup for the antenna's use as GPR under field conditions

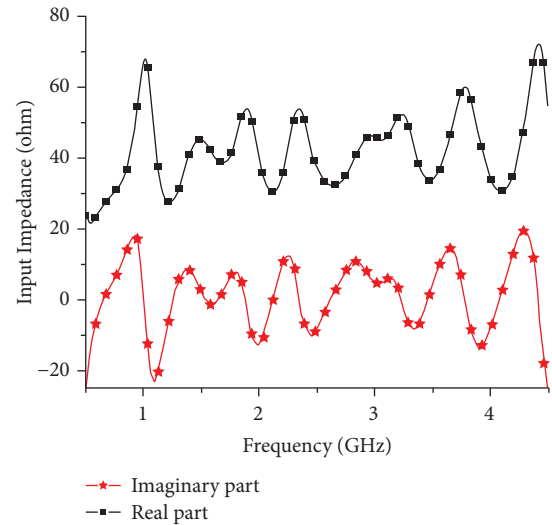


FIGURE 6: Impedance plot of the antenna.

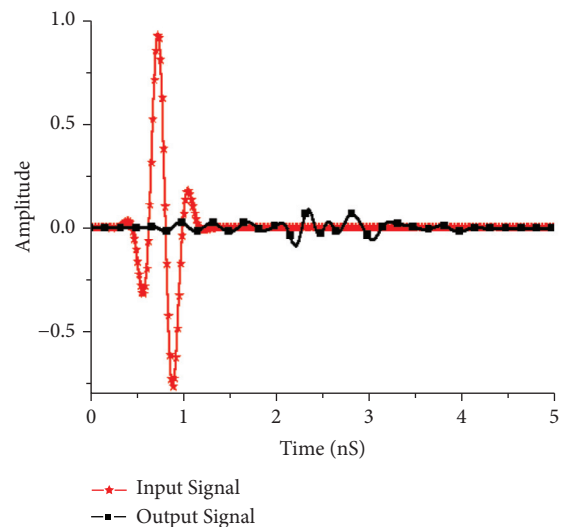


FIGURE 7: Time-domain performance of the proposed antenna.

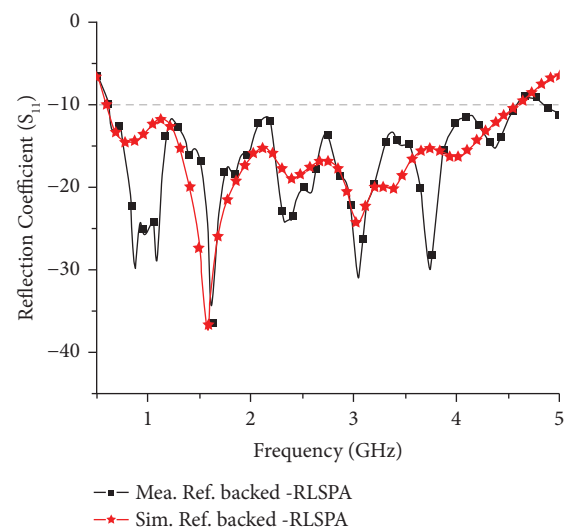


FIGURE 8: Simulated and measured  $S_{11}$  of reflector-backed antenna.

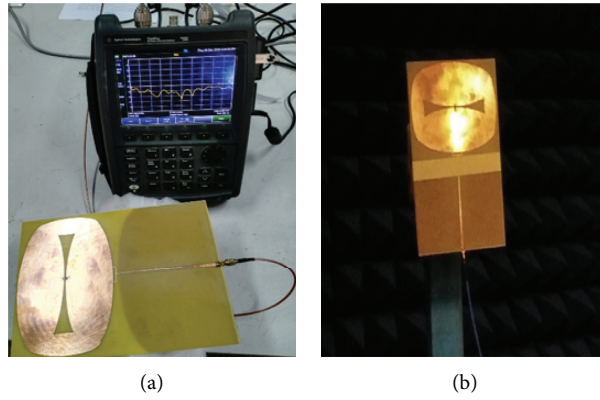


FIGURE 9: Photographs of the antenna measurement: (a) vector network analyzer (VNA) and (b) anechoic chamber.

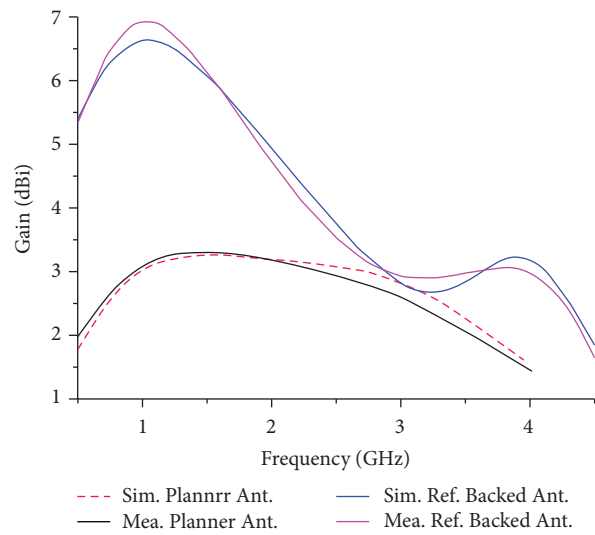


FIGURE 10: Simulated and measured gain of the proposed antenna at the different gaps between the reflector and the antenna.

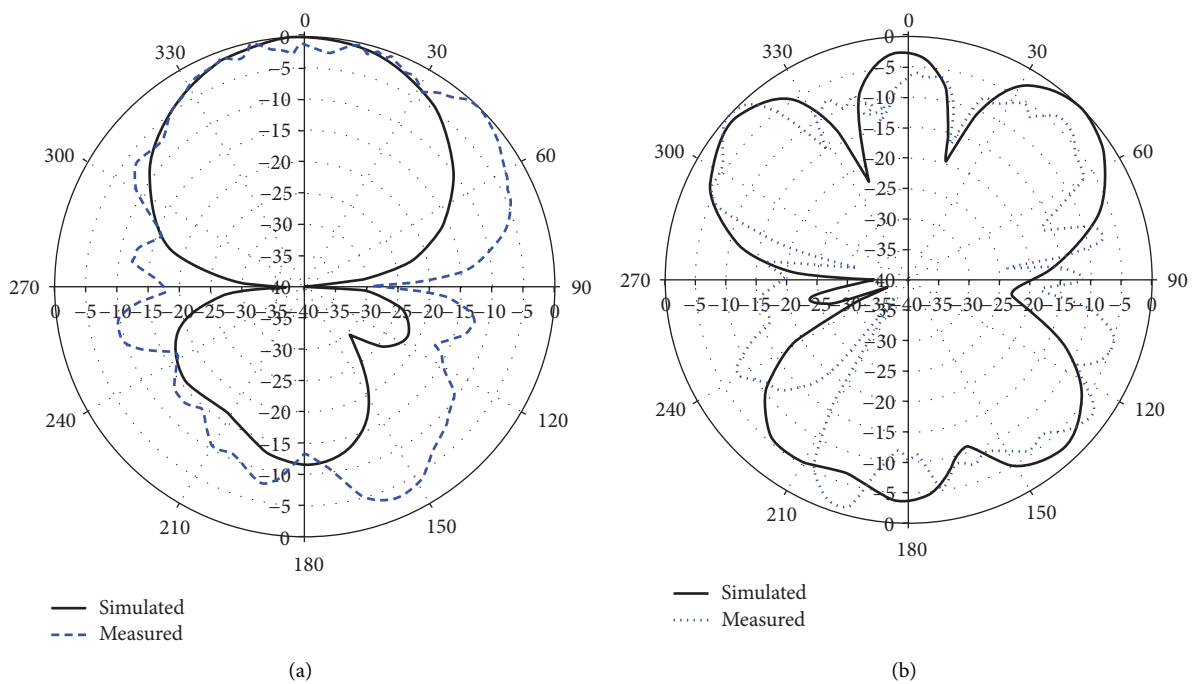


FIGURE 11: Continued.

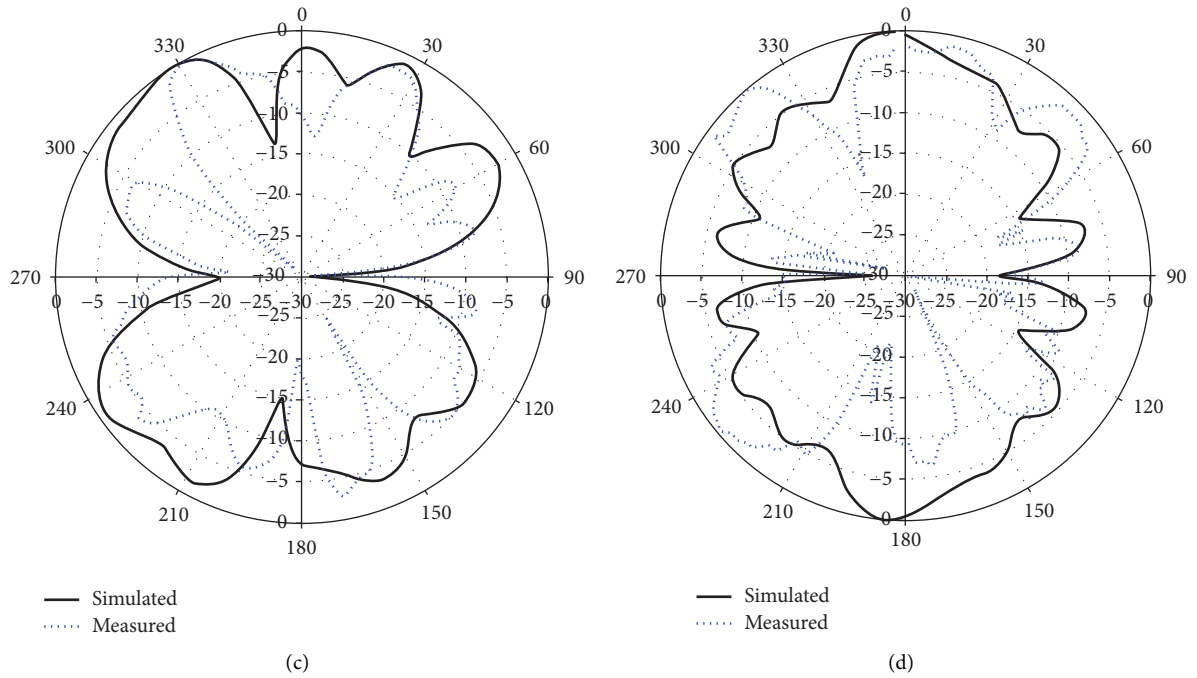


FIGURE 11: Simulated and measured E-plane radiation pattern of reflector-backed RLSPA: (a) 1 GHz; (b) 2 GHz; (c) 3 GHz; (d) 4 GHz.

TABLE 1: Proposed antenna’s comparative analysis with already existing antennas.

Reference	Shape	Antenna dimensions (cm <sup>3</sup> )	Frequency (GHz)	Peak gain (dBi)	Complexity/ease of manufacturing	Reflector type
[4]	Horn	25 × 18 × 18	0.6 to 6	9.91	Complex/costly	No
[6]	Cone	15.8 × 15.8 × 17.4	0.5 to 3	4.4	Complex/costly	No
[7]	Sinuous	10 × 10 × 9	2 to 6	7	Complex	No
[9]	Slot	10.7 × 7 × 5	1.4 to 3.5	6	Simple	Planner
[11]	Bowtie	27 × 18 × 11	0.5 to 3	12	Complex/costly	Cavity
[12]	Bow tie	20 × 15 × 4	0.98 to 4.5	10.3	Simple	Cavity
[26]	Patch	20.5 × 20.5 × 12	0.433	6	Simple	Reactive impedance surface(RIS)
<b>Proposed design</b>	<b>Tapered feed</b>	<b>18 × 22 × 5</b>	<b>0.6 to 4.6</b>	<b>7</b>	<b>Simple</b>	<b>Planner</b>

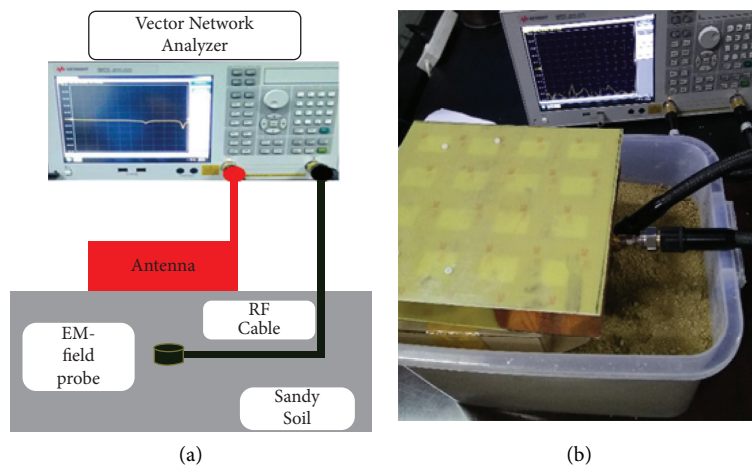


FIGURE 12: Sandbox experiment: (a) diagram of the experiment; (b) picture of the experiment.

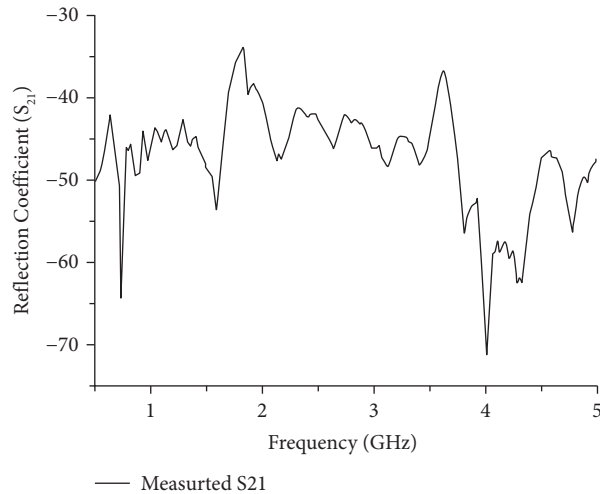


FIGURE 13: Measured  $S_{21}$  returns loss of the proposed antenna.

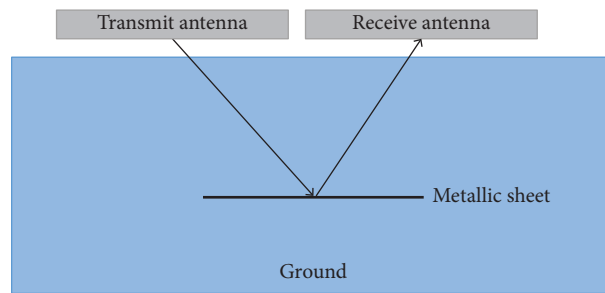


FIGURE 14: The block diagram of GPR test arrangement in the lab.

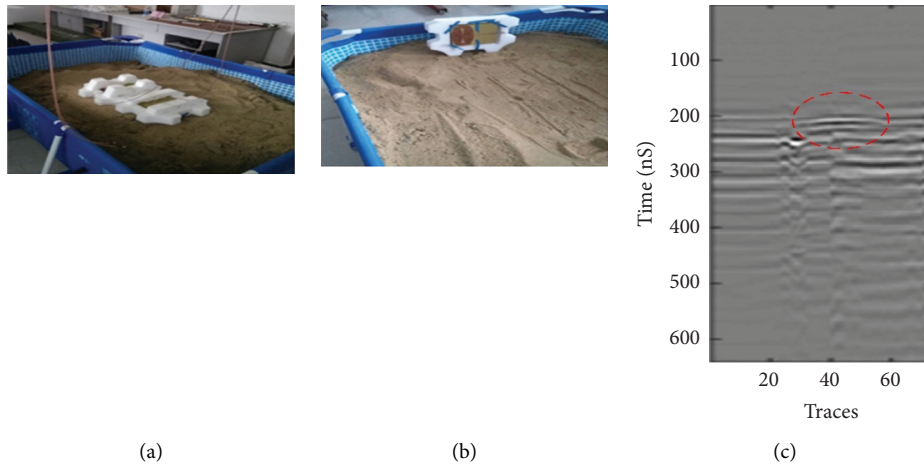


FIGURE 15: The block diagram of GPR test arrangement in the lab.

[10]. While experimentally testing the antenna’s ability to be used as GPR, some factors that can affect the detectability of buried objects include uneven surface, airgap between soil and antenna, and the presence of air bubbles under the target surface. Therefore, the height of the antenna above ground is kept very low so that ground acts as a dielectric part of the antenna system. The experimental setup along with the experimental results from the pulse radar system is shown in Figure 15 [9, 20]. The hyperbolic reflection curve is observed

and highlighted using a red dashed circle, which indicates the detectability of subsurface targets using the proposed antenna in pair configuration [32].

### 5. Conclusion

In this paper, a resistive-loaded wideband slotted patch antenna with optimized performance on low frequencies is proposed for GPR applications. The proposed design

provides an ultrawide bandwidth ranging from 0.6 GHz to 4.6 GHz with compact dimensions. The fabricated prototype of the antenna along with an integrated reflective surface has overall dimensions of  $18 \times 22 \times 5 \text{ cm}^3$ . The antenna exhibits good radiation characteristics. The presented antenna is suitable for GPR due to its simple structure, ease of fabrication, and low cost. The antenna is experimentally evaluated under soil conditions, as well as its ability to detect buried objects is tested. The experimental results validate the proposed antenna's ability to be used in GPR.

## Data Availability

The data used to support the findings of the study can be obtained from the corresponding author upon request.

## Conflicts of Interest

The authors declare that there are no conflicts of interest regarding the publication of this paper.

## Acknowledgments

This work was supported in part by the National Natural Science Foundation of China (Grant no. 11847307) and China Scholarship Council. The authors would like to thank Mr Jiyu Guo from the School of Resources and Environment, University of Electronic Science and Technology, Chengdu, China, for providing GPR measurement set up.

## References

- [1] M. Harry, *Ground Penetrating Radar: Theory and Applications*, Elsevier Science, England, UK, 2009.
- [2] Q. Wang, B. Ai, K. Guan, D. W. Matolak, R. He, and X. Zhou, "Ray-Based statistical propagation modeling for indoor corridor scenarios at 15 GHz," *International Journal of Antennas and Propagation*, vol. 2016, Article ID 2523913, 12 pages, 2016.
- [3] W. Wiesbeck, G. Adamiuk, and C. Sturm, "Basic properties and design principles of UWB antennas," *Proceedings of the IEEE*, vol. 97, no. 2, pp. 372–385, 2009.
- [4] A. Ahmed, Y. Zhang, D. Burns, D. Huston, and T. Xia, "Design of UWB antenna for air-coupled impulse ground-penetrating radar," *IEEE Geoscience and Remote Sensing Letters*, vol. 13, no. 1, pp. 92–96, 2016.
- [5] H. Qin and X. Xie, "Design and test of an improved dipole antenna for detecting enclosure structure defects by cross-hole GPR," *IEEE Journal of Selected Topics in Applied Earth Observations and Remote Sensing*, vol. 9, no. 1, pp. 108–114, 2016.
- [6] J. Ali, N. Abdullah, and M. Yusof, "Ultra-wideband antenna design for GPR applications: a review," *International Journal of Advanced Computer Science and Applications*, vol. 8, no. 7, pp. 392–400, 2017.
- [7] D. A. Crocker and W. R. Scott, "On the design of sinuous antennas for UWB radar applications," *IEEE Antennas and Wireless Propagation Letters*, vol. 18, no. 7, pp. 1347–1351, 2019.
- [8] J. Shao, G. Fang, Y. Ji, K. Tan, and H. Yin, "A novel compact tapered-slot antenna for GPR applications," *IEEE Antennas and Wireless Propagation Letters*, vol. 12, no. 1, pp. 972–975, 2013.
- [9] M. Li, R. Birken, N. X. Sun, and M. L. Wang, "Compact slot antenna with low dispersion for ground penetrating radar application," *IEEE Antennas and Wireless Propagation Letters*, vol. 15, pp. 638–641, 2016.
- [10] J. Jinjin Shao, G. Guangyou Fang, J. Jingjing Fan, Y. YiCai Ji, and H. Hejun Yin, "TEM horn antenna loaded with absorbing material for GPR applications," *IEEE Antennas and Wireless Propagation Letters*, vol. 13, pp. 523–527, 2014.
- [11] M. Alibakhshikenari, B. S. Virdee, P. Shukla et al., "Impedance bandwidth improvement of a planar antenna based on metamaterial-inspired T-matching network," *IEEE Access*, vol. 9, pp. 67916–67927, 2021.
- [12] M. M. Shirkolaei and M. Jafari, "A new class of wideband microstrip falcate patch antennas with reconfigurable capability at circular-polarization," *Microwave and Optical Technology Letters*, vol. 62, no. 12, pp. 1–6, 2020.
- [13] M. Alibakhshikenari, B. S. Virdee, A. A. Althuwayb et al., "Bandwidth and gain enhancement of composite right left handed metamaterial transmission line planar antenna employing a non foster impedance matching circuit board," *Scientific Reports*, vol. 11, no. 1, Article ID 7472, 2021.
- [14] A. Maleki, H. D. Oskouei, and M. M. Shirkolaei, "Miniaturized microstrip patch antenna with high inter-port isolation for full duplex communication system," *International Journal of RF and Microwave Computer-Aided Engineering*, vol. 31, 2021.
- [15] F. Moayyed, H. R. Dalili Oskouei, and M. Mohammadi Shirkolaei, "High gain and wideband multi-stack multilayer anisotropic dielectric antenna," *Progress In Electromagnetics Research Letters*, vol. 99, pp. 103–109, 2021.
- [16] M. Masoumi, H. R. Dalili Oskouei, M. Mohammadi Shirkolaei, and A. R. Mirtaheri, "Substrate integrated waveguide leaky wave antenna with circular polarization and improvement of the scan angle," *Microwave and Optical Technology Letters*, pp. 1–5, 2021.
- [17] M. Serhir and D. Lesselier, "Wideband reflector-backed folded bowtie antenna for ground penetrating radar," *IEEE Transactions on Antennas and Propagation*, vol. 66, no. 3, pp. 1056–1063, 2018.
- [18] M. Joula, V. Rafiei, and S. Karamzadeh, "High gain UWB bow-tie antenna design for ground penetrating radar application," *Microwave and Optical Technology Letters*, vol. 60, pp. 2425–2429, 2018.
- [19] I. T. McMichael, E. C. Nallon, V. P. Schnee, W. R. Scott, and M. S. Mirotznik, "EBG antenna for GPR colocated with a metal detector for landmine detection," *IEEE Geoscience and Remote Sensing Letters*, vol. 10, no. 6, pp. 1329–1333, 2013.
- [20] K. K. Ajith and A. Bhattacharya, "A novel compact super-wideband bowtie antenna for 420 MHz to 5.5 GHz operation," *IEEE Transactions on Antennas and Propagation*, vol. 66, no. 8, pp. 3830–3836, 2018.
- [21] D. J. Sawyer, S. Das, N. Diamanti, A. Peter Annan, and A. K. Iyer, "Choke rings for pattern shaping of a GPR dipole antenna," *IEEE Transactions on Antennas and Propagation*, vol. 66, no. 12, pp. 6781–6790, 2018.
- [22] D. M. Pozar, "Microstrip antennas," *Proceedings of the IEEE*, vol. 80, no. 1, pp. 79–91, 1992.
- [23] M. Ojaroudi, S. Yazdanifard, N. Ojaroudi, and M. Naser-Moghaddasi, "Small square monopole antenna with enhanced bandwidth by using inverted T-shaped slot and conductor-backed plane," *IEEE Transactions on Antennas and Propagation*, vol. 59, no. 2, pp. 670–674, 2011.
- [24] A. Raza, W. Lin, Y. Liu, A. B. Sharif, Y. Chen, and C. Ma, "A magnetic-loop based monopole antenna for GPR

- applications,” *Microwave and Optical Technology Letters*, vol. 61, no. 4, pp. 1052–1057, 2019.
- [25] M. Wang, Z. Yang, J. Wu et al., “Investigation of SAR reduction using flexible antenna with metamaterial structure in wireless body area network,” *IEEE Transactions on Antennas and Propagation*, vol. 66, no. 6, pp. 3076–3086, 2018.
- [26] E. Mohammadi, K. L. Tsakmakidis, F. Sohrabi, A. Tavakoli, and P. Dehkhoda, “Gain enhancement of circular waveguide antennas using near-zero index metamaterials,” *Microwave and Optical Technology Letters*, vol. 61, no. 6, pp. 1617–1621, 2019.
- [27] A. Yarovoy, R. de Jongh, and L. Ligthart, “Ultra-wideband sensor for electromagnetic field measurements in time domain,” *Electronics Letters*, vol. 36, no. 20, pp. 1679–1680, 2000.
- [28] A. G. Yarovoy, T. G. Savelyev, P. J. Aubry, P. E. Lys, and L. P. Ligthart, “UWB array-based sensor for near-field imaging,” *IEEE Transactions on Microwave Theory and Techniques*, vol. 55, no. 6, pp. 1288–1295, 2007.
- [29] H. G. Poley, “GPR antennas design and experimental evaluation,” *Electrical Engineering Mathematics & Computer Science*, Delft University of Technology, Delft, The Netherlands, 2010.
- [30] B. Wu, Y. Ji, and G. Fang, “Analysis of GPR UWB half-ellipse antennas with different heights of backed cavity above ground,” *IEEE Antennas and Wireless Propagation Letters*, vol. 9, pp. 130–133, 2010.
- [31] A. Raza, W. Lin, Y. Chen, Z. Yanting, H. T. Chattha, and A. B. Sharif, “Wideband tapered slot antenna for applications in ground penetrating radar,” *Microwave and Optical Technology Letters*, vol. 62, no. 7, pp. 2562–2568, 2020.
- [32] J. Guo, J. Tong, Q. Zhao, J. Jiao, J. Huo, and C. Ma, “An ultrawide band Antipodal vivaldi antenna for airborne GPR application,” *IEEE Geoscience and Remote Sensing Letters*, vol. 16, no. 10, pp. 1560–1564, 2019.

## Research Article

# A Novel Shape Compact Antenna for Ultrawideband Applications

Saad Hassan Kiani <sup>1</sup>, Xin Cheng Ren <sup>2</sup>, Muhammad Rizwan Anjum <sup>3</sup>,  
Khalid Mahmood <sup>4</sup>, Haider Ali <sup>5</sup>, Naveed Jan <sup>5</sup>, Muhammad Adil Bashir <sup>6</sup>,  
and Muhammad Abbas Khan <sup>7</sup>

<sup>1</sup>Department of Electrical Engineering, City University of Science and Information Technology, Peshawar 25000, Pakistan

<sup>2</sup>School of Physics and Electronic Information, Yanan University, Yanan 761000, China

<sup>3</sup>Department of Electronic Engineering, The Islamia University of Bahawalpur, Bahawalpur 63100, Pakistan

<sup>4</sup>Department of Electrical Engineering, Abasyn University, Peshawar 25000, Pakistan

<sup>5</sup>Department of Electrical and Electronics Engineering Technology, University of Technology Nowshera, Nowshera, Pakistan

<sup>6</sup>Electrical Engineering Department, Bahauddin Zakariya University, Multan, Pakistan

<sup>7</sup>Department of Electrical Engineering, Balochistan University of Information Technology, Engineering and Management Sciences, Quetta, Pakistan

Correspondence should be addressed to Xin Cheng Ren; [xchren@yau.edu.cn](mailto:xchren@yau.edu.cn)

Received 17 September 2021; Accepted 28 September 2021; Published 6 October 2021

Academic Editor: Muhammad Inam Abbasi

Copyright © 2021 Saad Hassan Kiani et al. This is an open access article distributed under the Creative Commons Attribution License, which permits unrestricted use, distribution, and reproduction in any medium, provided the original work is properly cited.

Nowadays, more attention has been given into ultrawideband by dint of its extraordinary features over narrowband communication systems. This study presents a novel compact with tilted square frames shape antenna with partial ground plane. The proposed antenna is printed on commercially available Fr4 substrate with relative thickness of 1.6 mm. The antenna has compact dimensions of  $14 \times 18 \text{ mm}^2$  with bandwidth ranging from 3.3 to 11.5 GHz. The peak gain obtained is 1.4 dBi with omnidirectional radiation characteristics throughout the entire bandwidth. The proposed antenna is fabricated, and the developed prototype measured results, which well agree with simulated results. With the performance parameters obtained and the well agreed measured results, the proposed antenna is well suitable for Wi-Fi, ISM, and UWB applications.

## 1. Introduction

The rapid progress of wireless communication systems has emerged the need of wideband antenna, since they cover majority of applications. After the announcement of ultrawide band (UWB) by federal services commission, several antennas designs have been proposed in order to be deployed on the industrial scale. With low energy consumption, better channel capacity characteristics within the partial range, unmanned vehicles (UAVs), and body area networks (WBANs) [1, 2], the UWB antennas are emerging as most promising candidates for future wireless communication systems [3, 4]. UWB antenna role as compared to the conventional narrowband antenna system is unique and vital. Also, printed antenna technology light weight and low-cost fabrication characteristics as compared to conventional antenna structures provide quick and reliable wireless

communication access. In published literature, several antennas have been reported on UWB technology [5–10].

In literature, several wide and ultrawideband antenna structures have been reported. With a size of  $121 \times 314 \text{ mm}^2$ , a wide band antenna is reported in [5] with bandwidth of approximately 4.6 GHz ranging from 3.4 to 8 GHz. The shape of the antenna comprises a leaf structure with partial ground plane. The proposed antenna is well developed but is difficult to integrate in RF circuits due to its unconventional size. Similarly, in [6], an UWB is proposed with the total size of  $31 \times 23 \text{ mm}^2$ , having bandwidth characteristics ranging from 3 to almost 15 GHz. The antenna is small in size, but the gain variations are quite big. In [7], a monopole antenna is presented with elliptical slot rings. With nearly gain up to 3.5 dBi, the antenna exhibits good flat gain near the entire resonating spectrum, but the size of antenna is quite large up to  $100 \times 100 \text{ mm}^2$ .

A miniaturized UWB antenna with dimensions of  $9.11 \times 10.8$  mm is proposed in [8] with an operating bandwidth of at least 1 GHz around a centre frequency of 4 GHz for implantable applications. The M-shaped antenna resonating with 5600 MHz bandwidth ranging from 3.25 to 8 GHz is covered in [9], with large size of  $100 \times 160$  mm<sup>2</sup>. The V shape antenna with truncated ground plane is presented at [10]; the size of the antenna is  $28 \times 36$  mm, and the gain varies between 0.5 and 2 dB. In [11–14], several antennas have been developed for UWB applications, but they come in large sizes. In [14], the wideband response of 8 GHz has been reported, but the size of the antenna is  $50 \times 50$  mm. Such type of large sizes makes antenna difficult to embed in modern RF devices. A compact antenna with single notch characteristics has been reported in [15] using split ring slots. The size of the antenna is  $23 \times 20$  mm. Similarly, in [16, 17], UWB antennas are proposed with band notch characteristics with approximate size of  $30 \times 34$  mm<sup>2</sup> and  $32 \times 36$  mm<sup>2</sup>. A multilayered compact 3D antenna in [18] exhibits wideband impedance characteristics of 40%. The multilayer structure makes it complex to fabricate. A ring loaded circular patch in [19] covers the bandwidth from 4.27 to 8.72 GHz.

In the reported works, the UWB structures are found to be at either exceptionally large or small with gain variations. The modern RF communication systems require the antennas to be compact in size, so that they could easily be embedded. Therefore, this research presents a novel UWB antenna with a compact size of 225 mm<sup>2</sup> and flat gain of 1.2–1.4 dBi. The proposed antenna is well compact in size as compared to the published literature and is suitable for next generation UWB systems.

## 2. Antenna Design

The proposed antenna is designed on commercially available FR4 substrate with relative permittivity of 4.3 and loss tangent of 0.02. The overall dimension of the proposed antenna is  $18 \times 14 \times 1.6$  mm<sup>3</sup>. Figure 1 shows the overall view and dimension of the proposed antenna.

The printed monopole UWB antenna has been transformed in a sequence of steps. The aim of the proposed antenna was to resonate at ultrawideband range. Figure 2 shows the step-by-step design development of the proposed antenna. In stage 1, a square frame tilted at 45° with half ground plane was introduced. In this stage, the resonance response achieved was almost 1.5 GHz ranging from 7 to 8.5 GHz. The second stage in the evolution introduced a square slot on the ground plane. The ground slot improved the reflection coefficient response up to 2.5 GHz. Then, the introduction of the square frames at 2.5 mm distance resulted in the proposed design, in which the resonance frequency shifted from 3.2 to 11.6 GHz. Also, the design showed the minimum reflection coefficient value of  $-29$  dB at 6.3 GHz frequency.

*2.1. Parametric Analysis.* The proposed antenna has been tuned in number of steps to achieve the desired frequency

band response. There were several parameters such as ground slot and transmission line length and width that involved in constant analysis. Figure 3 shows the complete parametric analysis of our proposed design.

In Figure 3(a), it can be seen that the effect of the ground slot on the resonance response of the antenna is captivating. As the ground slot increases in size, the resonance response gets wider and the higher frequency response gets generated. This is limited to a certain threshold value of 4.25 mm, which exhibits the desired frequency response of the proposed antenna. After this point, the antenna starts exhibiting the dual band nature.

The distance between the square frames has been set at 2.5 mm. In Figure 3(b), the effect of the antenna on resonance has been observed. By looking at the figure, it is obvious that the increasing distance causes the antenna to be more focused in lower band and the response of the bandwidth decreases. Similarly, the feed length of the proposed antenna shows that with lower values, its impedance mismatches and the response of the antenna diminishes. At 12 mm length, the desired bandwidth is achieved which when further increased causes the bandwidth to abrupt.

## 3. Results and Discussion

This section discusses the results from the fabricated prototype and their comparison with the simulated results. The propose antenna is fabricated using the LPFK machine, and the measured reflection coefficient is found to be in good agreement with the simulated results. Slight variations are found in the measured results, but they can be attributed to the cable losses, connector losses, and random measurement set up losses. Figure 4 shows the fabricated prototype with simulated and measured reflection coefficient.

The performance parameters of the proposed antenna are shown in Figure 5. The peak gain simulated is found to be 1.4 dBi, while the measured gain is found to be at 1.389 dBi. The efficiency of the proposed antenna ranges from 60 to 68%. The gain is found to be at acceptable levels; since the proposed antenna is compact in size, the gain can be considered on satisfactory levels considering the size of the proposed antenna.

*3.1. Radiation Patterns.* The radiation patterns of the antenna both simulated and measured in phi 90 and theta 90 plane are shown in Figure 6. The radiation patterns of the proposed antenna were measured in an anechoic chamber. The antenna showed well-measured radiation patterns, and it can be observed that antenna exhibits an omnidirectional response. The radiation patterns measured are from 4.5, 5.5, 6, and 7 GHz. From the figure, it can be observed that the radiation patterns are stable across the entire bandwidth. The simulated and measured results slight variations can be due to the measurement set up errors. In phi 90 plane, the antenna exhibits a directional response at some frequency points. Overall, the

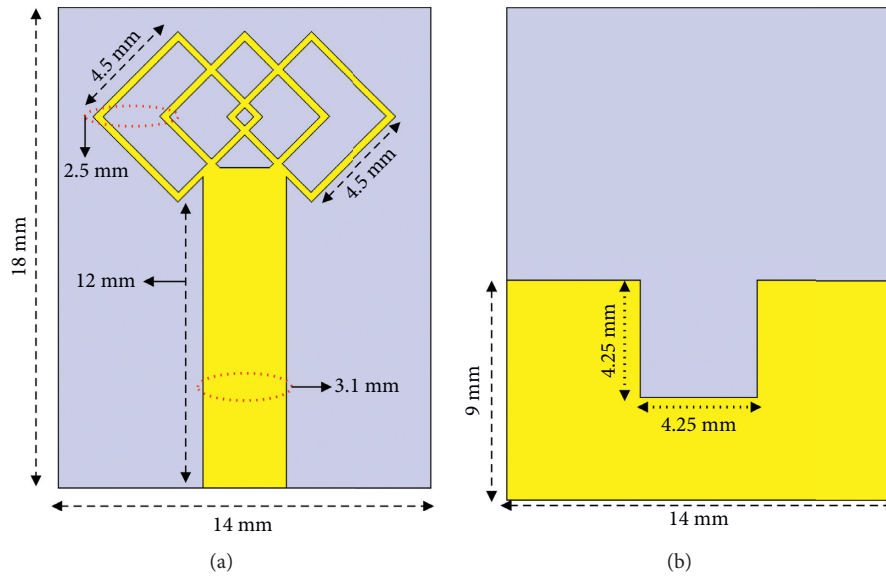


FIGURE 1: Proposed antenna design. (a) Front. (b) Back.

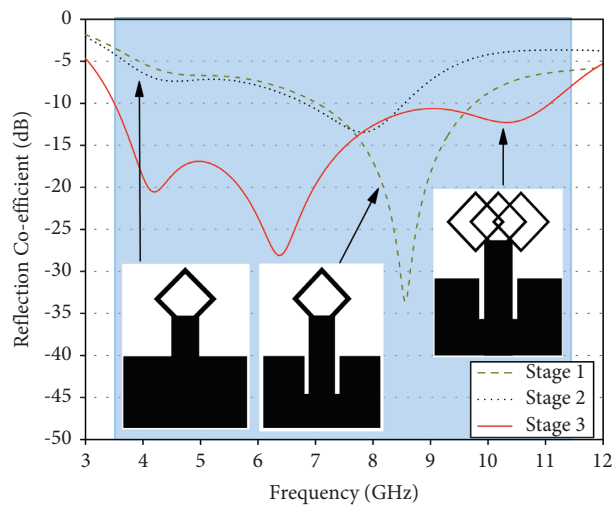


FIGURE 2: Design evolution of the proposed antenna.

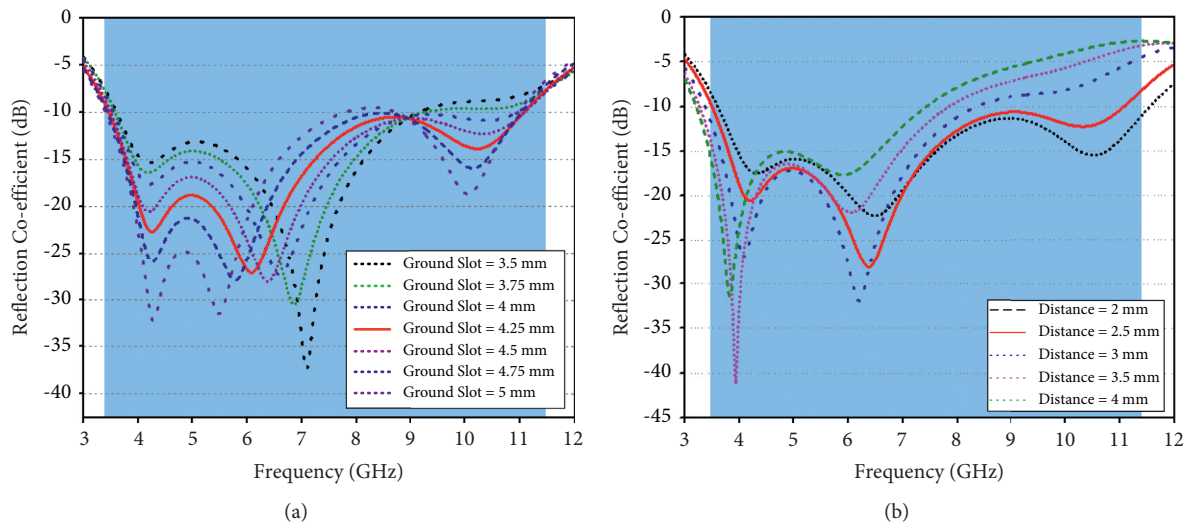


FIGURE 3: Continued.

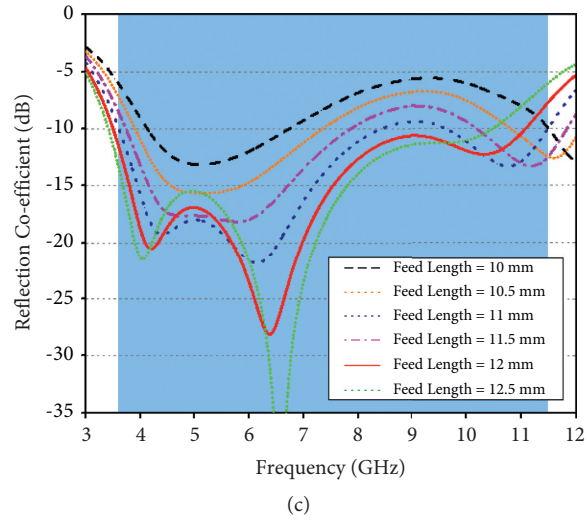


FIGURE 3: Parametric analysis of the proposed antenna. (a) Ground slot. (b) Distance. (c) Feed length.

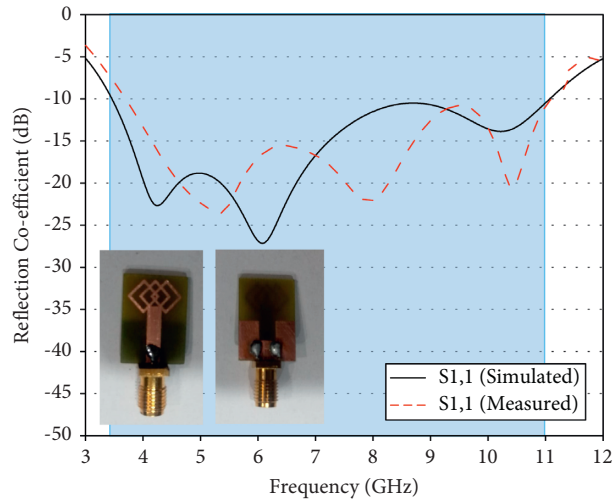


FIGURE 4: Simulated and measured reflection coefficient.

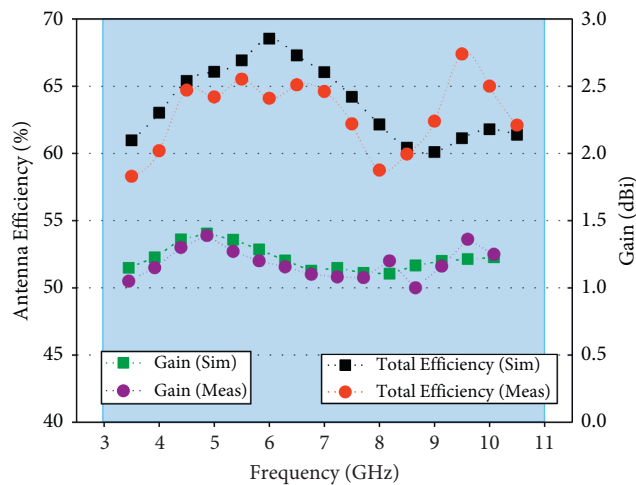


FIGURE 5: Antenna efficiency and gain parameters.

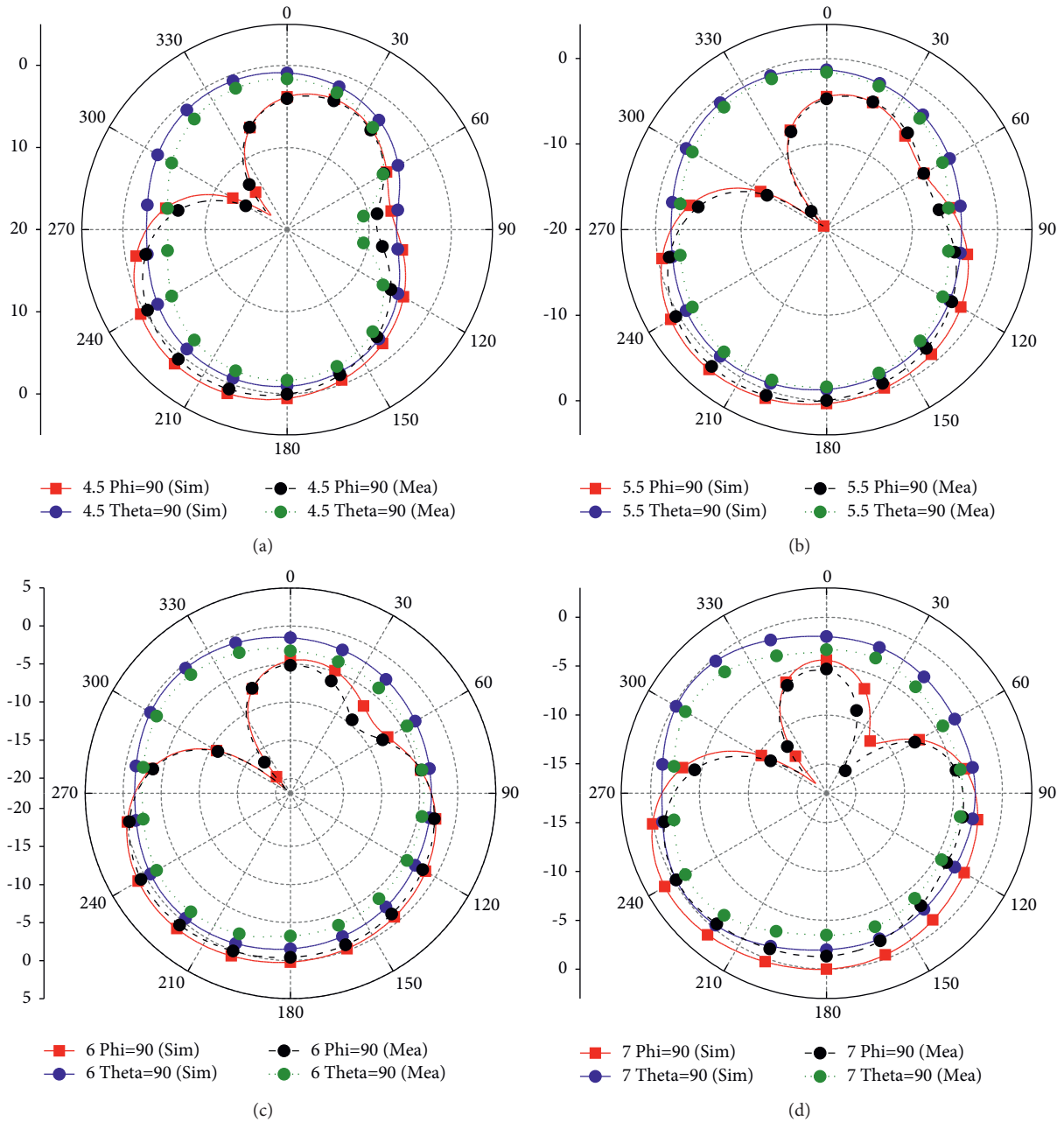


FIGURE 6: Radiation patterns. (a) 4.5 GHz. (b) 5.5 GHz. (c) 6 GHz. (d) 7 GHz.

proposed antenna shows satisfactory radiation pattern characteristics and exhibits response as required by UWB systems [11–14].

3.2. *Surface Currents.* Figure 7 shows the surface currents patterns at the resonance frequency of 4.5, 5.5, 6, and 7 GHz. From the figure, the ground slot and plane can be observed, and the titled square frames are responsible for

generating the resonances. The ground slot is helpful in generating the constructive interface of currents. Furthermore, in lower frequency values, the effect of the square frames can be seen forming constructive interface at the edges of the frames.

From Table 1, it can be seen that the proposed antenna is compact in size, and also, the gain throughout the frequency range is nearly flat. Also, the proposed antenna offers omnidirectional radiation characteristics. With this small

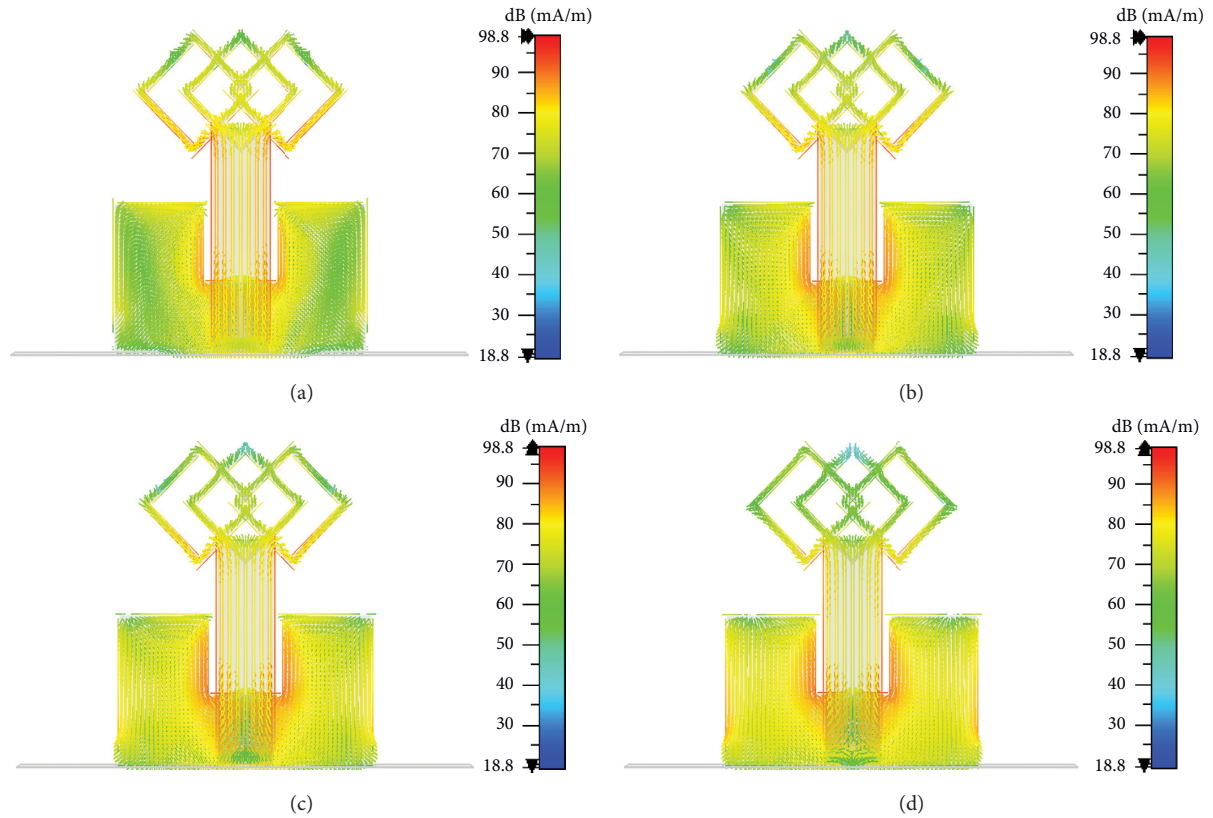


FIGURE 7: Surface current patterns. (a) 4.5 GHz. (b) 5.5 GHz. (c) 6 GHz. (d) 7 GHz.

TABLE 1: Comparison table of proposed antenna with published literature.

Reference	Frequency (GHz)	Size (L × W)	Gain (dBi)	Efficiency (%)
[5]	3.4–8.0	312 × 121	3.99	79
[6]	3.3–10.2	31 × 23	4.1	N/A
[9]	3.25–8.85	100 × 160	5.4	85
[10]	3.1–10.6	25 × 26	3.83	76
[11]	2.5–12	50 × 50	N/A	N/A
[12]	3.2–10.6	40 × 40	4.00	88
[13]	4.0–12.0	50 × 35	5.25	80
[14]	3–14.5	40 × 34	2.4	75
[20]	4.8–5.9	30 × 35	5.3	65
[21]	4.4–4.6/5.4–5.6	26 × 25	4.89	N/A
[22]	2.4 × 3.6	26.1 × 25.4	5.6	82
Proposed	3.3–11.5	14 × 18	1.4	60–68

size and robust characteristics, the reported literature can be termed as a compact and potential candidate for future wireless systems.

#### 4. Conclusion

This research presents a novel three square tilted frame monopole antenna with a compact size. The proposed antenna is made with a square cut in the top middle section of the ground plane which helps in generating the wideband response from 3.3 to 11.6 GHz frequency. The total size of the antenna is  $14 \times 18 \times 1.6 \text{ mm}^3$ , which is quite small as compared to published literature. Through

the performance parameters, the antenna is found to be exhibiting good response. Moreover, the proposed antenna is fabricated, and measured results are in well agreement with the simulated results which validate that the proposed antenna is a good contender for UWB applications. In future, this work can further be improved with MIMO configuration and through metasurfaces.

#### Data Availability

The data used to support the findings of this study are included within the article.

## Conflicts of Interest

The authors declare that they have no conflicts of interest.

## Acknowledgments

This project was supported by the National Natural Science Foundation of China (61861043).

## References

- [1] D. A. Sehrai, M. Abdullah, A. Altaf et al., "A novel high gain wideband mimo antenna for 5G millimeter wave applications," *Electronics*, vol. 9, no. 6, p. 1031, 2020.
- [2] C. R. Guo, W. J. Lu, Z. S. Zhang, and L. Zhu, "Wideband non-traveling-wave triple-mode slotline antenna," *IET Microwaves, Antennas & Propagation*, vol. 11, no. 6, pp. 886–891, 2017.
- [3] L. Wang, K. H. Teng, Y. Lian, and C. H. Heng, "A IR UWB timed-array radar based on 16-channel transmitter and sampling capacitor reused receiver," *IEEE Transactions on Circuits and Systems II: Express Briefs*, vol. 65, no. 7, pp. 878–882, 2018.
- [4] S. Koziel, S. Ogurtsov, W. Zieniutycz, and A. Bekasiewicz, "Design of a planar UWB dipole antenna with an integrated balun using surrogate-based optimization," *IEEE Antennas and Wireless Propagation Letters*, vol. 14, pp. 366–369, 2015.
- [5] J. Cruz, A. Serres, A. de Oliveira et al., "Bio-inspired printed monopole antenna applied to partial discharge detection," *Sensors*, vol. 19, no. 3, pp. 628–643, 2019.
- [6] P. S. Bakariya, S. Dwari, and M. Sarkar, "Triple band notch UWB printed monopole antenna with enhanced bandwidth," *AEU-International Journal of Electronics and Communications*, vol. 69, no. 1, pp. 26–30, 2015.
- [7] K. Nakprasit, A. Sakonkanapong, and C. Phongcharoenpanich, "Elliptical ring antenna excited by circular disc monopole for UWB communications," *International Journal of Antennas and Propagation*, vol. 2020, Article ID 8707182, 11 pages, 2020.
- [8] M. Frank, F. Lurz, M. Kempf, J. Rober, and R. Weigel, "Miniaturized ultra-wideband antenna design for human implants," in *Proceedings of the IEEE Radio and Wireless Symposium*, pp. 48–51, San Antonio, TX, USA, January 2020.
- [9] S. A. Omar, A. Iqbal, O. A. Saraereh, and A. Basir, "An array of M-shaped Vivaldi antennas for UWB applications," *Progress In Electromagnetics Research Letters*, vol. 68, pp. 67–72, 2017.
- [10] N. Ahmad Jan, S. Hassan Kiani, F. Muhammad et al., "V-shaped monopole antenna with chichena itzia inspired defected ground structure for UWB applications," *Computers, Materials & Continua*, vol. 65, no. 1, pp. 19–32, 2020.
- [11] I. B. Vendik, A. Rusakov, K. Kanjanasit, J. Hong, and D. Filonov, "Ultrawideband (UWB) planar antenna with single-, dual-, and triple-band notched characteristic based on electric ring resonator," *IEEE Antennas and Wireless Propagation Letters*, vol. 16, pp. 1597–1600, 2017.
- [12] F. Amin, R. Saleem, T. Shabbir, S. u. Rehman, M. Bilal, and M. F. Shafique, "A compact quad-element UWB-MIMO antenna system with parasitic decoupling mechanism," *Applied Sciences*, vol. 9, no. 11, p. 2371, 2019.
- [13] R. Kumar, R. R. Krishna, and N. Kushwaha, "A fractal monopole antenna for UWB applications," in *Proceedings of the IEEE Applied Electromagnetics Conference*, pp. 1-2, Bhubaneswar, India, December 2013.
- [14] C. Hua, Y. Lu, and T. Liu, "Printed UWB heart-shaped monopole antenna with band-notch reconfigurability," in *Proceedings of the IEEE International Workshop on Electromagnetics: Applications and Student Innovation Competition*, pp. 1–3, Nanjing, China, May 2016.
- [15] W. A. Awan, A. Zaidi, N. Hussain, A. Iqbal, and A. Baghdad, "Stub loaded, low profile UWB antenna with independently controllable notch-bands," *Microwave and Optical Technology Letters*, vol. 61, no. 11, pp. 2447–2454, 2019.
- [16] A. Iqbal, A. Smida, N. Mallat, M. Islam, and S. Kim, "A compact UWB antenna with independently controllable notch bands," *Sensors*, vol. 19, no. 6, p. 1411, 2019.
- [17] A. Iqbal, O. A. Saraereh, and S. K. Jaiswal, "Maple leaf shaped UWB monopole antenna with dual band notch functionality," *Progress In Electromagnetics Research C*, vol. 71, pp. 169–175, 2017.
- [18] A. Lalbakhsh, M. U. Afzal, K. P. Esselle, and S. L. Smith, "Wideband near-field correction of a fabry-perot resonator antenna," *IEEE Transactions on Antennas and Propagation*, vol. 67, no. 3, pp. 1975–1980, 2019.
- [19] B. Mohamadzade, R. B. V. B. Simorangkir, R. M. Hashmi, and A. Lalbakhsh, "A conformal ultrawideband antenna with monopole-like radiation patterns," *IEEE Transactions on Antennas and Propagation*, vol. 68, no. 8, pp. 6383–6388, 2020.
- [20] J. Iqbal, "Circularly polarized bandwidth enhancement using hollow cylindrical DRA," in *Proceedings of the 2017 International Conference on Engineering Technology and Technopreneurship (ICE2T)*, pp. 1–4, Kuala Lumpur, Malaysia, September 2017.
- [21] U. Illahi, M. I. Sulaiman, J. Iqbal, M. Alam, and M. S. Mazliham, "A novel singly fed wideband circularly polarized rectangular dielectric resonator antenna using hook-shaped metal strip," *Sind University Research Journal*, vol. 50, no. 3D, pp. 59–62, 2018.
- [22] U. Illahi, J. Iqbal, M. Sulaiman, M. Alam, S. Mazliham, and H. Jamaluddin, "Circularly polarized rectangular dielectric resonator antenna excited by an off-set conformal metal strip," *Indonesian Journal of Electrical Engineering and Computer Science*, vol. 15, no. 2, pp. 902–909, 2019.

## Research Article

# Square-Framed *T* Shape mmwave Antenna Array at 28 GHz for Future 5G Devices

Saad Hassan Kiani <sup>1</sup>, Xin Cheng Ren <sup>2</sup>, Adil Bashir <sup>3</sup>, Ammar Rafiq <sup>4</sup>,  
Muhammad Rizwan Anjum <sup>5</sup>, Mian Muhammad Kamal<sup>6</sup>, Burhan Ud Din <sup>1</sup>,  
and Fazal Muhammad <sup>7</sup>

<sup>1</sup>Electrical Engineering Department, City University of Science and Information Technology, Peshawar 25000, Pakistan

<sup>2</sup>School of Physics and Electronic Information, Yanan University, Yanan 761000, China

<sup>3</sup>Electrical Engineering Department, Bahauddin Zakariya University, Multan, Pakistan

<sup>4</sup>Department of Computer Science, NFC Institute of Engineering & Fertilizer Research, Faisalabad, Pakistan

<sup>5</sup>Department of Electronic Engineering, The Islamia University of Bahawalpur, Bahawalpur 63100, Pakistan

<sup>6</sup>School of Information Engineering, Zhengzhou University, Zhengzhou 450001, China

<sup>7</sup>Department of Electrical Engineering, University of Engineering Technology, Mardan 23200, Pakistan

Correspondence should be addressed to Xin Cheng Ren; [xchren@yau.edu.cn](mailto:xchren@yau.edu.cn)

Received 6 August 2021; Revised 21 August 2021; Accepted 25 August 2021; Published 13 September 2021

Academic Editor: Muhammad Inam Abbasi

Copyright © 2021 Saad Hassan Kiani et al. This is an open access article distributed under the Creative Commons Attribution License, which permits unrestricted use, distribution, and reproduction in any medium, provided the original work is properly cited.

In this research, a novel *T* shape antenna is proposed for millimetre-wave (mmwave) 5G systems. Designed on 0.254 mm thin Rogers 5880 substrate with a dielectric constant of 2.3 and the loss tangent of 0.0009, the proposed antenna offers a wideband characteristics of nearly 8 GHz with gain of 4.25 dBi for single element. Based on these characteristics, the single element is further constructed into a four-element linear array with a compact size of  $18.5 \times 24 \text{ mm}^2$ . The proposed antenna array exhibited dual beam radiation patterns with a high realized gain of 11.5 dBi and 94% efficiency. The measured results from the fabricated prototype well agree with the simulated results and thus, therefore, make the proposed antenna system a well-suited candidate for future mmwave devices.

## 1. Introduction

With evolution of the universal telecommunication system, 5G technology has now become the centre of interest due to its higher data rates' capacity. The higher data rates are directly associated to bandwidth; therefore, radio frequency (RF) front ends operating at millimetre-wave part of the spectrum have drawn significant attention of the researchers. According to feasibility reports, mmwave spectrum is a promising candidate for 5G services providing high-data rates and low latency over the entire band [1]. Several frequency bands have been allotted for 5G standards including 28 and 38 GHz as most prominent (O2 band) and 164–200 GHz (H2O band) as unlicensed spectrum [2, 3]. As the higher spectrum is free of applications as compared to

sub 6 GHz which has immense pressure of application on it, the mmwave spectrum is quite sensitive to the atmospheric attenuations since, in mmwave, the wavelength becomes critically small, and such sensitivity can alter the signal strength which can depreciate experience of 5G. These atmospheric attenuation challenges can be overcome by deploying antennas with high gain levels. Antenna arrays offer higher gain and directivity levels. By implying higher gain antenna assemblies, the atmospheric conditional effects become mitigated and service becomes reliable [4].

Different studies on the mmwave spectrum have shown limitations. The physical dimensions of the antenna systems at mmwave become critically smaller; also, the wavelength becomes critical to fading environments. A four-port antenna system is presented in [5] with conical rings for

28 GHz mmwave applications. The antenna elements are well isolated offering pattern diversity characteristics, but the gain of the MIMO system is very low. Similarly, a nature-inspired four-element MIMO antenna in [6] offers pattern and spatial diversity characteristics, but the bandwidth of the antenna is very low. Substrate integrated waveguides (SIW) are known to have negligible line losses. SIW have been extensively researched in mmwave antenna arrays. In [7], a SIW antenna array offering high gain of 14 dBi is presented. The array has very low-side lobes and offers good dimensions of  $63 \times 70 \text{ mm}^2$ , but the Vias assembly in the proposed study makes it difficult to assemble in RF circuits. An mmwave antenna array covering 57–71 GHz spectrum with a high gain of 26 dBi is presented in [8]. Although the size of the antenna is relatively small, i.e.,  $28.8 \times 28.8 \text{ mm}^2$ , it is complex in nature to assemble due to its multilayer structure and bonding films. In [9], with the high efficiency of 85%, a four-element array with SIW is presented having the gain of 12 dBi. Although the gain and bandwidth of the proposed antenna is satisfactory, with less than 1 mm apart, Vias present in the structure makes the reported literature too bulky. As compared to SIW, planar antenna arrays are simple and easy to develop [10–12]. In [13], a four-element snowflake antenna array is presented. The gain of the antenna is nearly 10 dBi with narrow beam width for future mmwave devices. In [14], a small  $3 \times 3$  planar structure is presented in [15] with small size of  $400 \text{ mm}^2$  and gain above 15 dBi at 28 GHz, and the relative bandwidth of 1.7 GHz offered by the antenna is very low. Similarly, a super wide band planar antenna offering 17 GHz bandwidth from 23 to 40 GHz is presented in [15] with gain above 10 dBi over the entire band of interest; the size of the antenna is quite large up to  $80 \times 80 \text{ mm}^2$  with extensive side lobe levels.

In this paper, a simple *T* shape planar antenna embedded in a frame is presented. The proposed antenna is transformed into four-element linear array in order to increase the gain of the proposed antenna. Through its narrow dual beam width nature, good gain, and efficiency, the proposed antenna can be termed as potential candidate for future RF mmwave devices.

## 2. Antenna Design

The propose antenna element is designed on ultra-thin Rogers 5880 with relative permittivity of 2.3 and thickness of 0.254 mm. The proposed design is shown in Figure 1. Figure 1(a) shows the front face of the proposed structure, while Figure 1(b) shows the back side of the proposed resonating structure. The length and width of proposed design is  $10 \times 12 \text{ mm}$ . The dimensions of proposed design are  $X = 8 \text{ mm}$ ,  $Y = 10 \text{ mm}$ ,  $C = 4.65 \text{ mm}$ ,  $GSX = 1.4 \text{ mm}$ ,  $GSY = 1.4 \text{ mm}$ ,  $FX = 0.9 \text{ mm}$ ,  $FY = 6 \text{ mm}$ ,  $T1 = 2 \text{ mm}$ ,  $T2 = 2 \text{ mm}$ ,  $S1 = 3.15 \text{ mm}$ , and  $S2 = 3.15 \text{ mm}$ .

The main aim of the design was to resonate at the central frequency of 28 GHz which was achieved with a series of steps. Figure 2 shows the reflection coefficient response of design evolution.

Stage 1 comprised of feed line at 6 mm length which was introduced with a small extension above in stage 2. A

horizontal strip was added at the top of extension presented in stage 2, hence forming a *T* shape resonator, but the desired response was not achieved. A square shape frame surrounding a *T* shape was then introduced which produced a strong dip at the central frequency of 28 GHz with bandwidth ranging from 25.2 to approximately 37 GHz, as shown in Figure 2.

*2.1. Parametric Analysis.* The *s*-parameter response of the proposed antenna was evolved through parametric studies. Figure 3 shows the parametric study details of different antenna parameters. The length of the feed is chosen above 5 mm in order to embed it with the RF connector. The parametric studies presented in Figure 3 show how a small change in a parameter significantly alters the *S*-parameter response.

In Figure 3(a), the impact of feed length on the reflection coefficient is presented. The length of the feed at small intervals of 0.2 mm is observed. It can be seen that, as the length of the feed decreases the reflection-coefficient response decreases in magnitude. At 6 mm length, the feed length exhibits a sharp resonance at the desired frequency of 28 GHz. Similarly, the ground plane of the design is introduced with the square slot at the top-middle section. The optimized value obtained of the square ground slot is 1.4 mm. Now, the length and the width of the slot is change with 1 mm value in range of 1.3 to 1.7, and it is observed that, as the dimension of the square slot increases, the reflection coefficient response is shifted forward and improves in decibels' value.

Figure 3(c) shows the parametric response of the length of *S1*. The length of *S1* plays a significant role in shifting the resonance from the desired frequency of interest. It is observed that this parameter, also with increasing value, shifts the response to lower frequency position. Also, the value of the reflection coefficient decreases, hence showing the occurrence of impedance mismatch. At last, Figure 3(d) shows the resonance response of the parameter *S2* which shows that the width of *S2* affects the impedance matching of the antenna, and as the width decreases, the resonance response gets frail.

Figure 4 shows the performance parameter of proposed antenna. The total efficiency of proposed antenna is above 90% and 97.5% at the frequency of interest with gain ranging in between 4 and 4.5 dBi. The high-performance parameters indicate that the proposed design is highly efficient.

*2.2. Array Transformation.* The proposed antenna is transformed into four-element linear array for better performance characteristics. Since 5G systems required narrow beam width and high gain, the antenna arrays generally offer such characteristics. A four-element array is prepared using four-element feed network, as shown in Figure 5. The overall dimensions of the four element array is  $24 \times 18.5 \text{ mm}$ , while the length of the ground plane is 12.85 mm. The surface current distribution has been shown in Figure 6 at 28 GHz which shows that the current is distributed symmetrically between the radiating elements.

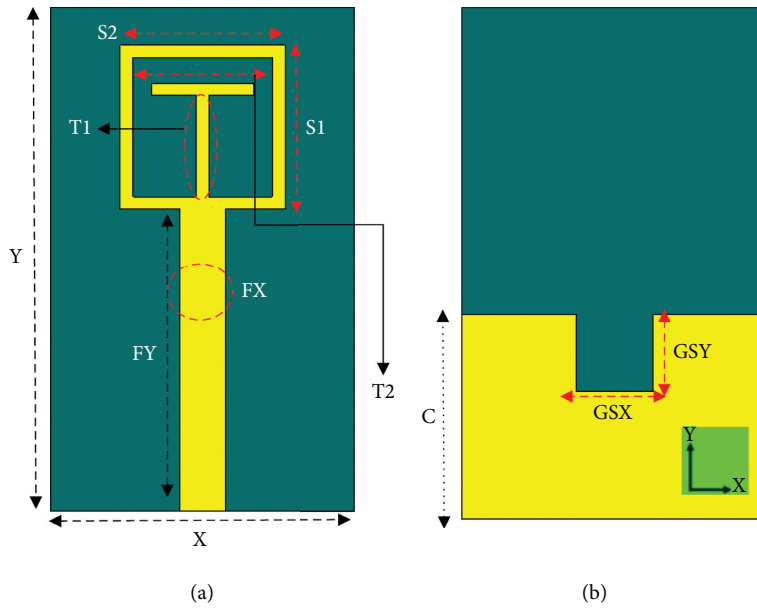


FIGURE 1: Proposed antenna design: (a) front and (b) back.

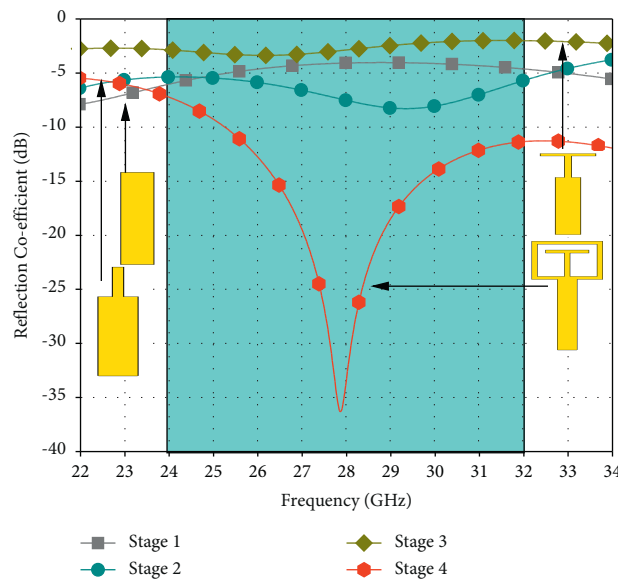


FIGURE 2: Design evolution.

### 3. Results and Discussion

The proposed antenna array is fabricated using LPFK machine and is tested using the vector network analyzer. Figure 7 shows the fabricated antenna prototype both front and back side.

The simulated and measured reflection coefficient response of the four-element antenna array is shown in Figure 8. In the resonance bandwidth of the array, although reduced to 25.5 to 30 GHz, a slight shift in the measured reflection coefficient has been observed which can be attributed to the connector, cable losses, or human errors, but overall performance of the system is satisfactory.

The simulated and measured total efficiency with gain over the desired band of interest is given in Figure 9. Both simulated and measured efficiency of the proposed antenna is above 88% in the entire operational band of the antenna. Upon the formation of the proposed single-element antenna into a four-element array, the increase in gain achieved was 7 dBi. Thus, at the main resonance frequency, the gain value achieved is 11.5 dBi, which is very desirable for mmwave systems.

**3.1. Radiation Patterns.** In this section, the radiation patterns of the proposed antenna array in both principle  $\Phi = 90$  and  $\Phi = 0$  planes are presented. Figure 10(a) shows

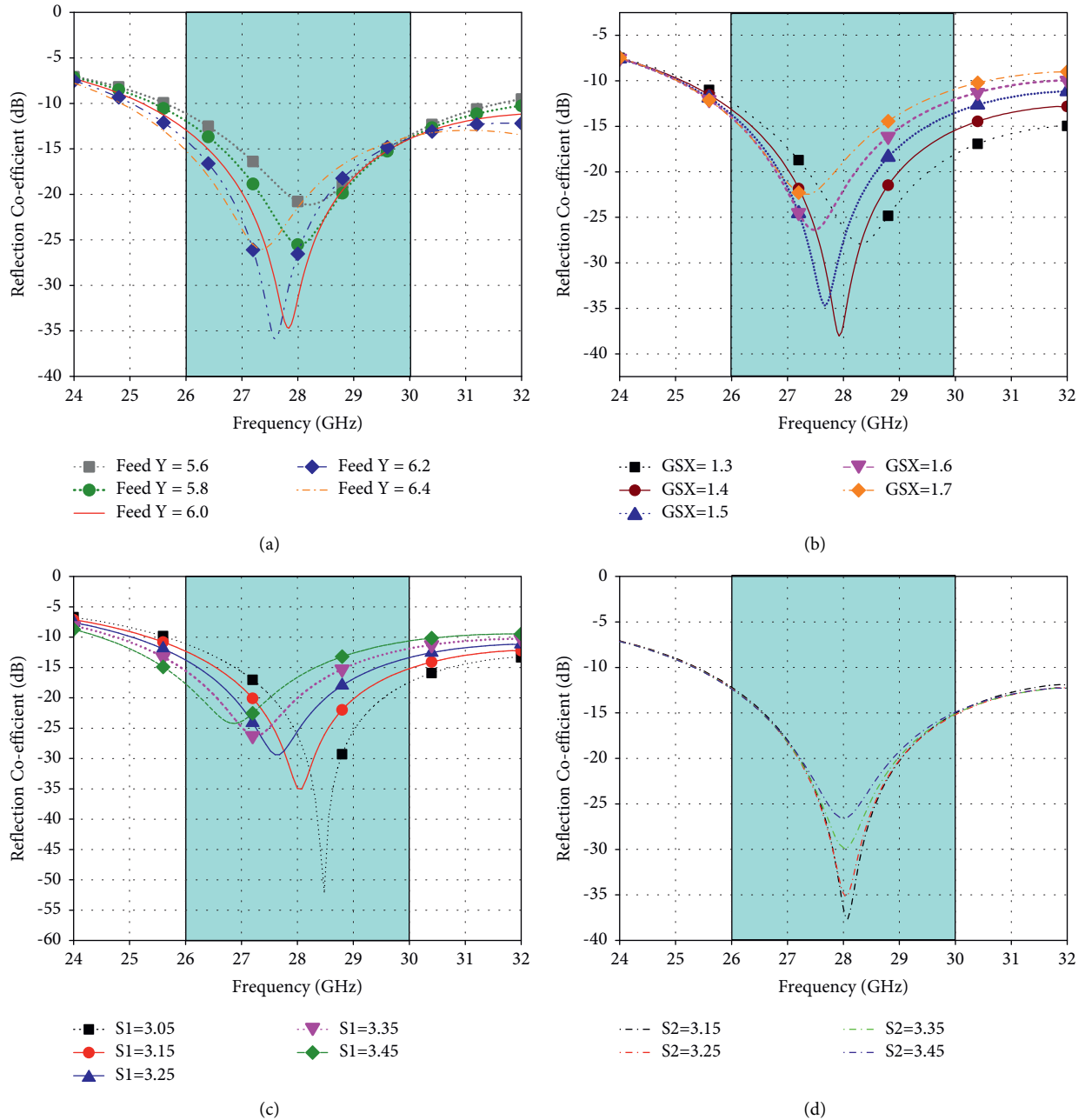


FIGURE 3: Parametric analysis with respect to (a) FY, (b) GSX, (c) S1, and (d) S2.

the  $\Phi = 90^\circ$  plane by which it can be seen that proposed antenna with exclusion of two nulls is radiating in all directions, whereas in  $\Phi = 0^\circ$  plane, the proposed antenna array is highly directive with the beam width of 20 degrees only. From  $\Phi = 0^\circ$  plane in Figure 10(b), it can be seen that the proposed antenna offers dual beam characteristics located at 180 degree which can be confirmed by 3D gain radiation patterns in Figure 11. The simulated and measured radiation vary each other with slight variations only. With measured gain of 11.5 dBi and high efficiency, the proposed antenna array can be said as a potential candidate for future

mmwave RF devices. Table 1 shows the proposed antenna structure comparison with published literature. From the table, it can be seen that the proposed antenna is simple planar in structure with no complex feeding mechanism. The gain of the antenna is better and the bandwidth of the proposed antenna is better covering the desired band with efficiency 94% at the desired frequency of interest. Hence, it can be concluded that the proposed antenna has good performance characteristics with compact size and thus can be termed as potential candidate for future mmwave RF front ends.

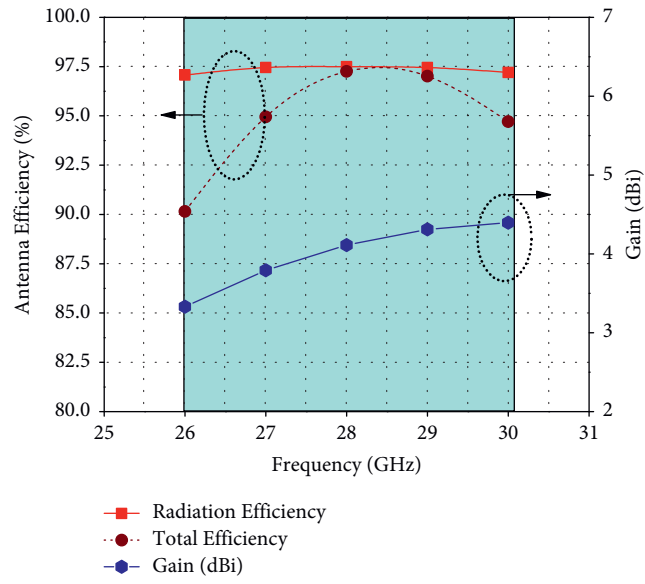


FIGURE 4: Performance parameters of proposed antenna.

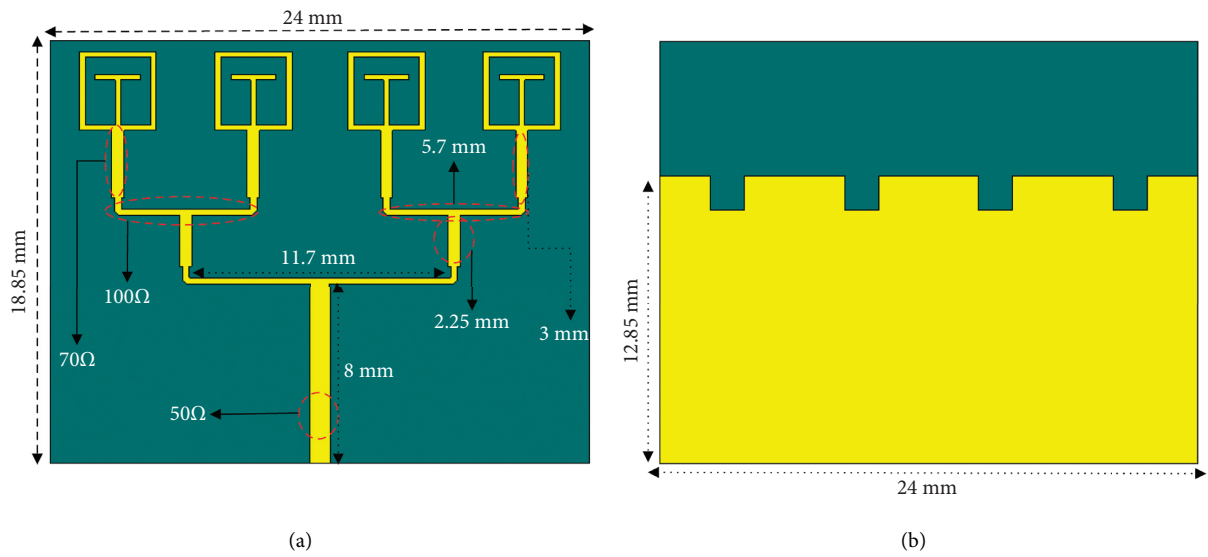


FIGURE 5: Four-element antenna array: (a) front view; (b) back view.

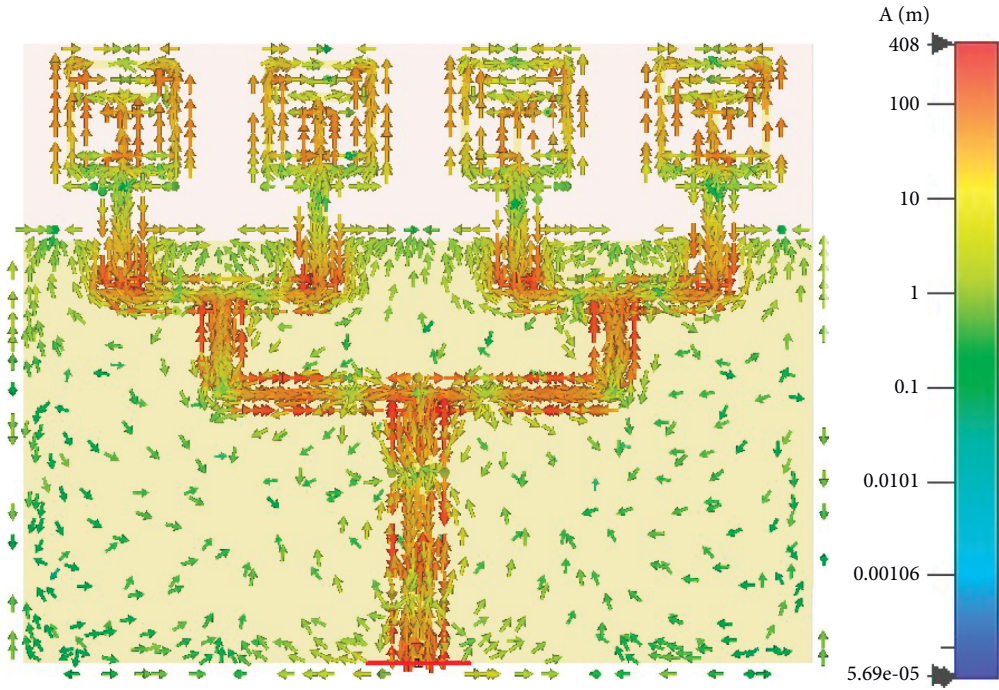


FIGURE 6: Surface current distribution at 28 GHz.

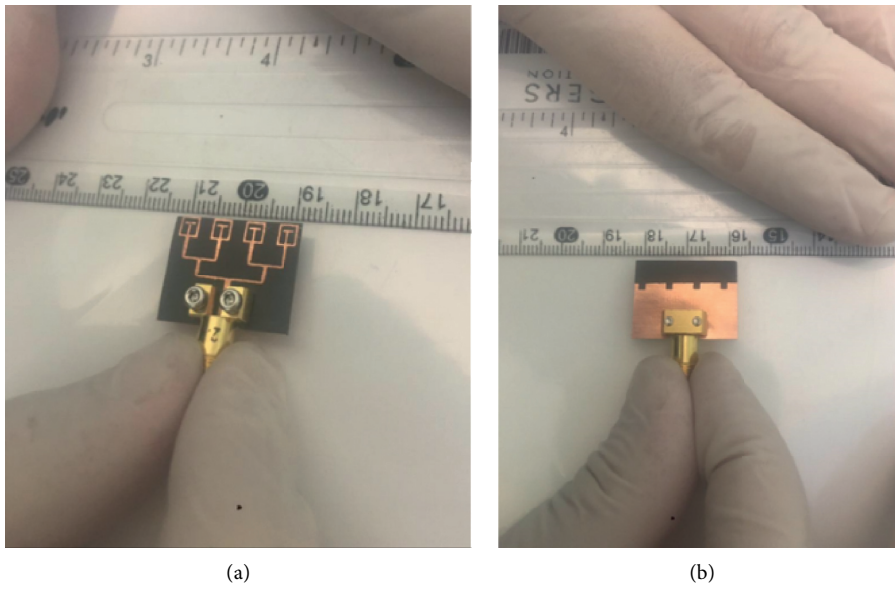


FIGURE 7: Fabricated antenna array prototype: (a) front view; (b) back view.

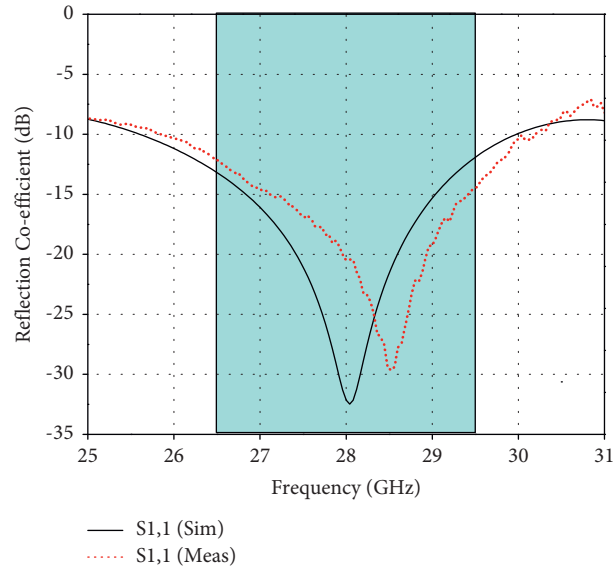


FIGURE 8: Simulated and measured reflection coefficient response of the proposed antenna array.

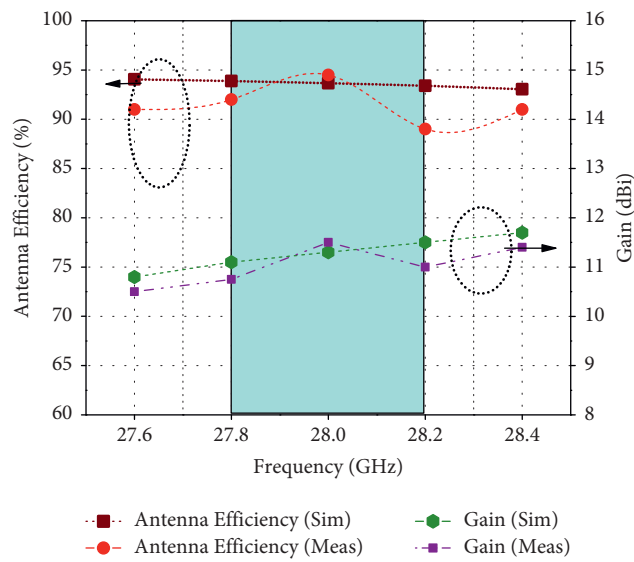


FIGURE 9: Simulated and measured array performance parameters.

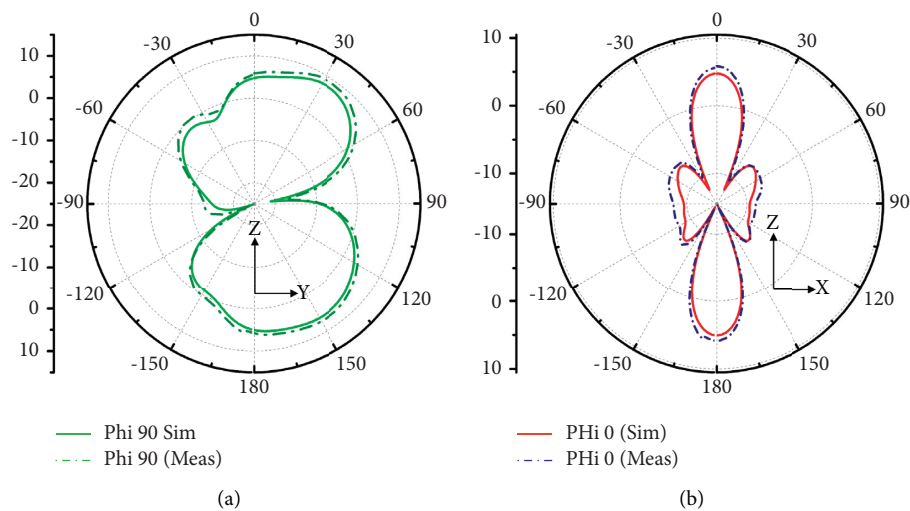


FIGURE 10: Radiation pattern of proposed array at 28 GHz: (a)  $\Phi = 90^\circ$ ; (b)  $\Phi = 0^\circ$ .

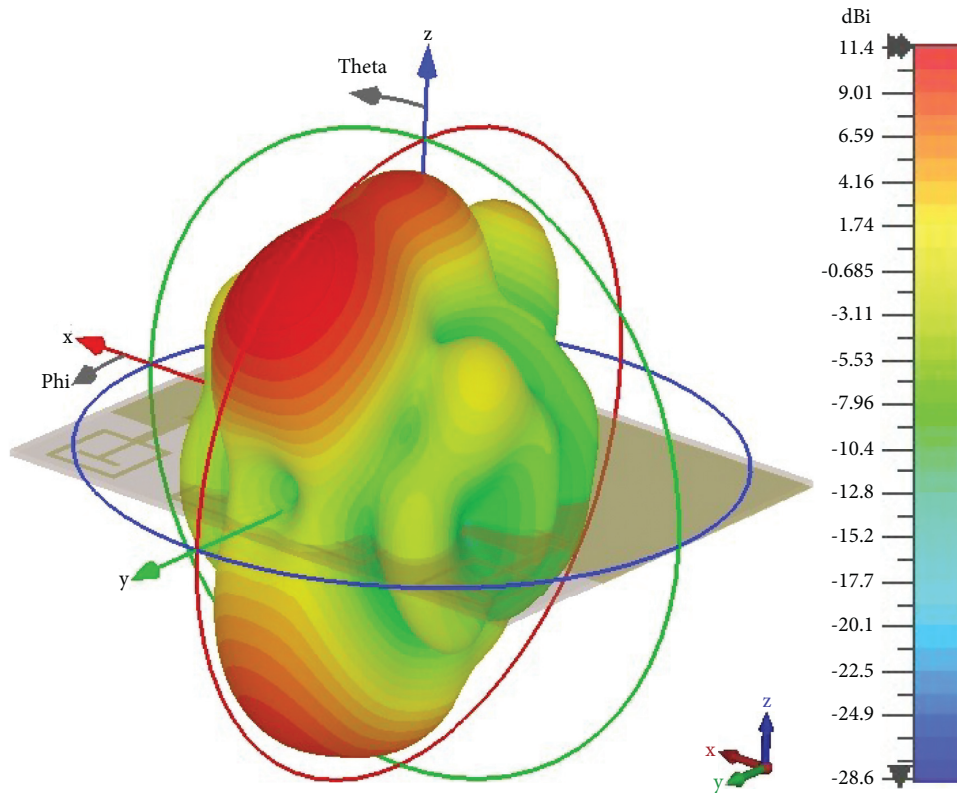


FIGURE 11: 3D radiation pattern at 28 GHz.

TABLE 1: Comparison table of proposed antenna with published literature.

Ref	Antenna elements	Configuration	Bandwidth (GHz)	Size in mm (L × W)	Efficiency (%)	Gain (dBi)
5	2 × 2	Planar	3	30 × 30	75	5.5
6	2 × 2	Planar	2.5	30 × 30	78	7
7	1 × 8	SIW	2.3	63.5 70	62	13.5
9	1 × 4	SIW	9	20 × 45	84	12.1
10	1 × 4	Planar	0.6	20 × 26	90	10
15	2 × 2	1 × 4	17	80 × 80	92	11.75
13	1 × 4	Planar	2.9	37 × 14.5	83	10.5
Proposed	1 × 4	Planar	4	18.5 × 24	94	11.5

#### 4. Conclusion

In this paper, a novel *T* shape planar antenna structure is presented for mmwave 28 GHz applications. The gain of the proposed antenna is 4.25 dBi for single element and efficiency is greater than 97% at 28 GHz. The proposed *T* shape antenna is transformed in four-element linear array manner and up to 11.5 dBi of high gain is achieved with radiation characteristics of two narrow beams at 180 and 0 degrees. The overall size of the antenna array is up to 18.5 × 24 mm and the measured results from fabricated prototype well agree with simulated results. Because of efficient performance, features, and unique design, the proposed antenna can be termed as a potential candidate for future high-speed mmwave communication systems.

#### Data Availability

The data used to support the findings of the study are included within the article.

#### Conflicts of Interest

The authors declare no conflicts of interest.

#### Acknowledgments

This project was supported by National Natural Science Foundation of China (61861043).

## References

- [1] J. Zhang, X. Yu, and K. B. Letaief, "Hybrid beam forming for 5G and beyond millimeter-wave systems: a holistic view," *IEEE Open Journal of the Communications Society*, vol. 1, pp. 77–91, 2019.
- [2] R. Przesmycki, M. Bugaj, and L. Nowosielski, "Broadband microstrip antenna for 5G wireless systems operating at 28 GHz," *Electronics*, vol. 10, p. 1, 2021.
- [3] G. Kim and S. Kim, "Design and Analysis of dual polarized broadband microstrip patch antenna for 5G mmwave antenna module on FR4 substrate," *IEEE Access*, vol. 9, pp. 64306–64316, 2021.
- [4] M. B. Almashhdany, A. A. Oras, M. S. Ahmed, A. Mohamed, H. Naba, and A. Fatima, "Design of multi-band slotted mmwave antenna for 5G mobile applications," in *Proceedings of the IOP Conference Series: Materials Science and Engineering*, April 2020.
- [5] M. M. Kamal, S. Yang, X.-c. Ren et al., "Infinity shell shaped mimo antenna array for mm-wave 5G applications," *Electronics*, vol. 10, no. 2, p. 165, 2021.
- [6] S. Rahman, X.-c. Ren, A. Altaf et al., "Nature inspired MIMO antenna system for future mmwave technologies," *Micro-machines*, vol. 11, no. 12, p. 1083, 2020.
- [7] S. J. Park, D. H. Shin, and S. O. Park, "Low side-lobe substrate-integrated-waveguide antenna array using broadband unequal feeding network for millimeter-wave handset device," *IEEE Transactions on Antennas and Propagation*, vol. 64, pp. 923–932, 2015.
- [8] Q. Zhu, K. B. Ng, C. H. Chan, and K.-M. Luk, "Substrate-Integrated-Waveguide-Fed array antenna covering 57–71 GHz band for 5G applications," *IEEE Transactions on Antennas and Propagation*, vol. 65, no. 12, pp. 6298–6306, 2017.
- [9] H. Ullah and F. A. Tahir, "A broadband wire hexagon antenna array for future 5G communications in 28 GHz band," *Microwave and Optical Technology Letters*, vol. 61, no. 3, pp. 696–701, 2019.
- [10] J. Khan, D. A. Sehrai, and U. Ali, "Design of dual band 5G antenna array with SAR Analysis for future mobile handsets," *Journal of Electrical Engineering & Technology*, vol. 14, no. 2, pp. 809–816, 2019.
- [11] G.-H. Sun and H. Wong, "A planar millimeter-wave antenna array with a pillbox-distributed network," *IEEE Transactions on Antennas and Propagation*, vol. 68, no. 5, pp. 3664–3672, 2020.
- [12] Y. Ma, J. Wang, Z. Li, Y. Li, M. Chen, and Z. Zhang, "Planar annular leaky-wave antenna array with conical beam," *IEEE Transactions on Antennas and Propagation*, vol. 68, no. 7, pp. 5405–5414, 2020.
- [13] H. Ullah and F. A. Tahir, "A novel snowflake fractal antenna for dual-beam applications in 28 GHz Band," *IEEE Access*, vol. 8, pp. 19873–19879, 2020.
- [14] M. Khalily, R. Tafazolli, T. Rahman, and M. Kamarudin, "Design of phased arrays of series-fed patch antennas with reduced number of the controllers for 28 GHz mm-wave applications," *IEEE Antennas and Wireless Propagation Letters*, vol. 15, pp. 1305–1308, 2015.
- [15] D. A. Sehrai, M. Abdullah, A. Altaf et al., "A novel high gain wideband MIMO antenna for 5G millimeter wave applications," *Electronics*, vol. 9, no. 6, p. 1031, 2020.

## Research Article

# Various Textiles-Based Comparative Analysis of a Millimeter Wave Miniaturized Novel Antenna Design for Body-Centric Communications

Mohammad Monirujjaman Khan <sup>1</sup>, Kaiserul Islam <sup>1</sup>, Md. Nakib Alam Shovon <sup>1</sup>, Mehedi Masud <sup>2</sup>, Mohammed Baz <sup>3</sup> and Mohammed A. AlZain <sup>4</sup>

<sup>1</sup>Electrical and Computer Engineering Department, North South University, Bashundhara, Dhaka 1229, Bangladesh

<sup>2</sup>Department of Computer Science, College of Computers and Information Technology, Taif University, P. O. Box 11099, Taif 21944, Saudi Arabia

<sup>3</sup>Department of Computer Engineering, College of Computers and Information Technology, Taif University, P. O. Box 11099, Taif 21944, Saudi Arabia

<sup>4</sup>Department of Information Technology, College of Computers and Information Technology, Taif University, P. O. Box 11099, Taif 21944, Saudi Arabia

Correspondence should be addressed to Mohammad Monirujjaman Khan; [monirujjaman.khan@northsouth.edu](mailto:monirujjaman.khan@northsouth.edu)

Received 4 June 2021; Accepted 20 July 2021; Published 2 August 2021

Academic Editor: Muhammad Inam Abbasi

Copyright © 2021 Mohammad Monirujjaman Khan et al. This is an open access article distributed under the Creative Commons Attribution License, which permits unrestricted use, distribution, and reproduction in any medium, provided the original work is properly cited.

A 60 GHz compact and novel shaped microstrip-fed antenna based on a textile substrate for body-centric communications has been proposed in this paper. The antenna has a partial ground, and the textile substrate is made up of 1.5 mm thick 100% polyester. Two rectangular sections from the patch antenna's radiator were removed to give the antenna a swan-shaped appearance. The antenna was designed and simulated using computer simulation technology (CST) microwave studio software. Simulated results show that, in free-space, the antenna achieved a high bandwidth of 11.6 GHz with a center frequency of 60.01 GHz. With 89.4% radiation efficiency, the maximum gain of the antenna was 8.535 dBi. For the on-body scenario, the antenna was simulated over five different distances from a human torso phantom. At the closest distance from the phantom, the antenna's gain was 5.27 dBi, while the radiation dropped significantly to 63%. The highest bandwidth of 12.27 GHz was attained at 8 mm, while the lowest bandwidth of 5.012 GHz was attained at 4 mm away from the phantom. Gain and radiation efficiency were comparable to free-space results at the furthest distance. The antenna was also simulated with ten different textile substrates for both free-space and on-body scenarios. Among these ten substrates, denim, tween, and Quartzel fabric had similar performance results as polyester. This design achieved similar performance compared to other 60 GHz textile antennas while being a bit more compact. This antenna will be a promising choice for body-centric communications because of its compact size, textile-based substrate, and excellent on-body performance.

## 1. Introduction

Advances in wireless technologies have meant an exponential increase in demand for smart wireless devices for the last few decades. These devices include emerging wearables for health and fitness. In today's world, the expectation of having every device connected to a network for the transfer of a huge amount of data is quite the norm. Due to this ever-

increasing demand for connectivity, it is apparent that current wireless bands are getting congested, and future communication will have to be in the millimeter-wave (mm-wave) spectrum [1, 2].

The mm-wave spectrum consists of frequencies between 30 to 300 GHz, which means the spectrum has a wavelength range from 10 mm to 1 mm. In free space, mm-wave has slightly higher attenuation than 4G frequencies due to high

oxygen absorption. At 60, 180, and 380 GHz frequency bands, the attenuation of mm-wave is significantly higher. Short wavelength and higher attenuation mean communication in the mm-waves spectrum is suitable for short-range indoor obstacle-free applications [1]. The Federal Communications Commission (FCC) allocated the 60 GHz band for unlicensed use in 2001 [3, 4]. Currently, the 60 GHz band is used for Wireless Gigabit Alliance (WiGig) wireless local area network (WLAN) devices. The 60 GHz band (57–64 GHz) offers a very high data rate in the gigabit per second range [3].

Wearable devices work in the vicinity of body-centric wireless communications (BCWC). BCWC includes wireless body area network (WBAN), a network of sensors around the human body. Wearable devices under WBAN have three modes of operation: on-body, off-body, and in-body. Communication between wearable devices placed in close proximity to the human body is known as on-body communication. Off-body communication is between a device placed on the human body and another device placed a few meters away from the human body. When an implant sends data to a device placed outside of the human body, it is known as in-body communication [2]. Body-centric devices may consist of medical equipment for monitoring health conditions such as heart rate and blood pressure [5]. Such devices designed for working in the 60 GHz band will have very directional and small antennas in physical size [3].

Textile antennas for WBAN are an attractive design prospect for their potential wearable uses. In general, these antennas are made from flexible conductive materials known as electro-textiles and substrate materials. Electro-textiles are made by weaving or knitting conductive threads like copper with nonconductive fabric materials. The substrate is a nonconductive material usually made of regular fabrics such as denim, polyester, and cotton. Textile antennas are practical due to their ease of integration into different fabrics, making them suitable for hospital patients' clothing, rescue workers' clothing, etc. The construction of textile antennas makes them low profile, lightweight, and low maintenance [6, 7].

Antennas designed for body-centric communication need to be evaluated appropriately under comparable human body conditions. The human body acts as a lossy medium, and it can greatly degrade the antennas' performance [8]. In [9–12], narrowband and ultra wideband antenna designs have been discussed by various authors. For these cases, none of the antennas are designed on a textile substrate. However, in [13–15], the authors presented 60 GHz antennas that are not designed on textile substrates. In addition, there are very few mm-wave antenna designs presented in [16–19]. In [15], a 60 GHz body-centric antenna is designed for on-body operation. In free space, the antenna achieved a high gain of 9.37 dB with a bandwidth of 5 GHz. For on-body performance evaluation, a phantom of the human torso was created. Even though mm-waves have a very low penetration depth on the human body, the phantom was created, taking skin, fat, and muscle layers. As a result, the antenna produced a slightly lower bandwidth but a higher maximum gain. Puskey et al. designed a disc-

like low-profile antenna that is well matched between 59.3 and 63.4 GHz [16]. The antenna lost about 25% efficiency when kept 1 mm away from a 5 mm thick skin phantom. Similar to the previous paper, depending on the antenna's distance from the phantom, the on-body maximum gain increased compared to free space. A low-profile slotted patch 60 GHz antenna was designed in [17]. The antenna has a wide bandwidth of 9.8 GHz with 74% efficiency in free space. For the on-body scenario, the antenna's efficiency decreased to 63%, but again, like in previous cases, the gain increased from 10.6 dBi to 12.1 dBi. The abovementioned mm-wave antennas are not textile based.

A 60 GHz textile antenna based on a microstrip patch array is proposed in [18]. Due to the fabrication process's complexity, instead of electro-textiles, copper foils of 0.07 mm were used for all radiating materials. For textile material, only a cotton-woven fabric of 0.2 mm was used. The antenna was fed by a 15.2 mm-long microstrip line and a V connector for performance measurements. The reflection coefficients were lower than  $-10$  dB in the 57–64 GHz range with 40.7% efficiency in free space. For human body performance, the antenna was kept at 0 and 5 mm away from a skin phantom of size  $2 \times 100 \times 100$  mm<sup>3</sup>. At the closest distance from the phantom, both the efficiency and gain of the antenna decreased. At 5 mm away from the phantom, these values increased closer to free-space values. The antenna was also subject to bending and crumpling, both of which had little effect on the antenna's performance. In [19], a similar sort of analysis has been made on a microstrip-fed Yagi-Uda antenna. The antenna consists of a driven dipole and 10 directors printed on a 0.2 mm thick fabric made of cotton. For the previously mentioned reason, the radiators are made from 0.07 mm thick copper foil. The antenna produced an end-fire radiation pattern over the 55–64 GHz range. Computed and measured maximum gain in free space was around 9.2 dBi. The antenna was evaluated on a homogeneous skin-equivalent phantom measuring  $10 \times 100 \times 100$  mm<sup>3</sup> at two different distances like in [18]. Compared to free space, the antenna's efficiency dropped to 48% from 78%, while the gain increased to 11.9 dBi. These two antennas are designed for only cotton substrates [18, 19]. One was designed for 60 GHz array antennas and another one was designed to get end-fire radiation.

Most of the studies conducted for the wearable textile antenna are based on designs working in much lower frequency bands [20–27]. Although the antennas presented in [18, 19] are textile based, they are designed for only one textile material, cotton. The antenna presented in [18] was an array antenna. The objectives and research investigation of the work [18, 19] are different from the research objectives and investigation of this paper. This paper's main objective is to propose a design of a 60 GHz antenna based on a 100% polyester substrate for wearable devices. Various textiles-based comparative analysis of a millimeter wave miniaturized novel antenna design for body-centric communications is presented here. The performance of the antenna has been compared with ten different textile substrates. Parametric studies are performed by changing various antenna parameters. The on-body performance was also investigated. In

addition, the performance also investigated placing the antenna at different distances from the human body model. Finally, the on-body performance of the antenna for various substrates has been investigated and compared.

This paper consists of six sections. The antenna's structure and its material selection are given in Section 2. Free-space performance is described in Section 3. Parametric changes were made where lengths of different parts of the antenna are altered to observe performance changes. The polyester textile substrate was replaced with ten other substrates and evaluated in free space. The simulation results are included in Section 3. For the wearable scenario, the antenna was placed over a torso phantom at 5 different distances. The on-body simulation results are detailed in Section 4. On-body simulation results for other textile substrates closest to the phantom are also included in this section. In Section 5, a brief comparison of the proposed antenna has been made with other available 60 GHz textiles. Lastly, in Section 6, conclusions are made.

## 2. Materials and Antenna Design

To minimize losses in wearable scenarios, an appropriate design should be considered for textile antennas. The antenna should be of low-profile and flexible enough so that the performance does not significantly degrade under stress [7]. This paper proposes the design of a microstrip patch antenna with the partial ground (Figures 1(a)–1(d)). Instead of electro-textile, the radiating patch and ground of the antenna are made of perfect electric conductor (PEC) with 0.035 mm thickness. The textile substrate is made of 1.5 mm thick 100% polyester, which has a dielectric constant of 1.9. The dielectric constant is the real part of relative permittivity and is an important parameter as it affects the impedance bandwidth of the antenna. Low dielectric constant reduces surface wave losses within a substrate and hence increases impedance bandwidth [7]. The overall dimension of the textile substrate is  $12.2 \times 12 \times 1.57 \text{ mm}^3$ . The electrical size of the antenna for the overall width and length of the substrate is  $0.42\lambda$  and  $0.41\lambda$ , respectively. The antenna is fed by a 4.9 mm-long and 2.15 mm-wide microstrip line. The list of antenna materials and their thickness and dielectric constant are given in Table 1. The antenna is designed and simulated using computer simulation technology (CST).

The antenna's radiating patch has a  $7.3 \text{ mm} \times 12 \text{ mm}$  dimension and is connected to a 2.15 mm-wide 4.9 mm-long feedline. The electrical size of the antenna for the overall width and length of the radiating element is  $0.68\lambda$  and  $0.42\lambda$ , respectively. The ground measures  $4.5 \text{ mm} \times 12 \text{ mm}$ . Two rectangular patches have been cut from the middle and right-hand sides of the radiator. The removed middle section from the patch has a  $5.38 \text{ mm} \times 2.9 \text{ mm}$  dimension, while the removed section from the side is  $6.3 \text{ mm} \times 3.1 \text{ mm}$ . The removed radiator sections also give the antenna a swan-shaped design. The total dimension of every section of the antenna is marked in Figure 1(c), and the values are given in Table 2.

## 3. Free-Space Simulation Results

Figure 2 shows the return loss curves of the proposed textile antenna. The antenna produced a very wide  $-10 \text{ dB}$  impedance bandwidth of 11.632 GHz with a center frequency of 60.01 GHz in free-space conditions. The antenna shows a very good return loss value of close to  $-19 \text{ dB}$  at the operating frequency. With a radiation efficiency of 89.4%, the antenna achieved a maximum gain of 8.535 dB, as shown in Table 3. Figure 3(a) shows the 3D radiation pattern at 60 GHz, while the E-plane and H-plane radiation patterns are shown in Figures 3(b) and 3(c), respectively. The radiation pattern of this antenna shows nearly omnidirectional radiation patterns with slight distortion at various angles. This could be due to the lower ground plane of the backside of this antenna. The antenna's E- and H-plane radiation patterns at 60 GHz are shown to have good characteristics, except for slight null and few angles. The voltage standing wave ratio (VSWR) is shown in Figure 4. The figure shows that the antenna has a VSWR value at 60 GHz, close to 1.3, which is excellent. For a surface, the current distribution is shown in Figure 5.

**3.1. Parametric Studies.** For the parametric study, the antenna's feedline width ( $fw$ ), length ( $l$ ), and ground length ( $lg$ ) were changed to observe the changes in the return loss curve. The rectangular patch size removed from the middle section was also varied by changing the values of the variables "ls" and "ws."

**3.1.1. Feedline Width ( $fw$ ).** The center frequency shifted slightly towards the right to 60.164 GHz when the feedline width was made smaller from 2.15 mm to 2 mm. Bandwidth decreased by 300 MHz while both gain and radiation efficiency remained virtually unchanged. When the feedline width was increased to 2.5 mm, the center frequency shifted to the left to 59.66 GHz. The bandwidth significantly increased by more than 1 GHz when compared to free space. Gain remained unchanged for both smaller and larger widths. While the radiation efficiency slightly increased for feedline width. Figure 6 shows a return loss comparison curve for different feedline widths with the free-space result. Table 3 contains the detailed values of the parameters for feedline width changes.

**3.1.2. Total Length of Antenna ( $l$ ).** When the antenna " $l$ " length was decreased from 12.2 mm to 12 mm, a shift of the center frequency to the right was observed (Figure 7). Bandwidth remained unchanged, but both gain and radiation efficiency marginally increased. For a larger antenna length of 12.5 mm, the center frequency shifted significantly to 58.834 GHz. All three parameters, bandwidth, gain, and radiation efficiency, decreased slightly. The details are given in Table 4, and the return loss comparison curves are given in Figure 7.

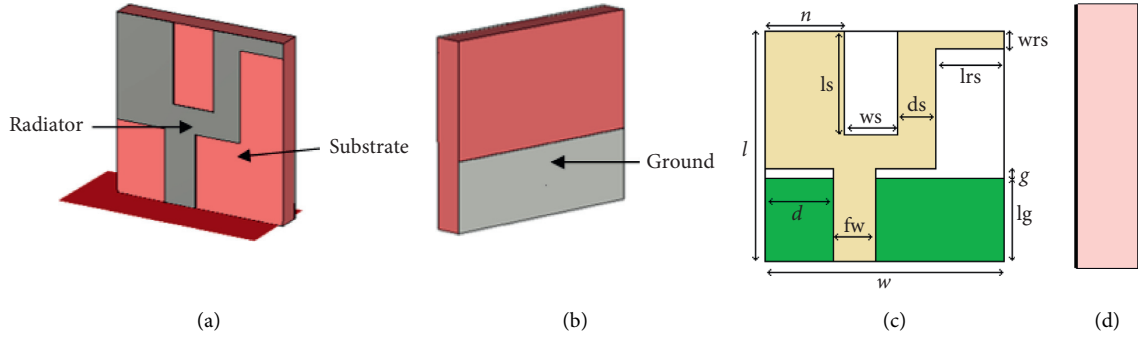


FIGURE 1: (a) Perspective front view; (b) perspective back view; (c) antenna dimensions; (d) left view.

TABLE 1: Antenna parts and materials.

Antenna part	Thickness (mm)	Material	Dielectric constant
Ground	0.035	PEC	—
Substrate	1.5	100% polyester	1.9
Patch radiator	0.035	PEC	—

TABLE 2: Antenna dimensions.

Parameter	Value (mm)
$w$	12
$l$	12.2
$lg$	4.5
$g$	0.4
$d$	3.5
$fw$	2.15
$n$	4.1
$ls$	5.38
$lrs$	3.1
$ws$	2.9
$wrs$	1

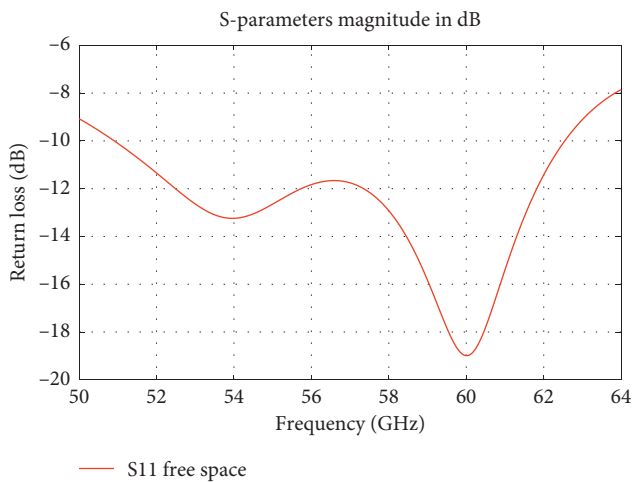


FIGURE 2: Return loss of the antenna in free space.

**3.1.3. Ground Plane Length ( $lg$ ).** Decreasing the size of the ground length,  $lg$ , by 0.5 mm, made the center frequency shift to the right while increasing the impedance bandwidth

(Figure 8). Gain remained unchanged, but the radiation efficiency decreased by more than 1%. Opposite observations were made when the size of the ground length was increased. The center frequency shifted to the left, bandwidth decreased by 0.6 GHz (Figure 8), radiation efficiency increased, and the gain remained almost the same (Table 5).

**3.1.4. Length “ $ls$ ” and Width “ $ws$ ”.** Figures 9(a) and 9(b) show the return loss for change in radiator dimension. A huge shift of the center frequency to the left was observed when the length “ $ls$ ” was decreased from 5.38 mm to 5 mm (Figure 9(a)). Even though both bandwidth and gain increased, the radiation efficiency decreased slightly. Very few changes were observed when the length was increased to 5.5 mm. Altering the width “ $ws$ ” from 2.9 mm to 2.6 mm and 3.2 mm had an insignificant effect on all four parameters. Table 6 shows all the detailed values from these changes.

**3.2. Simulation Results Using Different Textiles.** The antenna’s polyester substrate was replaced by 10 different fabrics to analyze the antenna design in free-space further. These fabrics are as follows: Jeans, Denim, Silk, Tween, Panama, Felt, Moleskin, Cotton, Quartzel Fabric, and Cordura/Lycra. The dimensions of these substrates were kept the same as 100% polyester, but the thickness was altered depending on the fabric used. Results indicate that denim, tween, and quartzel fabric performed closest to the initial design in terms of center frequency and bandwidth (Figure 10(a)). Except for cordura/lycra, the gain was above 8 dBi for all the substrates. Due to the similar thickness and relative permittivity of jeans and quartzel fabric, the results were very similar to polyester fabric. A summary of this fabric variation free-space analysis is given in Table 7. Figures 10(b) and 10(c) show the antenna’s E and H plane radiation patterns for different textile substrates. Due to different textile substrates, the E and H plane radiation patterns do

TABLE 3: Feedline width (fw) changes.

Parameters	Free-space fw = 2.15 mm	fw = 2 mm	fw = 2.5 mm
Center frequency (GHz)	60.01	60.164	59.66
Bandwidth (GHz)	11.632	11.302	12.354
Gain (dBi)	8.535	8.54	8.523
Radiation efficiency (%)	89.4	89.3	89.61

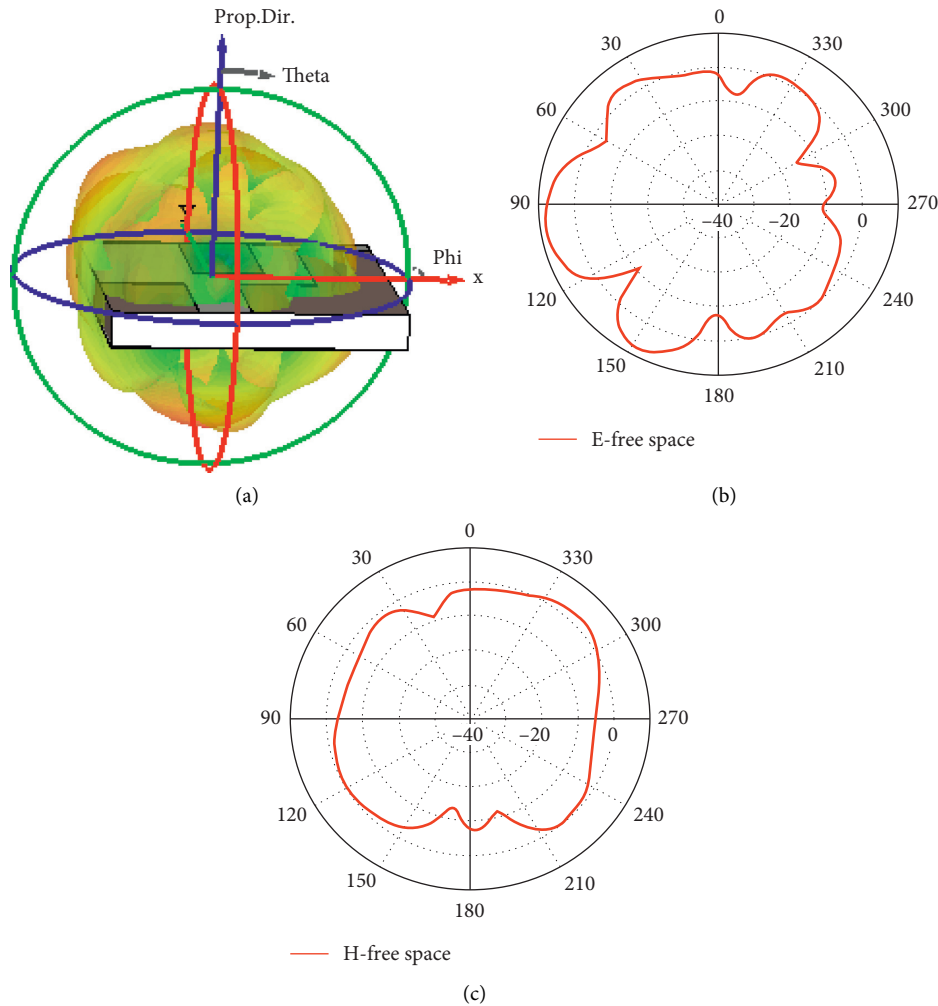


FIGURE 3: (a) 3D radiation pattern free space for 60 GHz, (b) E-plane radiation pattern free space for 60 GHz, and (c) H-plane radiation pattern free space for 60 GHz.

not change much, but a slight variation of power level is observed.

#### 4. On-Body Simulation Results

For body-centric simulations, a human torso-equivalent phantom is created. This phantom contains three layers representing skin, fat, and muscle. mm-waves have very low penetration capability, and at 60 GHz, they can penetrate only 0.5 mm of human skin [15]. For this reason, most of the research works for 60 GHz are based on skin-

equivalent phantom [18, 19]. We have chosen three layers for our work to represent a more accurate model of the human body. These three layers can be modeled accurately by taking their relative permittivity and conductivity. In Table 8, detailed values of the dimensions, relative permittivity, and conductivity of the torso phantom are given [28]. Figure 11(a) shows the different layers of the human torso phantom.

The antenna was positioned at 5 different distances from the phantom to analyze the antenna's performance in wearable scenarios. Starting from 2 mm, the antenna was

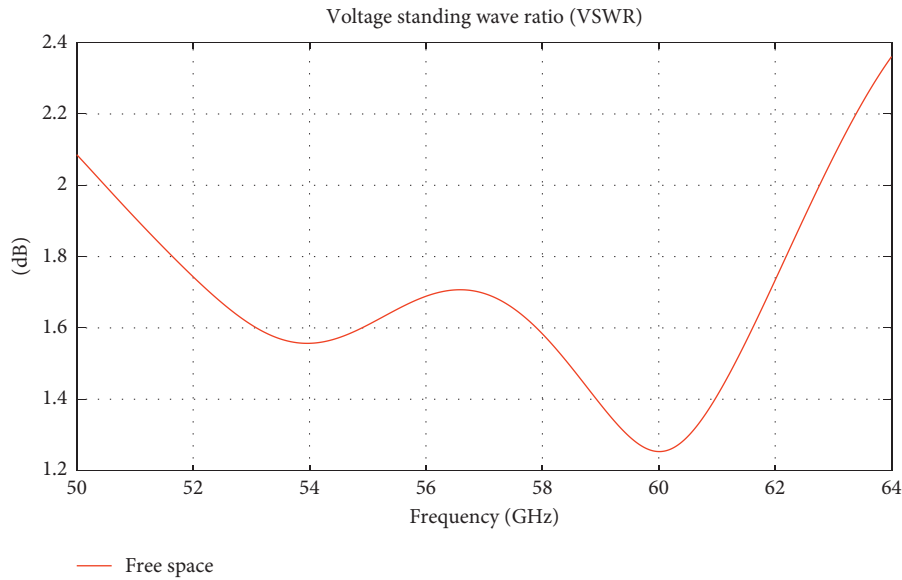


FIGURE 4: VSWR of the antenna at 60 GHz.

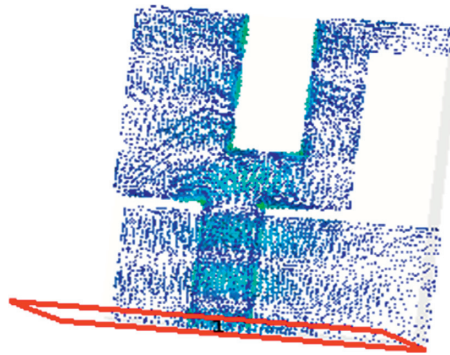


FIGURE 5: Free-space surface current distribution for 60 GHz.

moved gradually 2 mm away and ended up 10 mm away from the phantom. Figures 11(b)–11(d) show the antenna's position at three different distances.

**4.1. 100% Polyester Results.** The return loss curves for different antenna placement distances from the three layers of the human body model are shown in Figure 12(a). At 2 mm and 6 mm away from the phantom, the center frequency of the antenna shifted by around 0.5 GHz. The shift was not as significant for 4, 8, and 10 mm, while at 10 mm, the center frequency was closest to the free-space center frequency. From distances of 6 mm and above, the impedance bandwidth was over 11 GHz, with 8 mm having the highest bandwidth. The bandwidth was lowest at 4 mm, and at 2 mm, it was just above 10 GHz. The maximum gain was around 8.7 dBi for distances of 6, 8 and 10 mm. At 2 mm, the gain dropped to a minimum value of 5.27 dBi. Radiation efficiency increased as the antenna's distance from the phantom increased but was significantly lower compared to

free-space. In this study, it is noted that the antenna's on-body radiation efficiency is slightly lower than free space. This happens due to the absorption of different lossy tissues of the human body. From Table 9, it is noted that the reduction of radiation efficiency is lower when the distance between the antenna and the body increases. This happens because when the antenna is placed at a higher distance from the human body, it has less effect on the radiation efficiency from lossy human tissues. Table 9 summarizes the results of on-body antenna performance with distance variation. E-Plane and H-plane radiation pattern with distance variation are shown in Figures 12(b) and 12(c). The radiation patterns for E and H planes do not change much for changing the distance between the antenna and the human body model, whereas the variation of power loss is observed.

**4.2. Different Textile Results.** All ten substrates were also simulated for an on-body scenario by keeping the antenna 2 mm away from the phantom. Antenna's performance

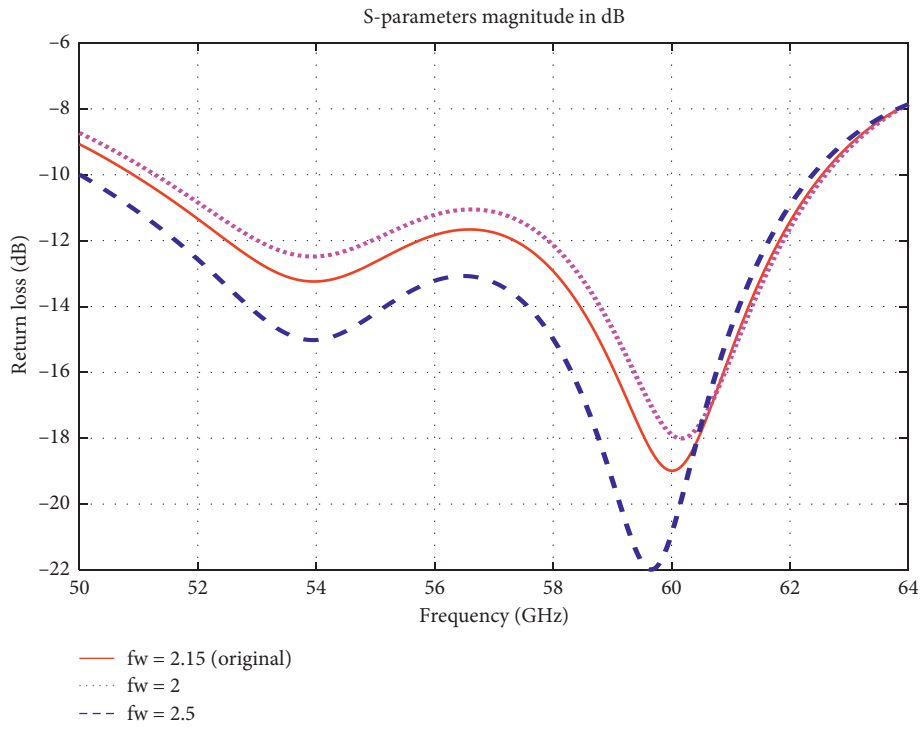


FIGURE 6: Return loss for different feedline widths.

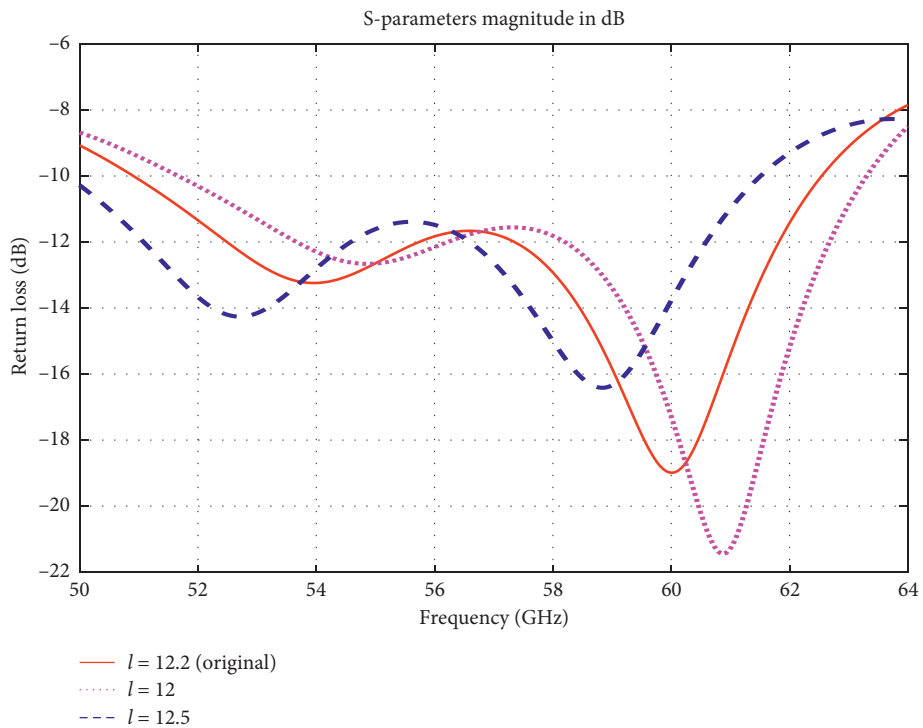


FIGURE 7: Return loss for change in antenna length “ $l$ .”

TABLE 4: Antenna length changes.

Parameters	Free-space $l = 12.2$ mm	$l = 12$ mm	$l = 12.5$ mm
Center frequency (GHz)	60.01	60.878	58.834
Bandwidth (GHz)	11.632	11.63	11.505
Gain (dBi)	8.535	8.622	8.235
Radiation efficiency (%)	89.4	89.62	88.79

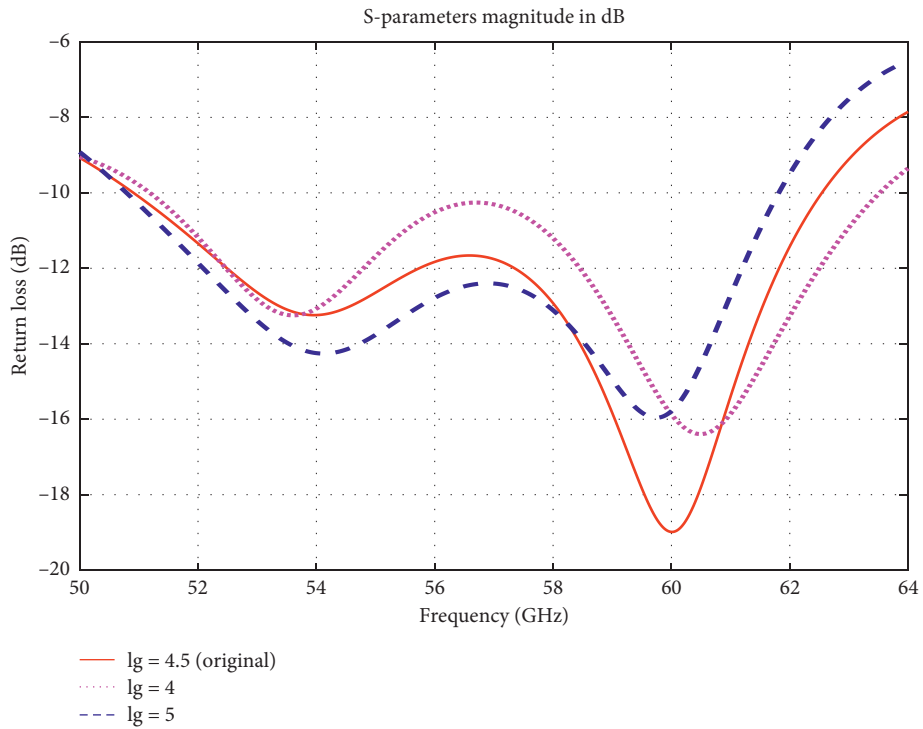


FIGURE 8: Return loss for change in ground length “lg.”

TABLE 5: Ground plane length changes.

Parameters	Free-space lg = 4.5 mm	lg = 4 mm	lg = 5 mm
Center frequency (GHz)	60.01	60.5	59.744
Bandwidth (GHz)	11.632	12.345	11.018
Gain (dBi)	8.535	8.555	8.692
Radiation efficiency (%)	89.4	88.1	89.87

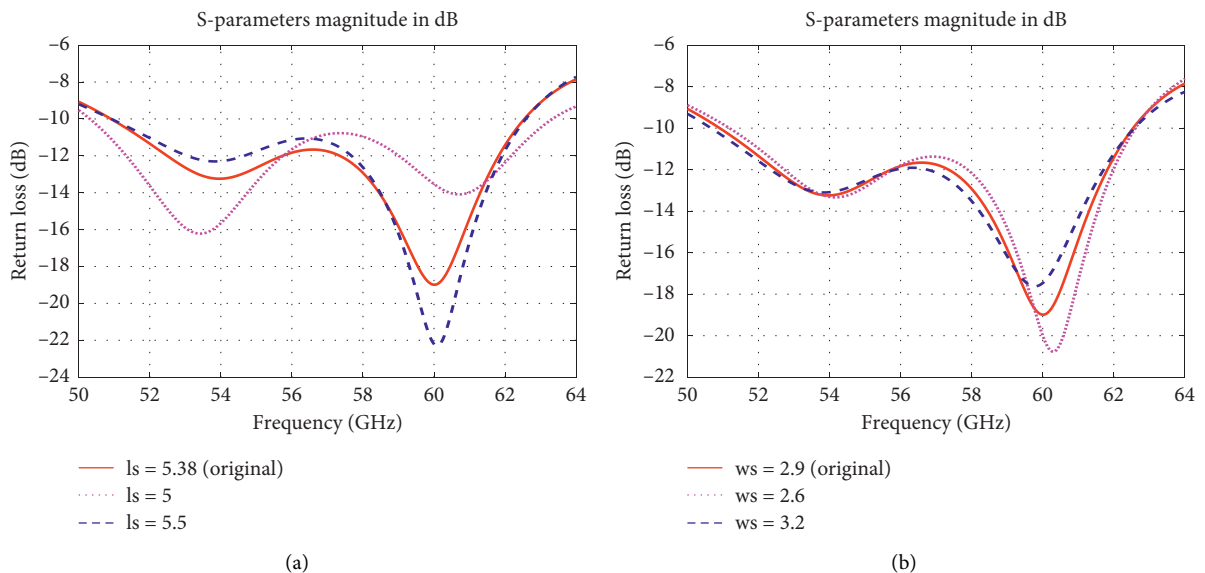


FIGURE 9: Return loss for change in radiator dimension. (a) “ls.” (b) “ws.”

TABLE 6: Radiator length (ls) and width (ws) change.

Parameters	Free space	ls = 5	ls = 5.5	ws = 2.6	ws = 3.2
Center frequency (GHz)	60.01	53.416	60.08	60.29	59.772
Bandwidth (GHz)	11.632	13.002	11.657	11.427	11.894
Gain (dBi)	8.535	8.94	8.523	8.323	8.854
Radiation efficiency (%)	89.4	88.75	89.42	89.47	89.49

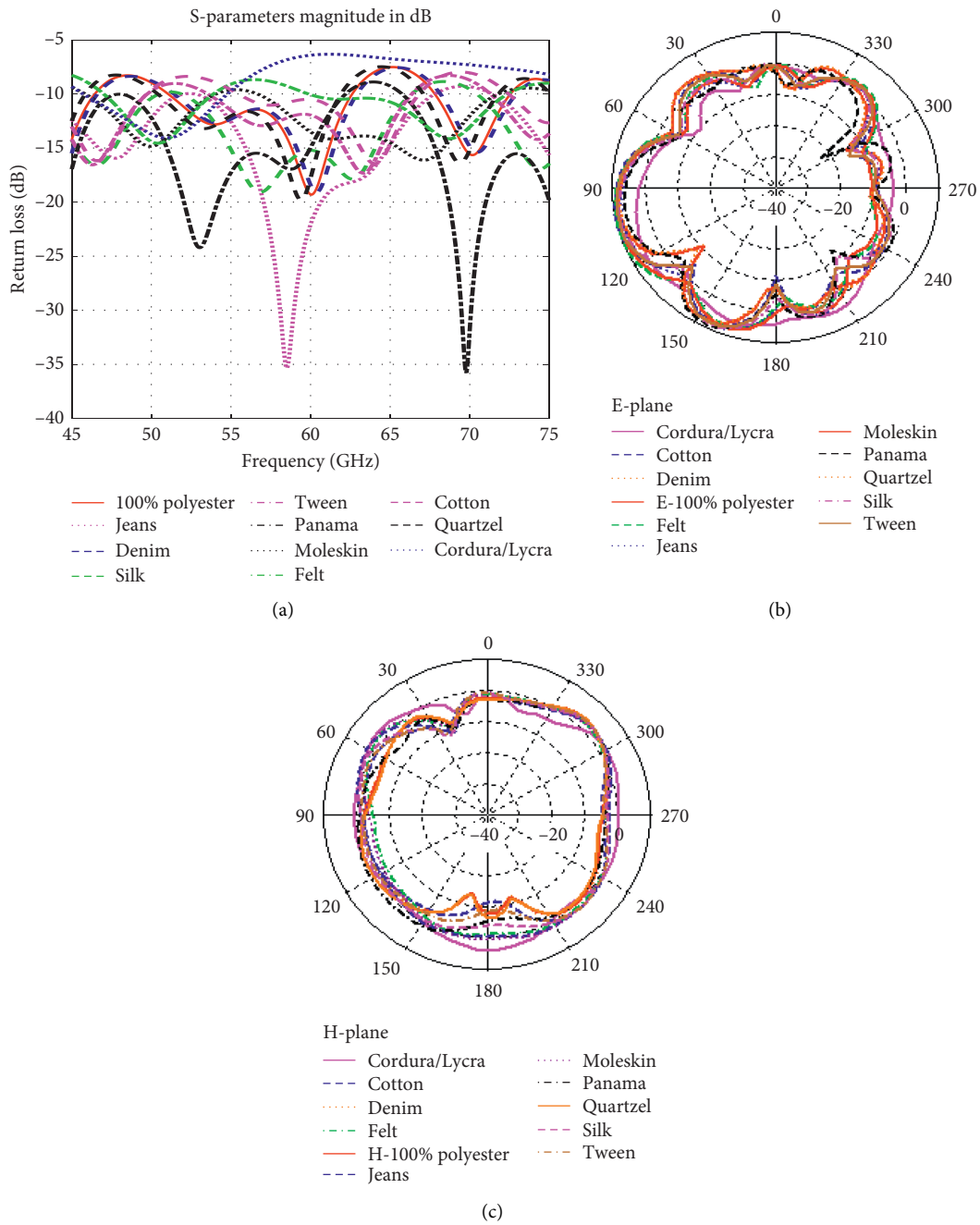


FIGURE 10: Comparison of antenna performance for different textile substrates in free-space (a) return loss (b) E-plane radiation patterns (c) H-plane radiation patterns.

TABLE 7: Free-space performance summary of the antenna for different textiles.

Substrate	Relative permittivity	Thickness (mm)	Center frequency (GHz)	Bandwidth (GHz)	Gain (dBi)	Radiation efficiency (%)
100% polyester	1.9	1.5	60.06	11.578	8.531	89.69
Jeans	1.7	1	58.5	15.094	7.841	93.19
Denim	1.87813	1.5	60.36	11.505	8.653	89.91
Silk	1.75	1.16	56.82	14.439	8.298	92.33
Tween	1.69	1.37	60.3	12.818	9.138	91.88
Panama	2.12	1.04	53.069	14.184	8.864	91.48
Felt	1.38	1.38	68.772	12.507	9.824	93.64
Moleskin	1.45	1.17	67.11	15.141	8.862	93.87
Cotton	1.63	1.5	64.05	11.357	9.686	91.58
Quartzel fabric	1.95	1.5	59.4	11.515	8.217	89.16
Cordura/Lycra	1.5	0.5	50.97	9.052	5.213	95.49

TABLE 8: Properties of a torso phantom.

Parameter	Length (mm)	Width (mm)	Thickness (mm)	Relative permittivity	Conductivity (S/m)
Skin	20	20	2	7.9753	36.397
Fat	20	20	3	3.1324	2.8152
Muscle	20	20	10	12.856	52.825

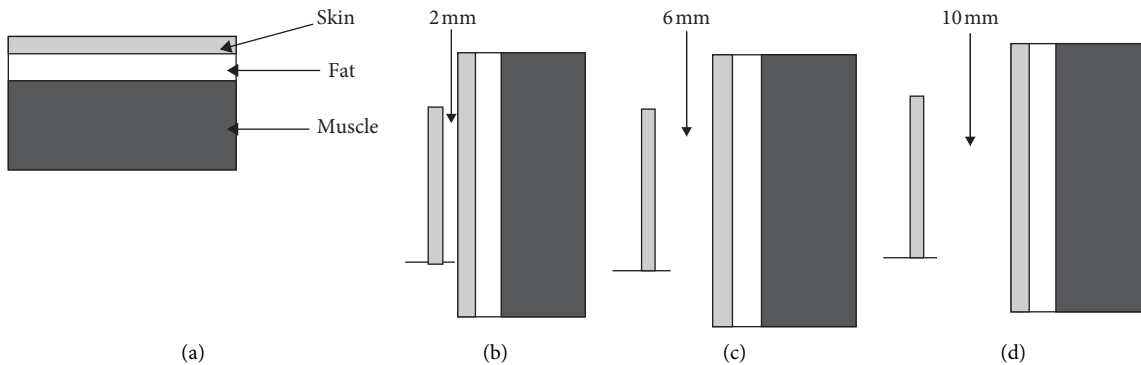


FIGURE 11: (a) Different layers of torso-equivalent torso, (b) antenna 2 mm away from phantom, (c) antenna 6 mm away from phantom and (d) antenna 10 mm away from the phantom.

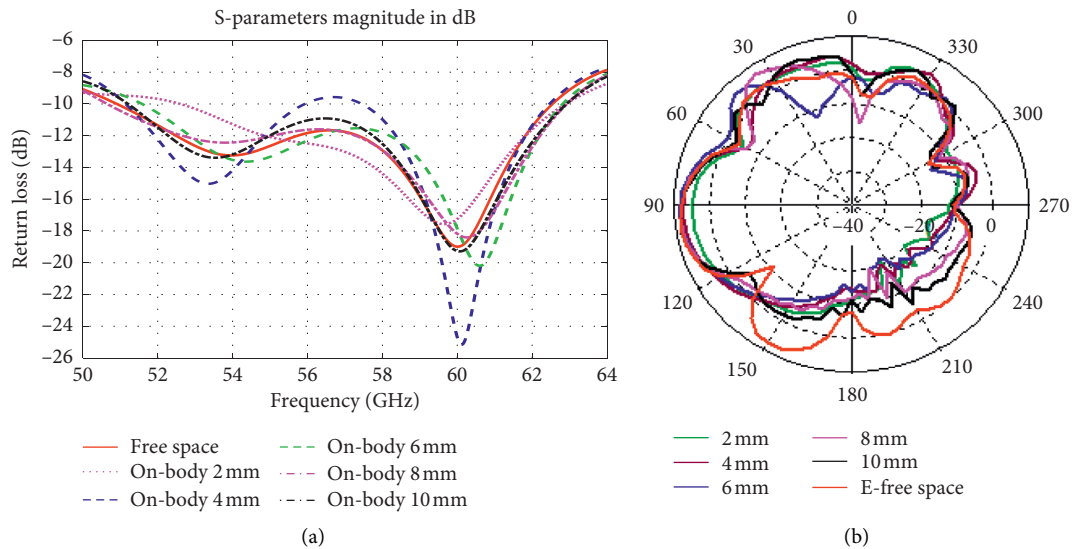


FIGURE 12: Continued.

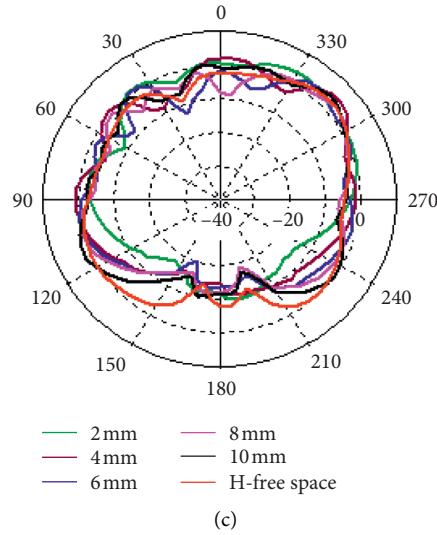


FIGURE 12: Polyester on-body (a) Return loss at different distances, (b) E-plane radiation patterns and (c) H-plane radiation patterns.

TABLE 9: 100% polyester on-body performance summary.

Parameters	Free-space	On-body 2 mm	On-body 4 mm	On-body 6 mm	On-body 8 mm	On-body 10 mm
Center frequency (GHz)	60.01	59.646	60.122	60.598	60.262	60.066
Bandwidth (GHz)	11.632	10.271	5.012	11.225	12.269	11.71
Gain (dBi)	8.535	5.272	7.629	8.695	8.703	8.69
Radiation efficiency (%)	89.4	63	69.44	74.06	78.06	80.65

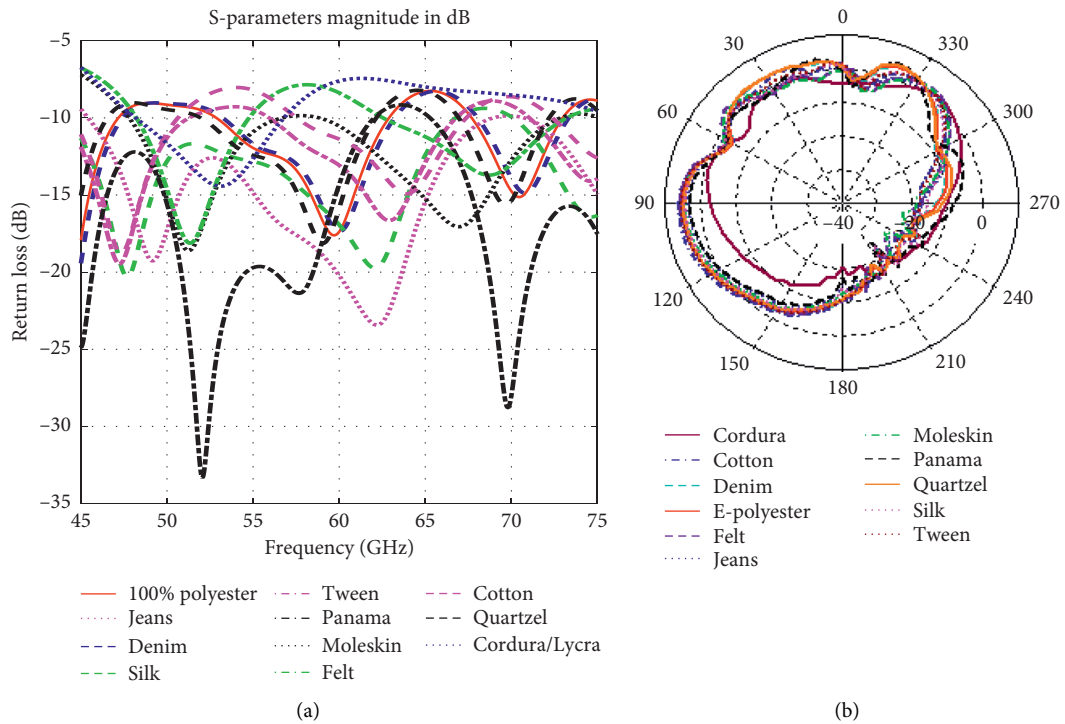


FIGURE 13: Continued.

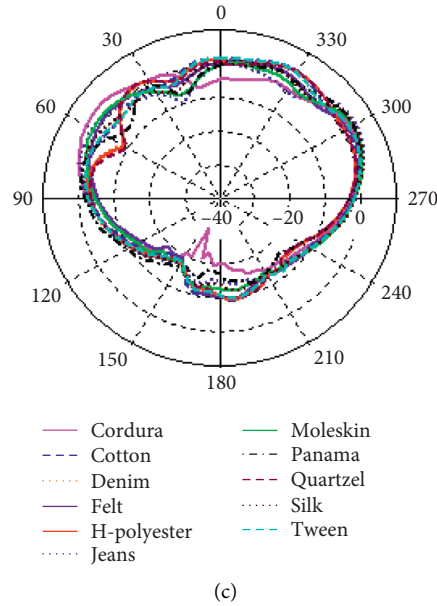


FIGURE 13: (a) On-body return loss responses for different textiles, (b) E-plane radiation patterns (c) H-plane radiation patterns.

TABLE 10: Different textiles performance summary at 2 mm away from phantom.

Substrate	Center frequency (GHz)	Bandwidth (GHz)	Gain (dBi)	Radiation efficiency (%)
100% polyester	59.718	10.01	5.209	63.29
Jeans	62.19	23.51	4.376	43.53
Denim	60	9.962	5.239	62.93
Silk	62.135	22.641	4.359	50.30
Tween	62.972	10.484	5.280	56.08
Panama	52.05	—	4.766	50.12
Felt	68.684	10.681	5.674	49.82
Moleskin	66.993	13.98	4.442	45.75
Cotton	63.878	9.84	5.958	58.03
Quartzel fabric	59.04	10.158	5.20	64.02
Cordura/Lycra	53.13	8.604	6.658	53.86

TABLE 11: Performance comparison with previous works.

Reference	Antenna dimension (mm)	Textile substrate	Free-space bandwidth (GHz)	Free-space gain (dBi)	On-body bandwidth (GHz)	On-body gain (dBi)
This work	$12.2 \times 12 \times 1.57$	100% polyester	11.578	8.531	10.01	5.209
[18]	*	Cotton	57–64*	8.6	57–64*	7.7
[19]	$26 \times 8 \times 0.34$	Cotton	55–64*	9.2	55–64*	11.9

\*Exact values not provided.

using denim and quartzel fabric was closest to on-body polyester performance. Figure 13(a) shows an on-body return loss comparison for all 10 different substrates along with the original polyester substrate. For denim, even though the maximum gain decreased to 5.239 dBi, the center frequency was exactly at 60 GHz and bandwidth close to 10 GHz. With a low gain of 4.376 dBi, 43.53% radiation efficiency, and center frequency of 62.19 GHz, jeans achieved the highest bandwidth of 23.51 GHz. Overall, every substrate

achieved a bandwidth higher than 8.6 GHz, while the radiation efficiency never exceeded 64.02%. Detailed values from the on-body analysis are given in Table 10. Figures 13(b) and 13(c) show the antenna's E and H plane radiation patterns for different textiles when the antenna is placed 2 mm away from the human body model. For changing different textile substrates, the on-body radiation patterns of the antenna change slightly; however power loss is noticed.

## 5. Comparison with Previous Works

As mentioned previously, there aren't many 60 GHz textile antennas studied for body-centric communications. Compared to works in [18, 19], the antenna proposed in this work is smaller in length but a bit wider. Overall, the dimension is a little bit more compact than other works. The bandwidth of our proposed antenna was higher in both free-space and on-body. The proposed design in this study achieved a similar result in free-space in terms of maximum gain, but for on-body, gain decreased significantly. Table 11 provides a comparative overview of our work and other known designs.

## 6. Conclusions

This paper's main purpose was to design a compact 60 GHz antenna based on a textile substrate for body-centric communication. Designed on a 100% polyester substrate, the microstrip patch antenna showed high impedance bandwidth in the 60 GHz band with good radiation efficiency. From parametric studies, it is shown that by decreasing the ground length, the bandwidth increases. Both gain and radiation efficiency are not affected much when changes are made in radiator and ground size. For on-body arrangement, the antenna performed best when kept at 8 mm away from a phantom. We have seen both bandwidth and gain increase at this distance compared to free-space with a slight degradation in radiation efficiency. The antenna's lowest gain was at the closest distance from the phantom. In general, the antenna's performance kept on improving as the distance between the phantom and the antenna kept on increasing.

Their relative permittivity value characterizes textile substrates. This was evident as the antenna performed equally well when the polyester substrate was replaced by denim, tweek, or quartzel fabric. Compared to previous works on 60 GHz textile antennas, our design achieved higher impedance bandwidth. Even though the free-space gain was similar, the on-body gain was much lower. There are not many textile antennas designed for mm-wave wearable devices. Our work will be a good addition to this class of antennas because of its compact and relatively simple design.

## Data Availability

The data used to support the findings of this study are freely available at <http://niremf.ifac.cnr.it/tissprop/>

## Conflicts of Interest

The authors declare that they have no conflicts of interest to report regarding the present study.

## Acknowledgments

The authors are thankful for the support from Taif University Researchers Supporting Project (TURSP-2020/239), Taif University, Taif, Saudi Arabia.

## References

- [1] T. S. Rappaport, G. R. MacCartney, M. K. Samimi, and S. Sun, "Wideband millimeter-wave propagation measurements and channel models for future wireless communication system design," *IEEE Transactions on Communications*, vol. 63, no. 9, pp. 3029–3056, 2015.
- [2] P. S. Hall and Y. Hao, "Antennas and propagation for body centric communications," in *Proceedings of the 2006 First European Conference on Antennas and Propagation*, pp. 1–7, Nice, France, November 2006.
- [3] T. Guo, R. C. Qiu, S. S. Mo, and K. Takahashi, "60 GHz millimeter-wave radio: principle, technology, and new results," *EURASIP Journal on Wireless Communications and Networking*, vol. 2007, Article ID 068253, 2006.
- [4] A. M. Al-samman, M. H. Bin Azmi, and T. A. Rahman, "A survey of millimeter wave (mm-wave) communications for 5G: channel measurement below and above 6 GHz," in *Recent Trends in Data Science and Soft Computing*, F. Saeed, N. Gazem, F. Mohammed, and A. Busalim, Eds., vol. 843 Berlin, Germany, Springer, 2019.
- [5] H.-B. Li, K.-I. Takizawa, B. Zhen, and R. Kohno, "Body area network and its standardization at IEEE 802.15.MBAN," in *Proceedings of the 16th IST Mobile and Wireless Communications Summit*, pp. 1–5, Budapest, Hungary, July 2007.
- [6] J. Tak and J. Choi, "An all-textile louis vuitton logo antenna," *IEEE Antennas and Wireless Propagation Letters*, vol. 14, pp. 1211–1214, 2015.
- [7] B. Almohammed, A. Ismail, and A. Sali, "Electro-textile wearable antennas in wireless body area networks: materials, antenna design, manufacturing techniques, and human body consideration-a review," *Textile Research Journal*, vol. 91, no. 5-6, pp. 646–663, 2020.
- [8] T.-W. Koo, Y.-J. Hong, G.-K. Park, K. Shin, and J.-G. Yook, "Extremely low-profile antenna for attachable bio-sensors," *IEEE Transactions on Antennas and Propagation*, vol. 63, no. 4, pp. 1537–1545, 2015.
- [9] M. M. Khan, Q. H. Abbasi, A. Alomainy, C. Parini, and Y. Hao, "Dual band and dual mode antenna for power efficient body-centric wireless communications," in *Proceedings of the IEEE International Symposium on Antennas and Propagation (APSURSI)*, pp. 396–399, Spokane, WA, USA, July 2011.
- [10] M. M. Khan, Q. H. Abbasi, and R. H. Ashique, "Comprehensive design and propagation study of a compact dual band antenna for healthcare applications," *Journal of Sensor and Actuator Networks*, vol. 4, no. 2, pp. 50–66, 2015.
- [11] B. Yeboah-Akokuah, P. Kosmas, and Y. Chen, "A Q-slot monopole for UWB body-centric wireless communications," *IEEE Transactions on Antennas and Propagation*, vol. 65, no. 10, pp. 5069–5075, 2017.
- [12] Q. H. Abbasi, M. M. Khan, S. Liaqat, M. Kamran, A. Alomainy, and Y. Hao, "Experimental investigation of ultra wideband diversity techniques for on-body radio communications," *Progress in Electromagnetics Research C*, vol. 34, pp. 165–181, 2013.
- [13] S. F. Jilani, M. O. Munoz, Q. H. Abbasi, and A. Alomainy, "Millimeter-wave liquid crystal polymer based conformal antenna array for 5G applications," *IEEE Antennas and Wireless Propagation Letters*, vol. 18, no. 1, pp. 84–88, 2019.
- [14] K. Islam, T. Hossain, M. Monirujjaman Khan, M. Masud, and R. Alroobaea, "Comparative design and study of a 60 GHz antenna for body-centric wireless communications,"

- Computer Systems Science and Engineering*, vol. 37, no. 1, pp. 19–32, 2021.
- [15] K. Islam, T. Hossain, and M. M. Khan, “A compact novel design of a 60 GHz antenna for body-centric communication,” *International Journal on Communications Antenna and Propagation (IRECAP)*, vol. 10, no. 5, pp. 325–333, 2020.
- [16] J. Puskely, M. Pokorny, J. Lacik, and Z. Raida, “Wearable disc-like antenna for body-centric communications at 61 GHz,” *IEEE Antennas and Wireless Propagation Letters*, vol. 14, pp. 1490–1493, 2015.
- [17] M. Ur-Rehman, N. A. Malik, X. Yang, Q. H. Abbasi, Z. Zhang, and N. Zhao, “A low profile antenna for millimeter-wave body-centric applications,” *IEEE Transactions on Antennas and Propagation*, vol. 65, no. 12, pp. 6329–6337, 2017.
- [18] N. Chahat, M. Zhadobov, S. A. Muhammad, L. Le Coq, and R. Sauleau, “60 GHz textile antenna array for body-centric communications,” *IEEE Transactions on Antennas and Propagation*, vol. 61, no. 4, pp. 1816–1824, 2013.
- [19] N. Chahat, M. Zhadobov, L. Le Coq, and R. Sauleau, “Wearable endfire textile antenna for on-body communications at 60 GHz,” *IEEE Antennas and Wireless Propagation Letters*, vol. 11, pp. 799–802, 2012.
- [20] M. Mohamed, M. B. EL\_Mashade, S. Berra, G. S. Gaba, and M. Masud, “A novel hybrid precoding-combining technique for peak-to-average power ratio reduction in 5G and beyond,” *Sensors*, vol. 21, no. 4, p. 1410, 2021.
- [21] S. Yan, V. Volskiy, and G. A. E. Vandenbosch, “Compact dual-band textile PIFA for 433 MHz/2.4 GHz ISM bands,” *IEEE Antennas and Wireless Propagation Letters*, vol. 16, pp. 2436–2439, 2017.
- [22] M. Hirvonen, C. Böhme, D. Severac, and M. Maman, “On-body propagation performance with textile antennas at 867 MHz,” *IEEE Transactions on Antennas and Propagation*, vol. 61, no. 4, pp. 2195–2199, 2013.
- [23] M. Klemm and G. Troester, “Textile UWB antennas for wireless body area networks,” *IEEE Transactions on Antennas and Propagation*, vol. 54, no. 11, pp. 3192–3197, 2006.
- [24] H. Lee, J. Tak, and J. Choi, “Wearable antenna integrated into military berets for indoor/outdoor positioning system,” *IEEE Antennas and Wireless Propagation Letters*, vol. 16, pp. 1919–1922, 2017.
- [25] P. M. Potey and K. Tuckley, “Design of wearable textile antenna with various substrate and investigation on fabric selection,” in *Proceedings of the 3rd International Conference on Microwave and Photonics (ICMAP)*, pp. 1–2, Dhanbad, India, February 2018.
- [26] M. El Bakkali, M. El Bekkali, G. S. Gaba, J. M. Guerrero, L. Kansal, and M. Masud, “Fully integrated high gain S-band triangular slot antenna for CubeSat communications,” *Electronics*, vol. 10, no. 2, p. 156, 2021.
- [27] A. K. Bairagi, M. S. Munir, M. Alsenwi et al., “Coexistence mechanism between eMBB and uRLLC in 5G wireless networks,” *IEEE Transactions on Communications*, vol. 69, no. 3, pp. 1736–1749, 2021.
- [28] IFAC (International Federation of Accountants), *Dielectric Properties of Body Tissues in the Frequency Range 10 Hz to 100 GHz*, Italian National Research Council, Rome, Italy, 2021.